

MULTIMODE INTERFERENCE IN OPTICAL FIBERS AND ITS APPLICATIONS
OF FIBER LASERS AND AMPLIFIERS

by

Xiushan Zhu

A Dissertation Submitted to the Faculty of the

The COLLEGE OF OPTICAL SCIENCES

In Partial Fulfillment of the Requirements

For the Degree of

DOCTOR OF PHILOSOPHY

In the Graduate College

THE UNIVERSITY OF ARIZONA

2008

Directions: For best results, highlight the parenthesis sections and type over with new information. Please erase these directions as well as everything in parenthesis and unused signature lines before submitting this form. Copy this template and paste it into your dissertation file as the second page.

THE UNIVERSITY OF ARIZONA
GRADUATE COLLEGE

As members of the Dissertation Committee, we certify that we have read the dissertation

prepared by (enter student name)

entitled (enter dissertation title)

and recommend that it be accepted as fulfilling the dissertation requirement for the

Degree of (enter degree title, i.e. Doctor of Philosophy, Doctor of Education, Doctor of Musical Arts)

_____ Date: (Type defense date here)
(Type Dissertation Director Name here)

_____ Date: (Type defense date here)
(Type Committee Member Name here)

_____ Date: (Type defense date here)
(Type Committee Member Name here)

_____ Date: (Type defense date here)
(Type Committee Member Name here)

_____ Date: (Type defense date here)
(Type Committee Member Name here)

Final approval and acceptance of this dissertation is contingent upon the candidate's submission of the final copies of the dissertation to the Graduate College.

I hereby certify that I have read this dissertation prepared under my direction and recommend that it be accepted as fulfilling the dissertation requirement.

_____ Date: (Type defense date here)
Dissertation Director: (Type Name of Director here)

STATEMENT BY AUTHOR

This dissertation has been submitted in partial fulfillment of requirement for an advanced degree at the University of Arizona and is deposited in the University Library to be made available to borrowers under rule of the Library.

Brief quotations from this dissertation are allowable without special permission, provided that acknowledgment of source is made. Requests for permission for extended quotation from or reproduction of this manuscript in whole or in part may be granted by the head of the major department or the Dean of the Graduate College when in his or her judgment the proposed use of the material is in the interests of scholarship. In all other instances, however, permission must be obtained from the author.

SIGNED: Xiushan Zhu

ACKNOWLEDGEMENT

First of all, I acknowledge my academic advisor Dr. Nasser Peyghambarian. I am very grateful to him for agreeing to support me two years ago and providing me the chance to continue the research on fiber lasers and amplifiers. Without his help, I cannot transfer to the University of Arizona and moved to Tucson with my family. Prof. Peyghambarian's high-efficiency on work and wonderful personality impress me very much.

I also would like to express my special appreciation to Dr. Axel Schülzgen for his enthusiastic support and elaborate advice on my research. Axel's attitude and enthusiasm about science have greatly influenced me.

I am grateful for Dr. Franko Kueppers serving as my committee and providing valuable suggestions and helpful advice on my dissertation.

I would also like to appreciate Li Li, Valery L. Temyanko, Yevgeniv A. Merzlyak, Hongbo Li, Qing Wang, Shigeru Suzuki, and Prof. Jerome Moloney for their generous help and useful discussion. Without their support, this thesis would not be completed in such a short time.

Most importantly, I would like to acknowledge my wife, Hua. She has been believing in and encouraging me.

DEDICATION

To My Parents and My Daughter!

TABLE OF CONTENTS

	Page
LIST OF ILLUSTRATIONS.....	8
ABSTRACT.....	20
1. INTRODUCTION.....	22
1.1 Roads of high power fiber lasers and amplifiers.....	22
1.2 Road-blocks to high power fiber lasers and amplifiers.....	27
1.3 New method of removing the road-blocks.....	30
1.4 Outline of the dissertation.....	31
2. MULTIMODE INTERFERENCE IN OPTICAL FIBERS.....	32
2.1 Theory of MMI in Multimode Fibers.....	34
2.2 Self-imaging in Multimode Fibers and Its Properties.....	39
2.2.1 Self-imaging quality.....	41
2.2.2 Self-imaging length interval.....	45
2.2.3 Phase difference between excited modes for self-imaging.....	47
2.2.4 Self-imaging behavior in wavelength representation.....	50
2.3 Experimental Investigation of Self-imaging in Multimode optical fibers.....	56
2.3.1 Direct observation of self-imaging inside an MM fiber.....	56
2.3.2 Spectral filtering effect of MMI and its properties.....	59
2.3.3 Direct observation of self-imaging for different wavelengths.....	63
2.4 Discussion and Conclusion.....	68
3. MMI-BASED FIBER LASERS AND AMPLIFIERS.....	70

TABLE OF CONTENTS – continued

	Page
3.1 The First Demonstration of an MMI-based Fiber Laser.....	72
3.2 High Power MMI-based Fiber Lasers and Amplifiers.....	82
3.2.1 Loss of random mode conversion.....	83
3.2.2 Efficiency of high power MMI fiber lasers.....	85
3.2.3 Spectrum of MMI fiber lasers.....	93
3.2.4 Beam quality of MMI fiber lasers and amplifiers.....	95
3.2.5 Improve the efficiencies of large-core MMI fiber lasers and amplifiers...	97
3.3 Discussion and Conclusion.....	102
4. NONDIFFRACTING BEAM GENERATION.....	105
4.1 Bessel Beams.....	107
4.2 Generation of Nondiffracting Beams from Multimode Fibers.....	116
4.2.1 The principle.....	116
4.2.2 Simulations.....	123
4.2.3 Experimental results.....	136
4.3 High Power Nondiffracting Beams Generation.....	144
4.4 Discussion and Conclusion.....	146
5. SUMMARY AND PROSPECT.....	147
5.1 Summary.....	147
5.2 Prospect.....	150
REFERENCES.....	155

LIST OF ILLUSTRATIONS

	Page
Fig. 1.1 The concept of a core-pumped fiber laser.....	23
Fig. 1.2 The concept of a cladding-pumped fiber laser.....	24
Fig. 1.3 Evolution of continuous-wave output of single-mode 1 μm silica fiber laser, 2.7 μm ZBLAN fiber laser, and 1.5 μm single-frequency fiber laser over the past decade.....	26
Fig. 2.1 A simple fiber structure for studying the self-imaging properties of MM optical fibers.....	34
Fig. 2.2 Field distributions of the excited modes and their in-phase superposition in a 25 μm MM fiber segment of the MMI structure when the launching fiber is an SMF-28.....	37
Fig. 2.3 Field distributions of the excited modes and their in-phase superposition in a 50 μm MM fiber segment of the MMI structure when the launching fiber is an SMF-28.....	37
Fig. 2.4 Field distributions of the excited modes and their in-phase superposition in a 105 μm MM fiber segment of the MMI structure when the launching fiber is an SMF-28.....	38
Fig. 2.5 Intensity distribution in a 25 μm MM fiber segment of the MMI structure when the field of an SMF-28 is launched.....	40
Fig. 2.6 Intensity distribution in a 50 μm MM fiber segment of the MMI structure when the field of an SMF-28 is launched.....	40

LIST OF ILLUSTRATIONS – continued

	Page
Fig. 2.7 Intensity distribution in a 105 μm MM fiber segment of the MMI structure when the signal from a SMF-28 is launched.	41
Fig. 2.8 Self-imaging quality factor γ along the MM fiber segment with a core diameter of 25 μm for the input field from an SMF-28 fiber.....	42
Fig. 2.9 Self-imaging quality factor γ along the MM fiber segment with a core diameter of 50 μm for the input field from an SMF-28 fiber.....	43
Fig. 2.10 Self-imaging quality factor γ along the MM fiber segment with a core diameter of 105 μm for the input field from an SMF-28 fiber.....	44
Fig. 2.11 The maximum self-imaging quality factor γ_{max} within one meter MM fiber segment of different core diameters.....	45
Fig. 2.12 The self-imaging length interval within one meter MM fiber segment of different core diameters.....	46
Fig. 2.13 Energy percentage of the excited modes and the phase differences between the excited modes and the peak mode at three self-imaging positions inside the 25 μm MM fiber.....	47
Fig. 2.14 Energy percentage of the excited modes and the phase differences at a self-imaging point between the excited modes and the mode of highest intensity inside 50 μm MM fiber.....	48
Fig. 2.15 Energy percentage of the excited modes and the phase differences at a self-imaging point between the excited modes and the mode of highest	

LIST OF ILLUSTRATIONS – continued

	Page
intensity inside the 105 μm MM fiber.....	49
Fig. 2.16 Self-imaging quality with respect to wavelength for 199.9 mm, 200 mm, and 200.2 mm long 50 μm MM fibers, respectively.....	51
Fig. 2.17 Individual parameters $\Delta\lambda_{\text{im},n}L$ and their collective behavior $\Delta\lambda_{\text{im}}L$ of the 50 μm fiber are plotted in a wavelength range of 1.5-1.6 μm	53
Fig. 2.18 Individual parameters $d\lambda_n/(dL/L)$ and their collective behavior $d\lambda_n/(dL/L)$ of the 50 μm fiber are plotted in a wavelength range of 1.5-1.6 μm	54
Fig. 2.19 Individual parameters $\Delta\lambda_{\text{im},n}L$ and their collective behavior $\Delta\lambda_{\text{im}}L$ of the 105 μm fiber are plotted in a wavelength range of 1.5-1.6 μm	54
Fig. 2.20 Individual parameters $d\lambda_n/(dL/L)$ and their collective behavior $d\lambda_n/(dL/L)$ of the 105 μm fiber are plotted in a wavelength range of 1.5-1.6 μm	55
Fig. 2.21 Experiment setup for directly observing self-imaging in MM fibers.....	56
Fig. 2.22 Calculated self-imaging quality with respect to the position around 49.1 mm for the 50 μm fiber.....	57
Fig. 2.23 Intensity profiles at positions around 49.1 mm inside the 50 μm fiber.....	58
Fig. 2.24 Experimental setup for the transmission spectrum measurement of an MMI structure.....	59
Fig. 2.25 Transmission spectra of MMI structures with fiber lengths of 20 cm and 100 cm and with a fiber core diameter of 50 μm	60

LIST OF ILLUSTRATIONS – continued

	Page
Fig. 2.26 Transmission spectra of MMI structures with fiber lengths of 20 cm and 100 cm and with a fiber core diameter of 105 μm	61
Fig. 2.27 The self-imaging wavelength interval of the MMI structure with different MM fiber lengths for the 50 μm and 105 μm fiber, respectively.....	62
Fig. 2.28 The self-imaging wavelength shift for 1 cm change of the fiber length of the MMI structure with different MM fiber lengths for the 50 μm and 105 μm fiber, respectively.....	63
Fig. 2.29 The intensity distribution of the facet of the 50 μm MM fiber segment of a MMI structure when a tunable single-frequency signal is launched and the transmission spectrum of the corresponding MMI structure.....	64
Fig. 2.30 The facet image, its three-dimensional plot, and the far-field image of the 50 μm MM fiber segment of a MMI structure when a signal of 1557 nm is input. (a) MM fiber facet image; (b) Three-dimensional plot of (a); (c) Far-field image.....	65
Fig. 2.31 The intensity distribution of the facet of the 105 μm MM fiber segment of a MMI structure when a tunable single-frequency signal is launched and the transmission spectrum of the corresponding MMI structure.....	66

LIST OF ILLUSTRATIONS – continued

	Page
Fig. 2.32 The facet image, its three-dimensional plot, and the far-field image of the 105 μm MM fiber segment of a MMI structure when a signal of 1557 nm is input. (a) MM fiber facet image; (b) Three-dimensional plot of (a); (c) Far-field image.....	67
Fig. 3.1 Gain profile of a heavily Er/Yb codoped phosphate fiber and the transmission spectrum of an MMI cavity with 20-cm-long 50 μm MM fiber.....	73
Fig. 3.2 Design of the MMI fiber laser (the figure is not to scale).....	74
Fig. 3.3 Output power as a function of launched pump power for a MMI fiber laser as shown in Fig. 2 (red squares), a single-polarization MMI fiber laser (green circles), and a free-running MM fiber laser without SM section (blue triangles).....	75
Fig. 3.4 Emission spectra of an MMI fiber laser at various pump power levels.....	77
Fig. 3.5 Transmission spectra of a PMFBG (dotted green line) and a MMI structure consists of a 20 cm long 25 μm Er-Yb codoped MM phosphate fiber and two SMF-28 fibers (dashed line), respectively, and the output spectrum of a MMI fiber laser operating at single-polarization-state (solid red line) and random polarization-state (short dashed line), respectively.....	80
Fig. 3.6 Transmission at the self-imaging wavelength for MMI structures consisting of 50 μm MM fibers with different lengths and an SMF-28.....	84

LIST OF ILLUSTRATIONS – continued

	Page
Fig. 3.7 Transmission at the self-imaging wavelength for MMI structures consisting of 105 μm MM fibers with different lengths and an SMF-28.....	85
Fig. 3.8 Forward powers (solid lines) and backward powers (dotted lines) inside a MMI fiber laser that consists of a 50 cm long 50 μm active MM fiber and a 10 cm long SMF-28 fiber (blue) and inside its corresponding 50 cm long MM fiber laser (red).....	89
Fig. 3.9 Forward powers (solid lines) and backward powers (dotted lines) inside a MMI fiber laser that consists of a 50 cm long 105 μm active MM fiber and a 10 cm long SMF-28 fiber (blue) and inside its corresponding 50 cm long MM fiber laser (red).....	90
Fig. 3.10 Forward powers (solid lines) and backward powers (dotted lines) inside a MMI fiber laser that consists of a 10 cm long 105 μm active MM fiber and a 10 cm long SMF-28 fiber (blue) and inside its corresponding 10 cm long MM fiber laser (red).....	91
Fig. 3.11 Output power with respect to the pump power for a MMI fiber laser that consists of a 50 cm long 50 μm (circle) or 105 μm active MM fiber (downward triangle) and a 10 cm long SMF-28 fiber and their corresponding 50 cm long MM fiber lasers (square and upward triangle, respectively).....	92

LIST OF ILLUSTRATIONS – continued

	Page
Fig. 3.12 Output power with respect to the pump power for a MMI fiber laser that consists of a 10 cm long 105 μm active MM fiber and a 10 cm long SMF-28 fiber (triangle) and the corresponding 10 cm long MM fiber laser (square).....	93
Fig. 3.13 Spectrum of an MMI fiber laser that utilizes a 10 cm long 25 μm Er-Yb codoped phosphate fiber (red line), that of an MMI fiber laser that utilizes a 15 cm long 25 μm Er-Yb codoped phosphate fiber (blue line), and that of the corresponding MM fiber laser (black line).....	94
Fig. 3.14 Depiction of a proposed high-power MMI fiber amplifier in which the MM fiber is employed as the output fiber.....	95
Fig. 3.15 Beam profiles of proposed high-power MMI fiber amplifiers depicted in Fig. 3.14. (a) M^2 was about 1.1 when a 50 μm MM fiber was used; (b) M^2 was about 1.3 when a 105 μm MM fiber was used.....	96
Fig. 3.16 Self-imaging quality factor γ along a MM fiber segment with a core diameter of 105 μm when the input SM fiber has an MFD of 23 μm	98
Fig. 3.17 Self-imaging quality factor γ along a MM fiber segment with a core diameter of 105 μm when the input SM fiber has an MFD of 40 μm	99

LIST OF ILLUSTRATIONS – continued

	Page
Fig. 3.18 Transmission at the self-imaging wavelength for MMI structures consisting of 105 μm MM fibers with different lengths and a LMFD-10 fiber (circle) or an SMF-28 fiber (square).....	100
Fig. 3.19 Output power with respect to the pump power for a MMI fiber laser that consists of a 10 cm long 105 μm active MM fiber and a 10 cm long SMF-28 fiber (triangle), or a 10 cm long LMFD-10 fiber (circle), and the corresponding 10 cm long MM fiber laser (square).....	101
Fig. 4.1 Intensity profile of a zeroth-order Bessel beam.....	108
Fig. 4.2 Intensity profile of a first-order Bessel beam.....	109
Fig. 4.3 Radial intensity profile of the Bessel beam shown in Fig. 4.1 in the propagation direction.....	110
Fig. 4.4 (a) Angular spectrum of a Bessel beam; (b) the k-vectors of the Bessel beam propagate on a conic surface.....	111
Fig. 4.5 Reconstruction of a Bessel beam when its central spot is blocked by an obstruction.....	112
Fig. 4.6 Durnin's first demonstration of Bessel beam [68]	114
Fig. 4.7 Bessel beam generated by use of an axicon lens [68].....	114
Fig. 4.8 Design of a fiber device generating nondiffracting beams (the figure is not to scale)	116

LIST OF ILLUSTRATIONS – continued

	Page
Fig. 4.9 Energy percentage of the strongly excited modes inside the MM fiber segment with core diameters of 50 μm and 105 μm , respective, when the input SM fiber is SMF-28, and the intensity profiles of the odd-th excited modes inside the 105 μm MM fiber	118
Fig. 4.10 Radial intensity profile evolution in the propagation direction of the first five $\text{LP}_{0,n}$ mode, $\text{LP}_{0,7}$ mode and $\text{LP}_{0,9}$ mode.....	121
Fig. 4.11 On-axis intensity evolution of the first five $\text{LP}_{0,n}$ mode, $\text{LP}_{0,7}$ mode and $\text{LP}_{0,9}$ mode in the propagation direction.....	122
Fig. 4.12 Facet intensity profile and radial intensity evolution of the beam coming from the 50 μm MMI fiber device when the signal wavelength is 1510, 1520, and 1540 nm, respectively.....	125
Fig. 4.13 Facet intensity profile and radial intensity evolution of the beam coming from the 50 μm MMI fiber device when the signal wavelength is 1550, 1555, and 1575 nm, respectively.....	126
Fig. 4.14 Facet intensity profile and radial intensity evolution of the beam coming from the 50 μm MMI fiber device when the signal wavelength is 1585, 1590, and 1595 nm, respectively.....	127
Fig. 4.15 On-axis intensity of the beam coming from the 50 μm MMI fiber device when the signal wavelength is 1510, 1520, and 1540 nm, respectively.....	128

LIST OF ILLUSTRATIONS – continued

	Page
Fig. 4.16 On-axis intensity of the beam coming from the 50 μm MMI fiber device when the signal wavelength is 1550, 1555, and 1575 nm, respectively.....	128
Fig. 4.17 On-axis intensity of the beam coming from the 50 μm MMI fiber device when the signal wavelength is 1585, 1590, and 1595 nm, respectively.....	129
Fig. 4.18 Facet intensity profile and radial intensity evolution of the beam coming from the 105 μm MMI fiber device when the signal wavelength is 1500, 1510, and 1520 nm, respectively.....	131
Fig. 4.19 Facet intensity profile and radial intensity evolution of the beam coming from the 105 μm MMI fiber device when the signal wavelength is 1530, 1540, and 1550 nm, respectively.....	132
Fig. 4.20 Facet intensity profile and radial intensity evolution of the beam coming from the 105 μm MMI fiber device when the signal wavelength is 1560, 1570, and 1580 nm, respectively.....	133
Fig. 4.21 On-axis intensity of the beam coming from the 105 μm MMI fiber device when the signal wavelength is 1500, 1510, and 1520 nm, respectively.....	134
Fig. 4.22 On-axis intensity of the beam coming from the 105 μm MMI fiber device when the signal wavelength is 1530, 1540, and 1550 nm, respectively.....	134
Fig. 4.23 On-axis intensity of the beam coming from the 105 μm MMI fiber device when the signal wavelength is 1560, 1570, and 1580 nm, respectively.....	135

LIST OF ILLUSTRATIONS – continued

	Page
Fig. 4.24 Intensity profiles at selected distances from the MM fiber facet for signal wavelengths of (a) 1545 nm and (b) 1570 nm, respectively.....	137
Fig. 4.25 On-axis intensity at the selected distances from the MM fiber facet for signal wavelengths of 1545 nm (blue triangles) and 1570 nm (red circles), respectively, and from a SMF-28 fiber (black squares).....	138
Fig. 4.26 Intensity profiles at selected distances from the MM fiber facet for signal wavelengths of (a) 1510 nm, (b) 1560 nm, (c) 1570 nm, and (d) 1580 nm, respectively.....	140
Fig. 4.27 On-axis intensity at the selected distances from the MM fiber facet for signal wavelengths of 1510 nm (blue triangles), 1560 nm (red squares), 1570 nm (green circles), and 1580 nm (blue triangles), respectively.....	141
Fig. 4.28 Experimental setup to investigate the self-healing property of the nondiffracting beam generated from the fiber device.....	142
Fig. 4.29 Beam profiles at selected positions behind the plane of the needle for the case of blocking (upper row) and unblocking (lower row), respectively.....	143
Fig. 4.30 A proposed active fiber device generating high power diffraction-free beams (SM fiber provides the gain).....	145
Fig. 4.31 A proposed active fiber device generating high power diffraction-free beams (MM fiber provides the gain).....	145

LIST OF ILLUSTRATIONS – continued

	Page
Fig. 5.1 Design of a single-frequency MMI fiber laser.....	151
Fig. 5.2 Optical spectrum of the single-frequency MMI fiber laser.....	151
Fig. 5.3 RF beat signal between the emission of the single-frequency MMI fiber laser and a narrow linewidth single-frequency diode laser measured by an electrical spectrum analyzer.....	152
Fig. 5.4 The fiber length associated with the SBS threshold as a function of the fiber core diameter when the power is 1 kW.....	153
Fig. 5.5 The fiber length associated with the SRS threshold as a function of the fiber core diameter when the power is 1 MW.....	154

ABSTRACT

Multimode interference (MMI) in optical fibers has been studied and its applications in optical fiber lasers and amplifiers have been proposed and demonstrated in this thesis.

When a single-mode fiber is spliced onto a multimode fiber, quasi-reproduction of the field from the single-mode fiber, also called “self-imaging”, occurs periodically along the multimode fiber where the phase differences between the strongly excited modes are very small. The properties of self-imaging in multimode optical fibers have been investigated experimentally and theoretically in this thesis. Key parameters for the design of MMI-based fiber devices have been defined and their corresponding values have been provided for the 50 μm and 105 μm multimode fibers.

By use of the self-imaging effect, a fiber laser with single-transverse-mode output while using a multimode rare-earth-doped fiber has been demonstrated as an alternative route to overcome the constraints of an active single-mode fiber. The first MMI-based fiber laser in the world has provided a perfect beam quality ($M^2 = 1.01$) and an inherent narrow spectrum ($\Delta\lambda_{3\text{dB}} < 0.5 \text{ nm}$). Linearly-polarized narrow-linewidth single-transverse-mode emission has also been obtained from a MMI fiber laser utilizing a single-mode fiber inscribed with a polarization-maintaining fiber Bragg grating. Moreover, high power MMI fiber lasers and amplifiers utilizing rare-earth doped silica large-core multimode fibers have been proposed and their critical features, such as

efficiency, optical spectrum, and beam quality, have been investigated.

On the other hand, because exclusively excited $LP_{0,n}$ modes inside the multimode fiber segment are represented by apertured Bessel fields that have long propagation invariant distances, nondiffracting beams can be generated from the MMI-based fiber devices. In this thesis, the principle of generating nondiffracting beams from multimode optical fibers has been described and the propagation characteristics of the generated beams have been investigated. Active MMI fiber devices to generate tens of watts or even hundreds of watts nondiffracting beams have also been proposed.

CHAPTER 1

INTRODUCTION

1.1 Roads of High Power Fiber Lasers and Amplifiers

A fiber laser or amplifier is an oscillator or amplifier in which the active gain medium is an optical fiber doped with rare-earth elements such as erbium (Er), ytterbium (Yb), neodymium (Nd), dysprosium (Dy), praseodymium (Pr), thulium (Tm), and different synthesizers of these elements. When the rare-earth doped core is pumped by light that can excite ions from the ground level to higher energy level, laser radiation or amplified signal can be obtained through the stimulated emission process like solid-state lasers. As illustrated in Fig. 1, an optical fiber generally consists of a core surrounded by a cladding layer whose refractive index is slightly lower than that of the core and the core can guide light by total internal reflection, therefore a fiber cavity can be designed with an arbitrary length from several centimeters to tens of meters, with recent fiber laser technologies. In contrast to other lasers, the attractive features of fiber lasers and amplifiers include outstanding heat-dissipating capability, excellent beam quality, high optical conversion efficiency, simplicity and compactness, high single-pass gain, low laser threshold, and broad gain bandwidth. Fiber lasers and amplifiers have been studied and developed for

nearly fifty years. To date, the spectrum range of fiber lasers can cover from ultra-violet to mid-infrared and the output level can be up to several kilo-watts.

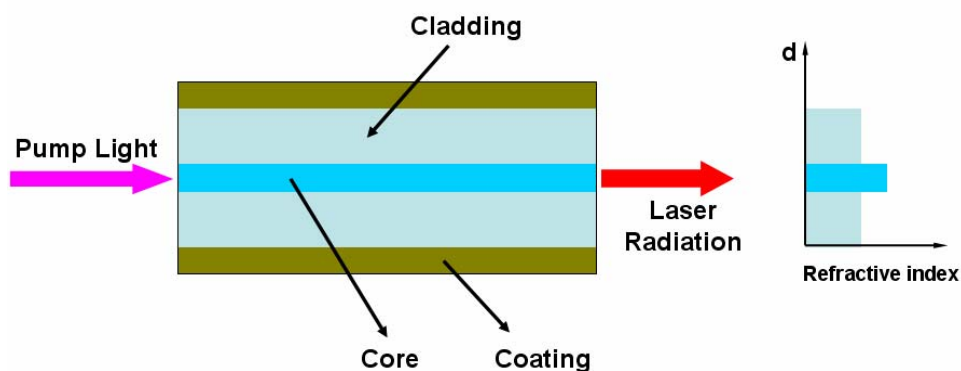


Fig. 1.1. The concept of a core-pumped fiber laser.

The first fiber laser was proposed and demonstrated by Snitzer [1] one year after Maiman's first demonstration of laser action in a ruby crystal [2] in 1960. In 1964, the first fiber laser side-pumped by flash lamp and based on Nd-doped phosphate glasses was developed [3]. In the early works multimode fibers were used to alleviate the problems of thermal heating of the glass host and to enable efficient pumping with flash lamps. However, due to a lack of compatibility with available pump sources, glass fiber lasers offered no compelling benefits that outweighed the disadvantages of laser pumping and did not find wide-spread applications. The advantages of glass fiber lasers became apparent with dramatic improvements in efficiency and performance after the realization of low-loss rare-earth doped single-mode silica fibers. Apart from the complete

elimination of thermal loading, fiber lasers allow operation in a confined diffraction-limited mode, excellent compatibility with single-mode diode pump lasers, long interaction lengths for the laser light in the fiber and very large gain bandwidths. These unique features subsequently led a revolution in optical technology. Particularly the demonstration of the erbium-doped optical amplifier by D. N. Payne and coworkers [4] in 1987, has greatly improved the transmission rates and the reliability of fiber-based communication systems.

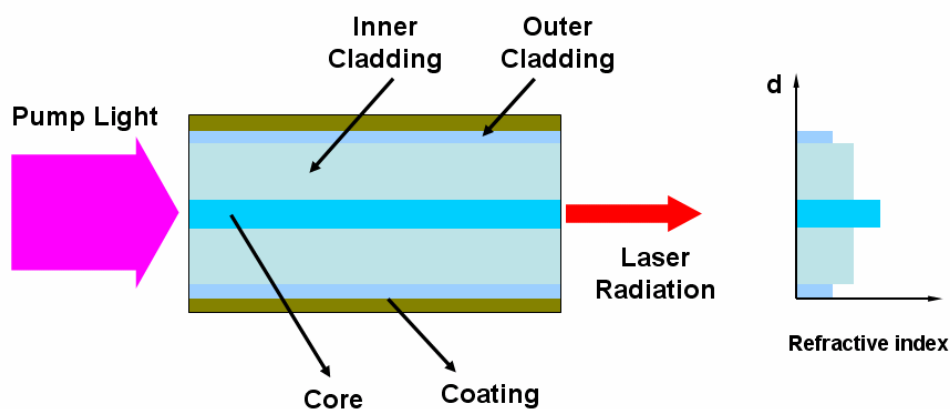


Fig. 1.2. The concept of a cladding-pumped fiber laser.

The subsequent development of erbium-doped fiber amplifiers spurred a large research effort into rare-earth doped fibers and related technologies, in particular diode pump lasers. Initially, fiber lasers were simple structures with a single core, guiding both the signal and the pump light. The requirement for robust operation on a

single-spatial-mode emphasized the need for single-mode cores, implying that single-mode pump diodes must be used. Although core-pumped fiber devices can be very efficient with quantum efficiencies approaching unit, however the limited power of single-mode diode pump sources has restricted the output powers to 1 W.

However, this limitation can be overcome by the use of the double-clad fiber design, invented in 1988 by Snitzer [5]. As shown in Fig. 2, the active doped core is surrounded by a second waveguide, which is highly multimode for pump light. In this second waveguide, also called inner cladding or pumping core, low brightness high power laser diode lasers can be launched. The pump light is gradually absorbed over the entire fiber length and is converted into high brightness high power laser radiation. Consequently, cladding-pumped fiber lasers do not require single-mode pump sources, but can still produce a single-mode laser output. Cladding-pumped fiber technology has revolutionized fiber laser over 1990s by increasing output power from less than 1 W with traditional core-pumping to well over 100 W.

In recent years, power scaling of fiber lasers and amplifiers has attracted considerable interest because of the dramatically increasing demands for high power or high energy laser systems for various applications including laser pumps, space communications, industrial welding and cutting, directed energy weapons, and high-energy physics researches. The two major approaches to obtain higher power or energy laser systems are

either to boost the power level of a single-element fiber laser or amplifier, or to increase the element quantities in a beam combining system.

With the advent of reliable and high-brightness diode pump lasers and double-clad fibers to facilitate coupling the pump light into the fiber, output power of single-mode fiber laser has been significantly increased over the past decade. For instance, as illustrated in Fig. 3, 6-kW 1 μm silica fiber laser [6], 10-watt 2.78 μm ZBLAN fiber laser [7], and 2-watt 1.53 μm single-frequency phosphate fiber laser [8] have been developed.

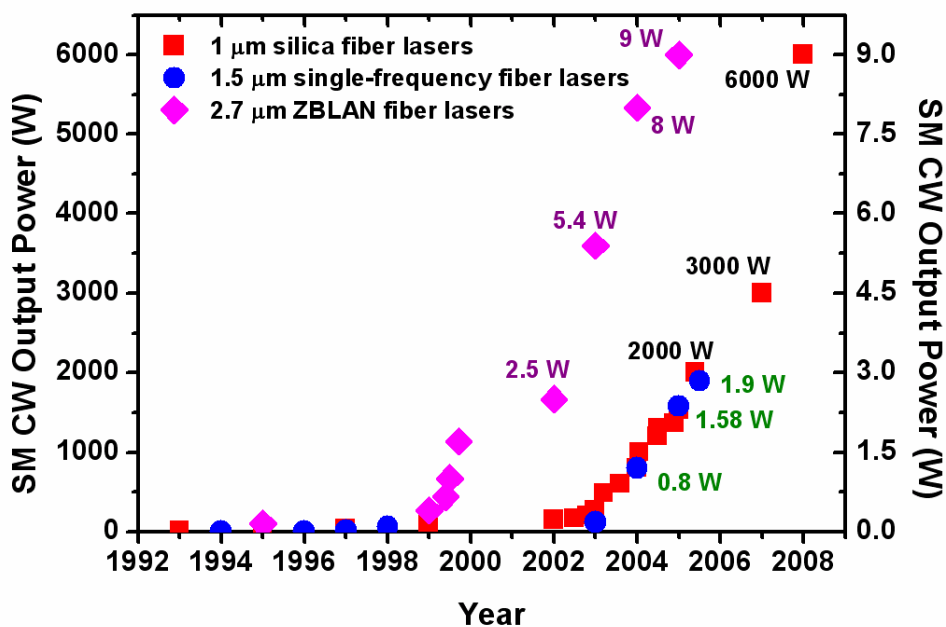


Fig. 1.3. Evolution of continuous-wave output of single-mode 1 μm silica fiber laser, 2.7 μm ZBLAN fiber laser, and 1.5 μm single-frequency fiber laser over the past decade.

1.2 Road-blocks to High Power Fiber Lasers and Amplifiers

It should be emphasized that, all the record breaking fiber lasers [6-8] were based on large-mode-area fiber design, an effective solution to overcome power scaling constraints of conventional SM fiber lasers defined by nonlinear effects, thermo-optic effects, and optical damage.

Because of the high power, tight signal beam confinement, and long length, well-known fiber nonlinearities such as stimulated Raman scattering, stimulated Brillouin scattering (for narrow-linewidth beams), and self-phase modulation (for pulse light) occur quite readily in cladding-pumped fibers. Stimulated Raman scattering and stimulated Brillouin scattering results from stimulated inelastic scattering processes, whereby the radiation transfers a part of its energy to the glass host in the form of excited vibrational modes. Both manifest themselves as a significant power loss mechanism in fiber-based laser systems. In general, the nonlinearity coefficients in glass fibers are intrinsically small. Nevertheless, due to the large product of intensity and interaction length inside the fiber core nonlinearity can be strong and deteriorate the performance of high power fiber devices. Basically, for silica fiber devices, nonlinearity limits the performance of active fiber systems before limits due to thermo-optical effects or fracture of the fiber are reached.

Since the heat generated in the laser pumping cycle is distributed over a considerably long length, the chief advantage of fiber lasers over bulk solid-state lasers is their outstanding heat-dissipation capability due to the large outer surface area of the fiber allowing effective heat dissipation with minimal heat-sinking requirements. Nevertheless, heat generation can still destroy an optical fiber, via thermal damage of the coating, fracture, or even melting of the core, during a very high power operation. Besides thermo-optic effect, optical damage is also a hindrance of power scaling of fiber lasers utilizing convention SM fiber. For soft-glass fiber lasers [7, 8], thermo-optic effect and optical damage always happen at a power level much lower than that for the occurrence of nonlinear phenomena.

Large-mode-area SM fibers can be realized either by precise control of the index step between the core and cladding, or by use of microstructured fiber. For instance, NP Photonics demonstrated Tm (1800 nm) fiber lasers based on active SM fiber with core diameter of 42 μm [9]; Limpert demonstrated a 320 W SM photonic crystal fiber laser with core diameter of 60 μm [10]. However, the emission of the large-mode-area SM fibers is not a strict diffraction-limited single-transverse-mode.

Utilizing active multimode (MM) fibers is an alternative approach to increase mode volume and boost power levels of SM emission. Diffraction-limited outputs from active MM fibers can be obtained by introducing a discrimination mechanism between the

various fiber modes which suppresses the transverse modes other than the fundamental mode. Fundamental-mode surviving mechanisms can be realized, e.g., by adjusting fiber index and doping distribution [11, 12], by introducing special cavity configurations [13, 14], by coiling the MM fiber [15], or by designing helical-core [16] or leakage channel fibers [17, 18]. Utilizing beam cleanup effects based on stimulated Raman scattering [19] and stimulated Brillouin scattering [20] has also been proposed to obtain diffraction-limited emissions from MM fiber lasers.

1.3 New Method of Removing the Road-blocks

However, robust and environmentally stable fundamental-mode operation is only possible in a true single-mode fiber. In this thesis, a new concept to achieve true single-transverse-mode output from an active MM fiber is proposed and demonstrated. By splicing a passive SM fiber onto a short rare-earth doped MM fiber, diffraction-limited output with a beam quality (M^2) is equal to that of the SM fiber can be obtained from a highly efficient diode-pumped MMI fiber laser as a consequence of the self-imaging property of multimode interference (MMI) in the MM fiber segment. In contrast to other approaches of obtaining SM emission from active MM fibers [11]-[20], MMI fiber lasers are easy to construct and do not need any specially-designed fibers. Furthermore, MMI fiber lasers can provide perfect beam quality and intrinsically narrow emission linewidth.

1.4 Outline of the Dissertation

Since MMI is the essence of proposed fiber devices and there are few physical insights into self-imaging in MM fibers, in comparison to the intensive and thorough investigations of MMI in planar waveguides, MMI in optical fibers and its properties are described in detail and investigated experimentally and theoretically in Chapter 2.

The first MMI fiber laser and its characteristics are presented in Chapter 3. High power MMI fiber lasers and amplifiers are also proposed and investigated in this chapter.

On the other hand, MMI fiber devices can be used to generate nondiffracting beams. The principle and the properties of the MMI fiber devices are presented in Chapter 4. In contrast to other methods of generating nondiffracting beams or optical arrays, this method is not only extremely simple and flexible, but also power scalable under recent dramatic progress of high power fiber lasers and amplifiers. MMI fiber devices to generate high power nondiffracting beams are also proposed in this chapter.

In Chapter 5, the summary of my thesis and the prospect of my work are given.

CHAPTER 2

MULIMODE INTERFERENCE IN OPTICAL FIBERS

When an arbitrary electromagnetic field is coupled into a multimode (MM) waveguide, a specific set of eigenmodes of the MM waveguide are excited and each of them propagates along the waveguide independently with its own propagation constant. All the excited modes interfere with each other (called multimode interference) and the field at any position inside the MM waveguide is a superposition of their mode fields. Although the superposition of these excited modes generally yields a complicated field distribution due to multiple interferences (MMI), self-imaging of the input field can be obtained at certain positions where the excited modes are in phase. Such positions can be determined using the condition that the accumulated phase difference between any two excited modes is an integer multiple of 2π . Self-imaging in planar waveguides was first demonstrated by Ulrich [21] and was found to be an inherent property of MM waveguides.

After the first demonstration of MMI-based self-imaging in planar waveguide, MMI in planar waveguides has been intensively investigated and the self-imaging effect has been widely utilized in the design and fabrication of high-performance waveguide couplers [22]. Although MMI in cylindrical optical fibers is more complicated than that

in planar waveguides, the self-imaging effect in MM fibers was first observed by Allison [23] and has been experimentally demonstrated by several groups in recent years for various applications such as wavelength tunable laser [24], all-fiber bandpass filter [25], wavelength tunable fiber lens [26], and fiber-optic displacement sensor [27]. Compared to the intensive and thorough investigations of self-imaging in planar waveguides, there are few physical insights into self-imaging in MM fibers, even though a lot of fiber devices based on MMI have been demonstrated. In this chapter, the theory of MMI in MM fibers is described first. Then the properties of self-imaging in MM fibers are investigated in detail through theoretical calculations and experiments.

2.1 Theory of MMI in Multimode Fibers

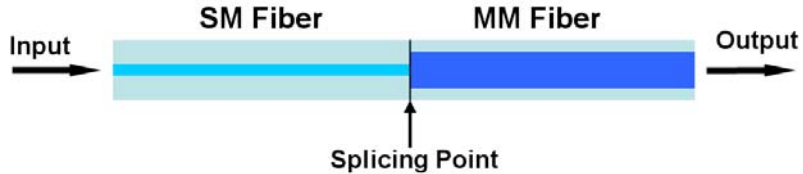


Fig. 2.1. A simple fiber structure for studying the self-imaging properties of MM optical fibers.

The central structure of an MMI fiber device is an MM fiber that supports many modes. In a common design, as depicted in Fig. 2.1, a single-mode (SM) fiber is spliced onto the MM fiber to ensure that a single-spatial-mode is launched into and recovered from the MM fiber segment.

Neglecting the reflected field as well as the power coupled to the radiation modes, in the plane of the splicing point ($z = 0$), the propagating field inside the SM fiber can be decomposed into the guided modes of the MM fiber, i.e.,

$$E_{SM}(r, \phi, z = 0) = \sum_1^N C_n e_n(r, \phi, z = 0), \quad (2.1)$$

where $E_{SM}(r, \phi, z = 0)$ is the fundamental mode of the SM fiber and $e_n(r, \phi, z = 0)$ is the n -th guided mode of the MM fiber. N is the number of excited modes inside the MM fiber. C_n is the mode expansion coefficient and can be determined from

$$C_n = \frac{\iint_S E_{SM}(r, \phi) \times e_n^*(r, \phi) ds}{\iint_S |e_n(r, \phi)|^2 ds}. \quad (2.2)$$

Neglecting mode conversion, all excited modes propagate independently inside the MM fiber, and the field $E_{MM}(r, \phi, z)$ along the MM fiber can be expressed as

$$E_{MM}(r, \phi, z) = \sum_1^N C_n e_n(r, \phi, 0) e^{-i\beta_n z} = e^{-i\beta_1 z} \sum_1^N C_n e_n(r, \phi, 0) e^{-i(\beta_n - \beta_1)z}, \quad (2.3)$$

where β_1 and β_n are the propagation constants of the fundamental mode and the n -th excited mode of the MM fiber, respectively.

Clearly, at certain positions inside the MM fiber, the reproduction of the input field occurs, i.e., $E_{MM}(r, \phi, z_{self-imaging}) = E_{SM}(r, \phi, z = 0)$, if the following condition is satisfied for all N modes

$$(\beta_n - \beta_1)z_{self-imaging} = \Delta\beta_n z_{self-imaging} = m_n 2\pi. \quad (m_n \text{ integer}) \quad (2.4)$$

Eq. (2.4) implies that the phase different between any two excited modes is an integer multiple of 2π , i.e., all excited modes are in phase.

In general, the propagation constants of the guided modes of an MM fiber should be evaluated through numerical approaches to solve the characteristic equation for the step-index fiber

$$\frac{\beta^2 v^2}{a^2} \left[\frac{1}{\gamma^2} + \frac{1}{\kappa^2} \right]^2 = \left[\frac{J'_v(\kappa a)}{\kappa J_v(\kappa a)} + \frac{K'_v(\gamma a)}{\gamma K_v(\gamma a)} \right] \cdot \left[\frac{k_0^2 n_{core}^2 J'_v(\kappa a)}{\kappa J_v(\kappa a)} + \frac{k_0^2 n_{cladding}^2 K'_v(\gamma a)}{\gamma K_v(\gamma a)} \right]. \quad (2.5)$$

where, a is the radius of the fiber core, v is the angular mode number, $\gamma^2 = \beta^2 - k_0^2 n^2$, $\kappa^2 = k_0^2 n^2 - \beta^2$, $k_0 = 2\pi/\lambda$; J_v and K_v are the Bessel function of the first and the second kind, respectively.

It should be noted that, due to the mode orthogonality and the on-axis excitation, only $HE_{1,n}$ modes ($v = 1$), also called $LP_{0,n}$ modes in linear polarization approximation, are strongly excited in the MM fiber segment of the MMI structure depicted in Fig. 2.1. And more modes are excited when a larger core MM fiber or a smaller SM fiber is used. For instance, when the MM fiber has a core diameter of 25 μm and a numerical aperture (NA) of 0.22 and the launching fiber is a conventional SMF-28 fiber, only the first four HE modes are strongly excited. The field distribution of the excited modes and their in-phase superposition are plotted in Fig. 2.2. When the core diameter of the MM fiber changes to 50 μm and 105 μm , first seven and fourteen HE modes are found to be strongly excited, respectively. The field distribution of the excited modes and their in-phase superposition are plotted in Fig. 2.3 and Fig. 2.4, respectively. Clearly, if all the excited modes are in phase, a precise self-imaging of the input field occurs.

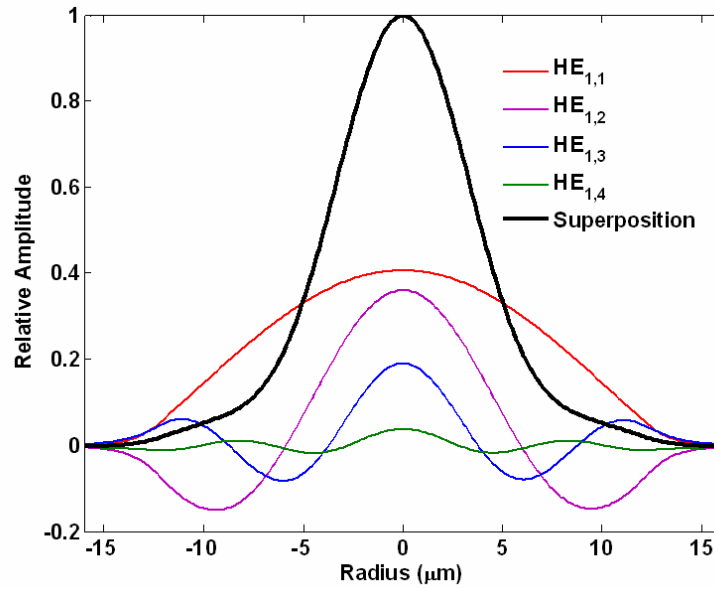


Fig. 2.2. Field distributions of the excited modes and their in-phase superposition in a 25 μm MM fiber segment of the MMI structure when the launching fiber is an SMF-28.

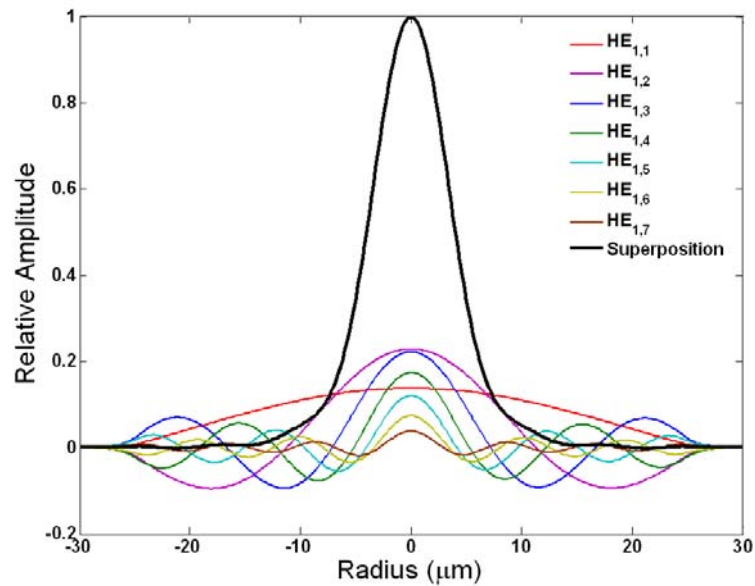


Fig. 2.3. Field distributions of the excited modes and their in-phase superposition in a 50 μm MM fiber segment of the MMI structure when the launching fiber is an SMF-28.

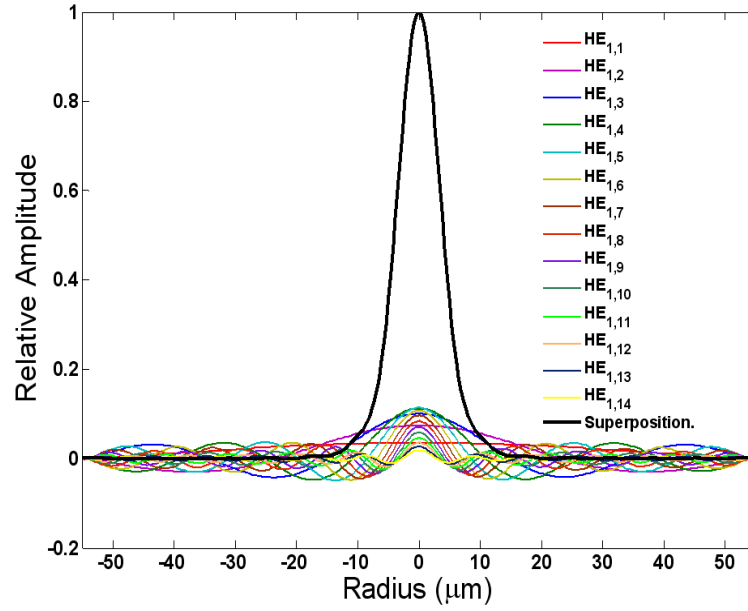


Fig. 2.4. Field distributions of the excited modes and their in-phase superposition in a 105 μm MM fiber segment of the MMI structure when the launching fiber is an SMF-28.

2.2 Self-imaging in Multimode Fibers and Its Properties

As analyzed in Section 2.1, it is straightforward that a reproduction of the input field can happen at positions where all the excited modes are in phase. However, the situation in optical fibers is much complicated because the propagation constants of the excited modes in optical fibers do not have multiple relationships between each other like in planar waveguides. Therefore, numerical approaches including the mode expansion approach and the beam propagation method have been employed to analyze the self-imaging in MM fibers. In this thesis, the fully vectorial mode expansion approach, developed by Li [28], is used to do the calculations.

With the mode expansion approach, the evolution of the intensity distribution along the MM fiber segment for the input field from an SMF-28 fiber is plotted in Figs. 2.5-2.7 for MM fibers with a NA of 0.22 and core diameters of 25 μm , 50 μm , and 105 μm . It is obvious that the positions for the self-imaging occurrence and the quality of the self-imaging are much different for the three MM fibers. For the 25 μm fiber, a quasi-reproduction of the input field occurs at every 0.55 mm and a nearly perfect reproduction occurs at every 2.2 mm. For the 50 μm and 105 μm fibers, however, only quasi-reproduction of the input field occurs at a much longer propagation distance. Therefore, detailed investigations of the self-imaging effect in optical fibers are necessary

for further design of MMI-based fiber lasers and amplifiers and are also beneficial for the design and optimization of the MMI fiber devices that have been demonstrated previously [24-27]

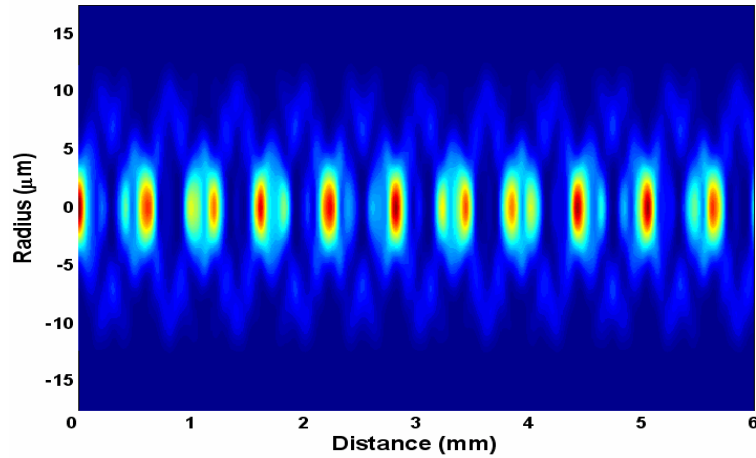


Fig. 2.5. Intensity distribution in a 25 μm MM fiber segment of the MMI structure when the field of an SMF-28 is launched.

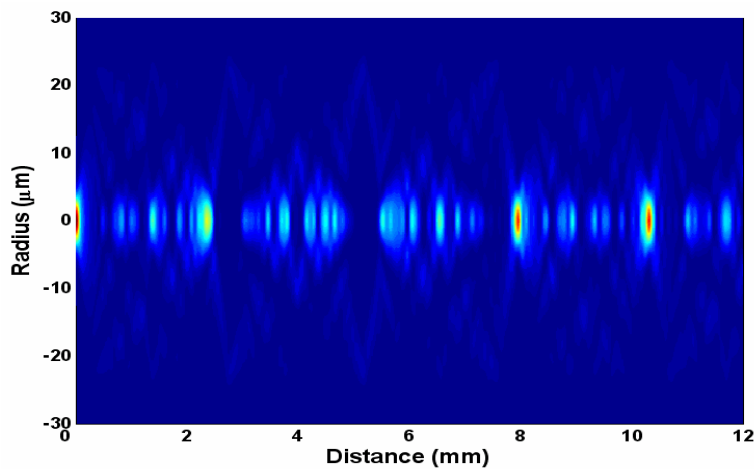


Fig. 2.6. Intensity distribution in a 50 μm MM fiber segment of the MMI structure when the field of an SMF-28 is launched.

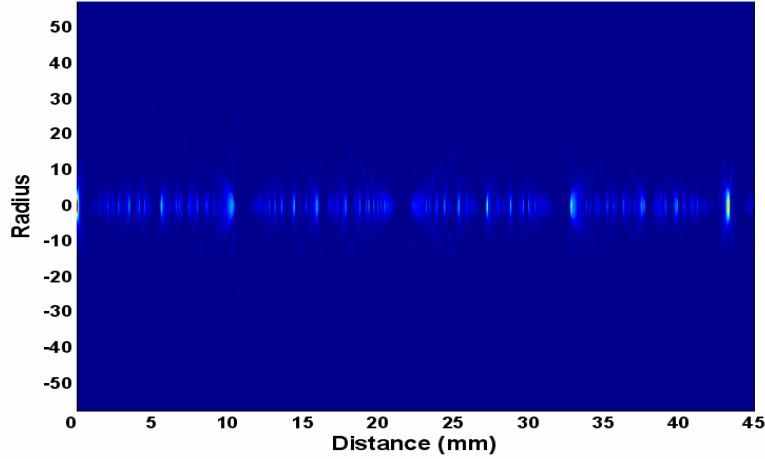


Fig. 2.7. Intensity distribution in a 105 μm MM fiber segment of the MMI structure when the signal from a SMF-28 is launched.

2.2.1 Self-imaging quality factor

Although the intensity distributions shown in Figs. 2.5-2.7 have given a distinct comparison for the self-imaging in different MM fibers, quantitative evaluation of the self-imaging properties is very necessary. Here, a factor γ defined as an effective amplitude reflection coefficient in [28] can be redefined for MMI fiber structures by

$$\gamma(z) = \frac{\left| \iint E_{MM}(r, \phi, z) E_{MM}^*(r, \phi, 0) r dr d\phi \right|}{\iint |E_{MM}(r, \phi, 0)|^2 r dr d\phi}. \quad (2.6)$$

The self-imaging quality factor $\gamma(z)$ reflects the quality of the reproduction of the input field at the position z inside the MM fiber.

The quality factor γ of self-imaging in the 25 μm MM fiber for a single-frequency ($\lambda = 1.535 \mu\text{m}$) input field from a standard SM fiber (SMF-28) are plotted in Fig. 2.8. Clearly, quasi-reproduction peaks with quality factor $\gamma > 0.9$ and perfect self-imaging peaks with quality factor $\gamma > 0.99$ can be obtained at a lot of positions.

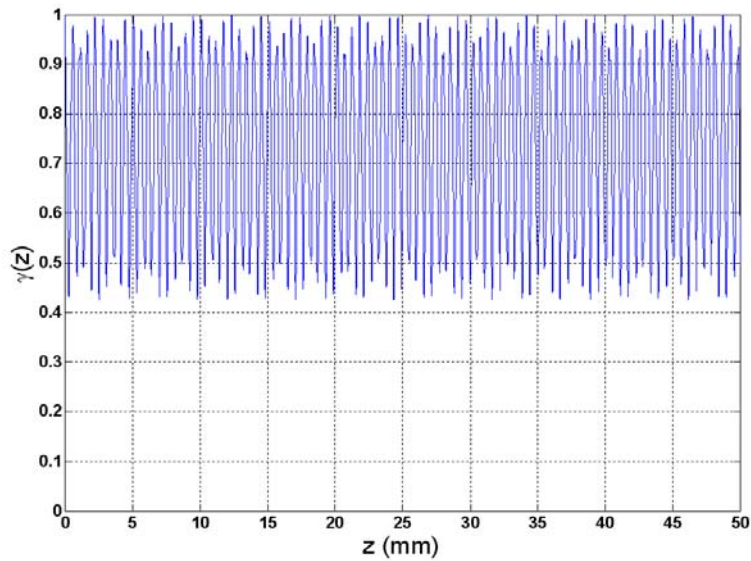


Fig. 2.8. Self-imaging quality factor γ along the MM fiber segment with a core diameter of 25 μm for the input field from an SMF-28 fiber.

The quality factor γ of self-imaging of the input field from an SMF-28 is plotted in Figs. 2.9 and 2.10 for the 50 μm and 105 μm MM fibers, respectively. In both cases,

perfect self-imaging ($\gamma > 0.99$) cannot be obtained. However, a quasi-reproduction of the input field with a self-imaging quality factor $\gamma > 0.9$ still occurs at certain positions inside the MM fiber. For example, a self-image of the input field with $\gamma > 0.97$ can be obtained at $z = 10.3$ mm in the $50\ \mu\text{m}$ or 43.28 mm in the $105\ \mu\text{m}$ MM fiber, respectively.

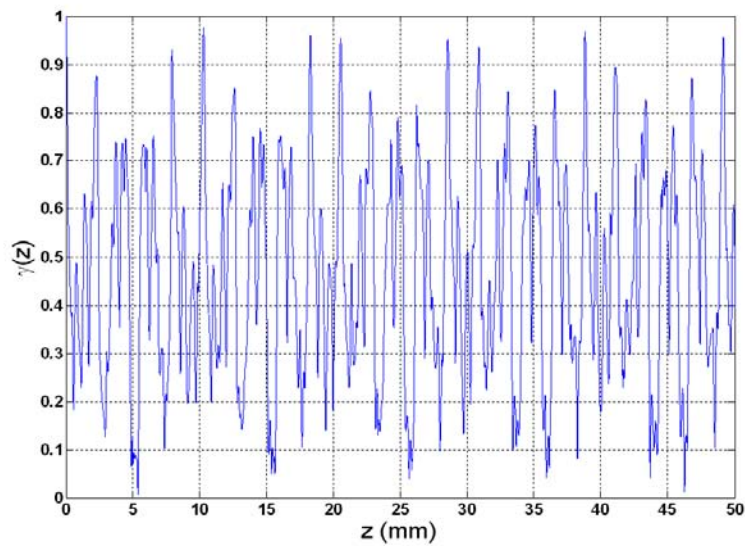


Fig. 2.9. Self-imaging quality factor γ along the MM fiber segment with a core diameter of $50\ \mu\text{m}$ for the input field from an SMF-28 fiber.

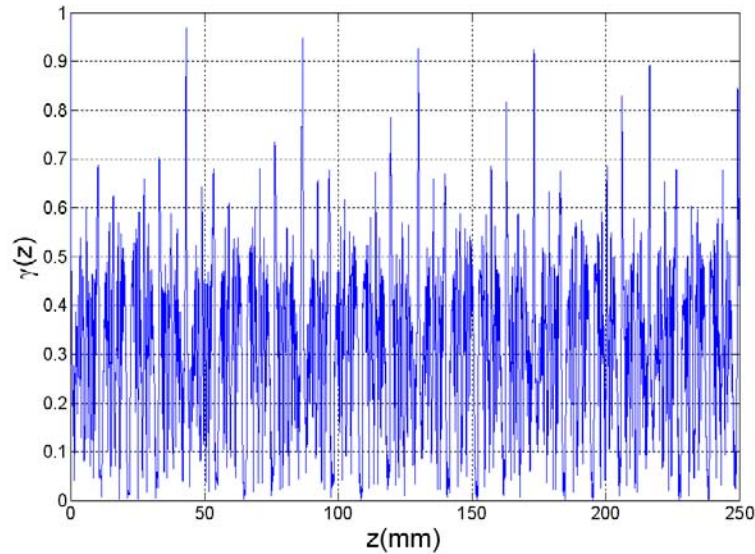


Fig. 2.10. Self-imaging quality factor γ along the MM fiber segment with a core diameter of $105 \mu\text{m}$ for the input field from an SMF-28 fiber.

Based on the simulation results of the $25 \mu\text{m}$, $50 \mu\text{m}$, and $105 \mu\text{m}$ fibers, it is straightforward that the self-imaging quality should reduce with the core diameter of the MM fiber segment. To see how the self-imaging quality changes with the core diameter, the maximum quality factor γ within a 1-m MM fiber segment with respect to the core diameter is plotted in Fig. 2.11. As the core diameter of the MM fiber segment is larger than $250 \mu\text{m}$, the self-imaging quality reduces evidently with the core diameter. When the core diameter is $500 \mu\text{m}$, the self-imaging quality factor is only 0.69.

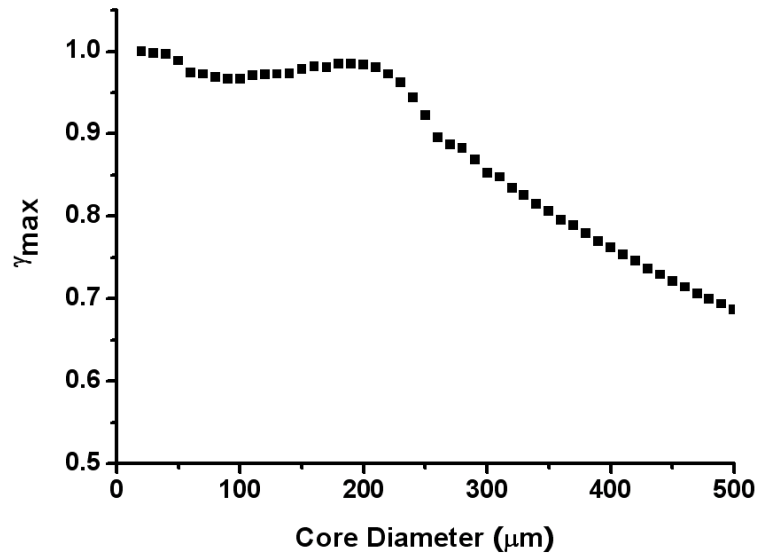


Fig. 2.11. The maximum self-imaging quality factor γ_{max} within one meter MM fiber segment of different core diameters.

2.2.2 Self-imaging length interval

In Figs. 2.9 and 2.10, the self-imaging length interval inside the 50 μm fiber is about 10.3 mm and that inside the 105 μm fiber is about 43.28 mm. It is obvious that, as the core size increases, the self-imaging length interval or the self-imaging period increases accordingly, as a result of more excited modes. The variation of the self-imaging length interval with the core size of a MM fiber is plotted in Fig. 2.12. Since self-imaging is

never 100% perfect, periodical peaks whose values are obviously larger than their neighbor peaks are defined as the self-imaging peaks. It is found that the self-imaging length interval $L_{\text{self-imaging}}$ increases quadratically with the core diameter d_m and $L_{\text{self-imaging}} = 4040d_m^2/\text{mm}$ is a very good approximation. For instance, when the core diameter is 200 μm , $L_{\text{self-imaging}} = 153.8 \text{ mm}$. It means that the length of the MM fiber segment must be multiple of 153.8 mm to obtain high quality self-imaging. Because random mode conversion, a major factor for MMI fiber device loss, increases with the fiber core size and the fiber length, when a large-core MM fiber is used, its length should be chosen with more considerations.

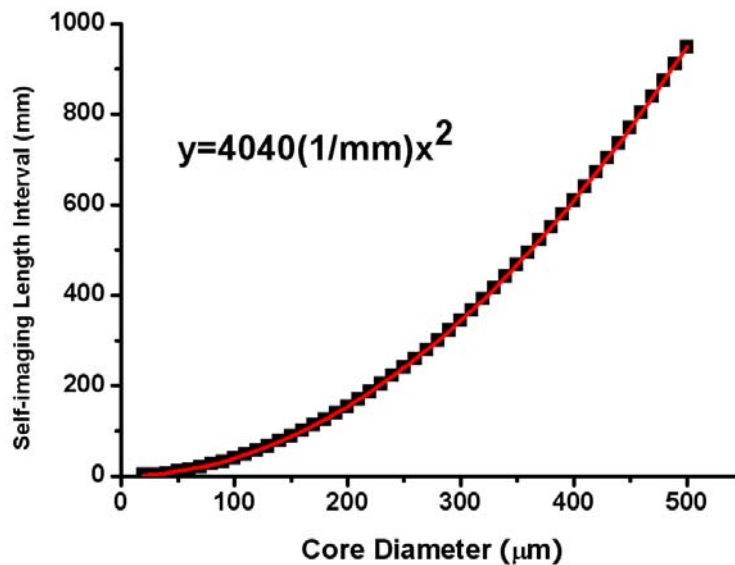


Fig. 2.12. The self-imaging length interval within one meter MM fiber segment of different core diameters.

2.2.3 Phase difference between excited modes for self-imaging

Because multiple modes (≥ 4) are excited and their propagation constants do not have a multiple relationship between each other, it is impossible to find a position exactly satisfying the condition defined by Eq. (2.4) within a practical fiber length (several meters). However, it is found that self-imaging of the input field can occur when the phase differences between the strongly excited modes are slightly different from 2π .

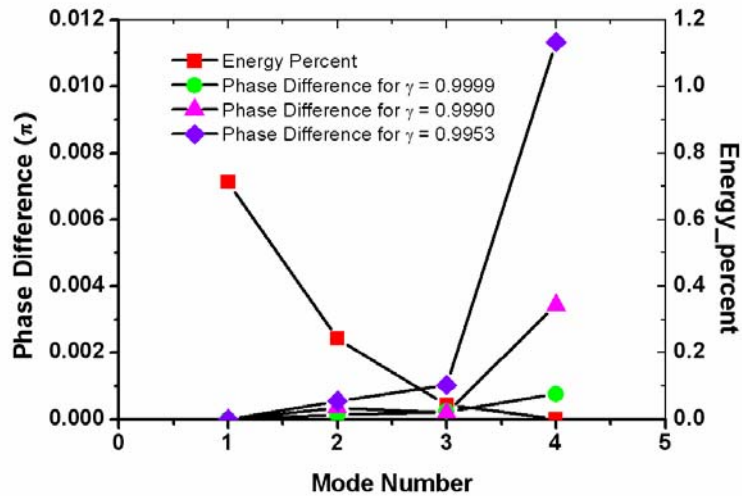


Fig. 2.13. Energy percentage of the excited modes and the phase differences between the excited modes and the peak mode at three self-imaging positions inside the 25 μm MM fiber.

When the core diameter of the MM fiber is $25\ \mu\text{m}$, the energy percentage of the excited modes and the phase differences between all the other excited modes and the peak mode (the excited mode of the highest energy) for three self-imaging peaks are plotted in Fig. 2.13. Clearly, when the phase differences between the excited modes are less than 0.012π , perfect self-imaging with $\gamma > 0.99$ is achieved. And the smaller the phase differences, the larger the self-imaging quality factor.

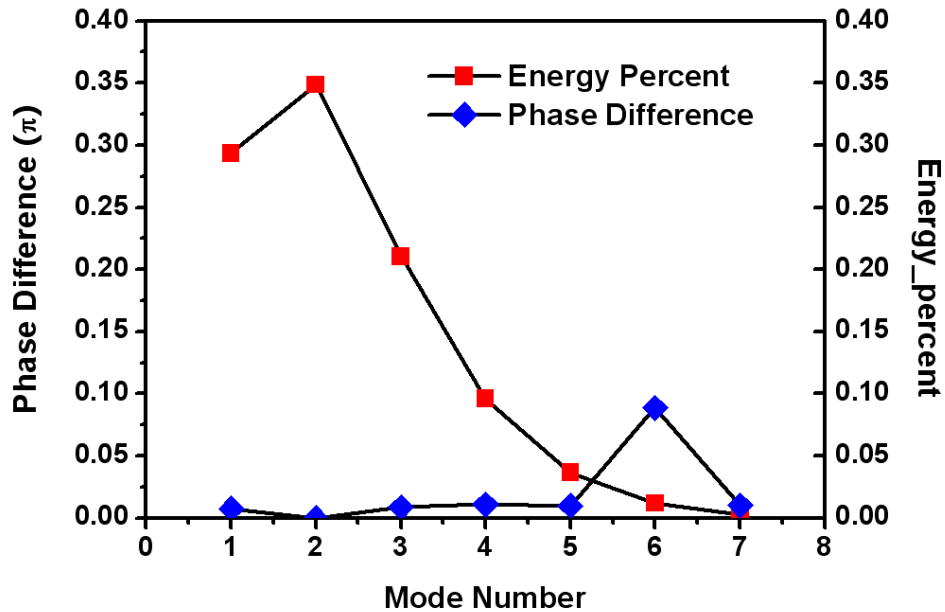


Fig. 2.14. Energy percentage of the excited modes and the phase differences at a self-imaging point between the excited modes and the mode of highest intensity inside $50\ \mu\text{m}$ MM fiber.

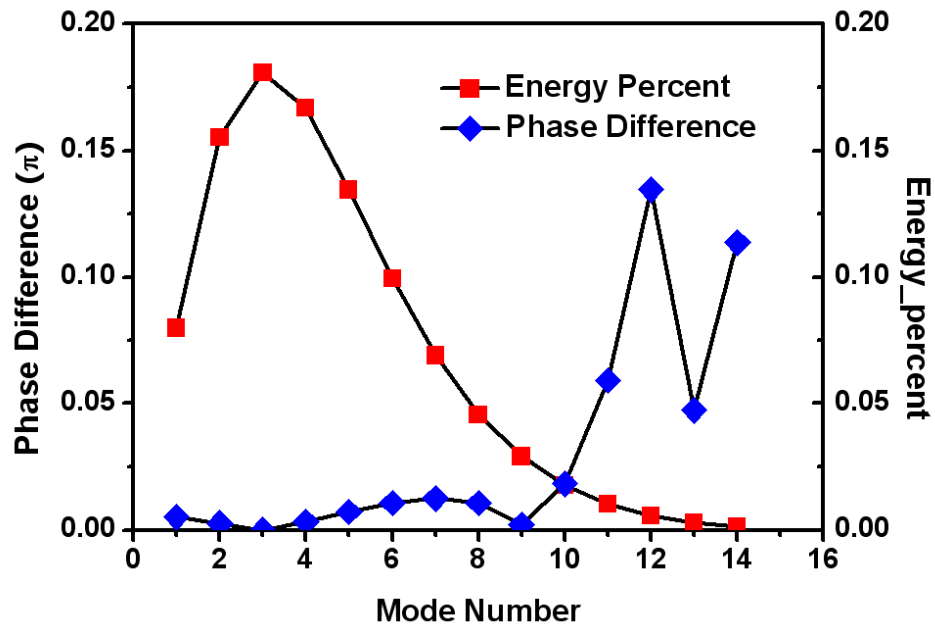


Fig. 2.15. Energy percentage of the excited modes and the phase differences at a self-imaging point between the excited modes and the mode of highest intensity inside the 105 μm MM fiber.

In the cases of 50 μm and 105 μm fibers, the energy percentage of the excited modes and the phase differences between all the other excited modes and the peak mode for the self-imaging peaks at 10.3 mm and 43.28 mm are plotted in Figs. 2.14 and 2.15, respectively. Clearly, self-imaging, strictly speaking, the quasi-reproduction of input field, can still occur even when the phase differences between the excited modes are slightly

different from 2π . For the 50 μm MM fiber almost perfect self-imaging with $\gamma = 0.976$ is achieved despite phase mismatches up to 0.01π for strongly excited modes and up to 0.1π for modes with smaller contributions. For the 105 μm MM fiber almost perfect self-imaging with $\gamma = 0.97$ is achieved despite phase mismatches up to 0.02π for strongly excited modes and up to 0.15π for modes with smaller contributions.

2.2.4 Self-imaging behavior in wavelength representation

In above sections, self-imaging along the MM fiber is analyzed for a specific wavelength. However, for an MM fiber segment with a fixed length, reproduction of the input field at its output facet can only occur for certain wavelengths (also called self-imaging wavelengths). This phenomenon is called spectral filtering effect of MMI. Self-imaging occurs when the following condition that derived from Eq. (2.4) is satisfied,

$$\Delta n_{eff,n} L = m_n \lambda, \quad (m_n \text{ integer}, n = 2, 3, \dots, N) \quad (2.7)$$

where L is the MM fiber length, λ is the signal wavelength, and $\Delta n_{eff,n} = (\beta_n - \beta_1)\lambda/2\pi$.

For instance, for the 50 μm MM fiber with a length of 200 mm, self-imaging with $\gamma > 0.9$ only occurs at 1524 nm and 1579 nm, shown in Fig. 2.16 by the self-imaging quality in a wavelength range from 1500 nm to 1600 nm. Seen from Eq. (2.7), it is obvious that the self-imaging wavelengths are different for the MM fiber with different lengths. To

illuminate the difference, the self-imaging quality of the output from an MMI fiber structure shown in Fig. 2.1 with respect to wavelength for MM fiber lengths of 199.8 mm and 200.2 mm is also plotted in Fig. 2.16. Clearly, self-imaging moves to shorter wavelength as the MM fiber becomes longer.

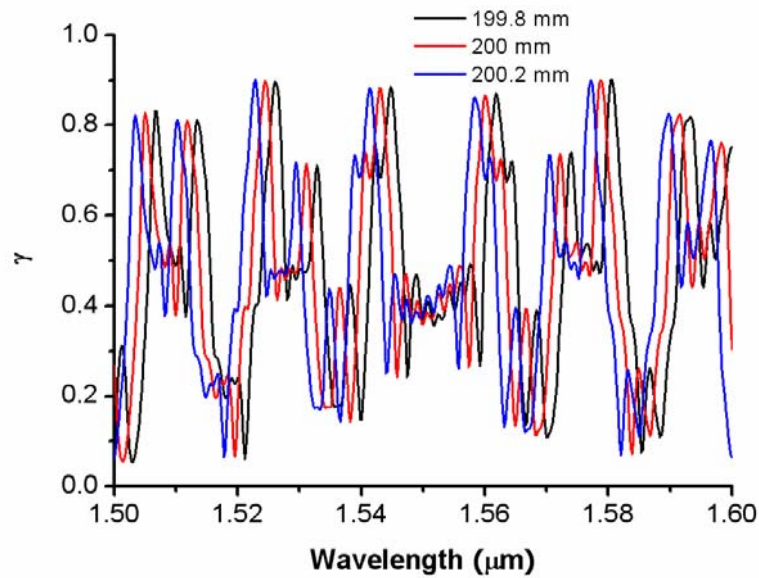


Fig. 2.16. Self-imaging quality with respect to wavelength for 199.9 mm, 200 mm, and 200.2 mm long 50 μm MM fibers, respectively.

Derived from Eq. (2.7) by taking the differential of λ and L , respectively, two important parameters that describe the self-imaging properties in spectrum domain, the wavelength interval of self-imaging $\Delta\lambda_{\text{im}}$ and the wavelength shift relative to the change

of the MM fiber length $d\lambda/dL$, can be given by individual formula for each excited modes as follows,

$$\Delta\lambda_{im,n} = \frac{1}{\frac{L}{\lambda} \left| \frac{d\Delta n_{eff,n}}{d\lambda} - \frac{\Delta n_{eff,n}}{\lambda} \right|} \quad (2.8)$$

$$\frac{d\lambda_n}{dL} = \frac{1}{L \left(\frac{1}{\lambda} - \frac{1}{\Delta n_{eff,n}} \frac{d\Delta n_{eff,n}}{d\lambda} \right)} \quad (2.9)$$

Although $\Delta\lambda_{im}$ and $d\lambda/dL$ are the collective behavior of each individual excited mode expressed by Eq. (2.8) and (2.9) and can be only evaluated from numerical approach, a conclusion can be drawn from the above equations that both $\Delta\lambda_{im}$ and $d\lambda/dL$ are inversed to the length of the MM fiber segment. In other words, the wavelength interval of self-imaging decreases with the MM fiber length and the shift of the self-imaging wavelength due to the variation of the fiber length is small when the MM fiber segment is long. In laboratory, the length control of the MM fiber segment is flexible and oriented if $\Delta\lambda_{im}$ and $d\lambda/dL$ are known. However, since both parameters defined by Eq. (2.8) and (2.9) depend on the total length of the MM fiber segment, it is necessary to define two new parameters independent of the fiber length, $\Delta\lambda_{im}L$ and $d\lambda/(dL/L)$. Parameters of individual mode, $\Delta\lambda_{im,n}L$ and $d\lambda_n/(dL/L)$, and their collection, $\Delta\lambda_{im}L$ and $d\lambda/(dL/L)$ of the

50 μm and 105 μm fiber are plotted in Figs. 2.17-2.20, respectively. Based on the behavior of the individual parameters and their collective behavior, the following conclusions can be drawn for $\Delta\lambda_{\text{im}}L$ and $d\lambda/(dL/L)$: (1) wavelength dependence of $\Delta\lambda_{\text{im}}L$ is very small; (2) $d\lambda/(dL/L)$ is negative, indicating that the self-imaging wavelength shifts towards shorter wavelength as the fiber length increases; (3) $\Delta\lambda_{\text{im}}L$ of the 50 μm fiber is smaller than that of the 105 μm fiber; and (4) $|d\lambda/(dL/L)|$ of the 50 μm fiber is larger than that of the 105 μm fiber.

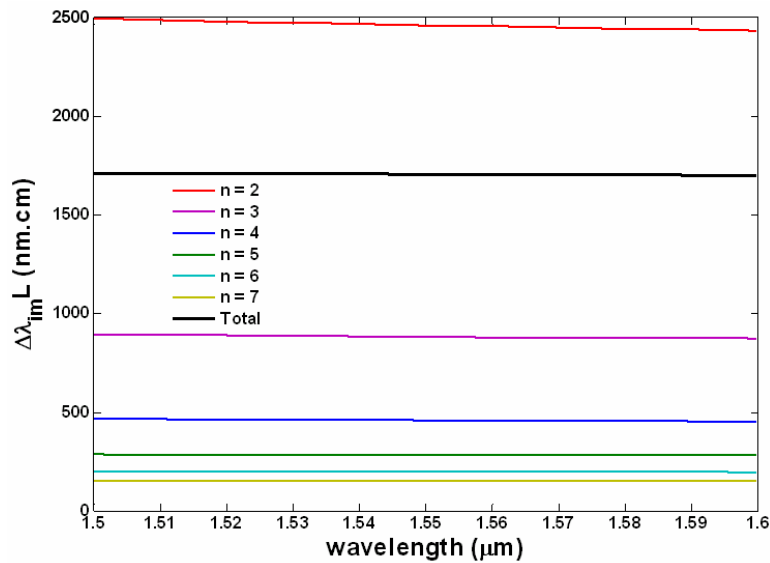


Fig. 2.17. Individual parameters $\Delta\lambda_{\text{im},n}L$ and their collective behavior $\Delta\lambda_{\text{im}}L$ of the 50 μm fiber are plotted in a wavelength range of 1.5-1.6 μm .

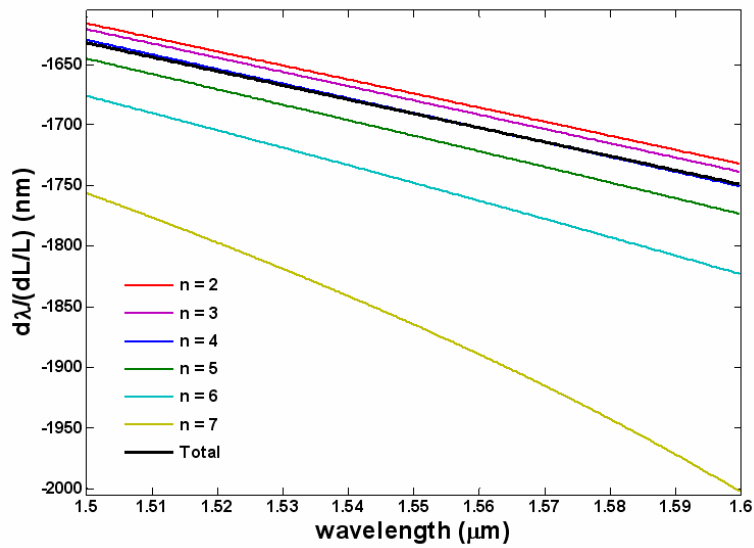


Fig. 2.18. Individual parameters $d\lambda_n/(dL/L)$ and their collective behavior $d\lambda/(dL/L)$ of the 50 μm fiber are plotted in a wavelength range of 1.5-1.6 μm .

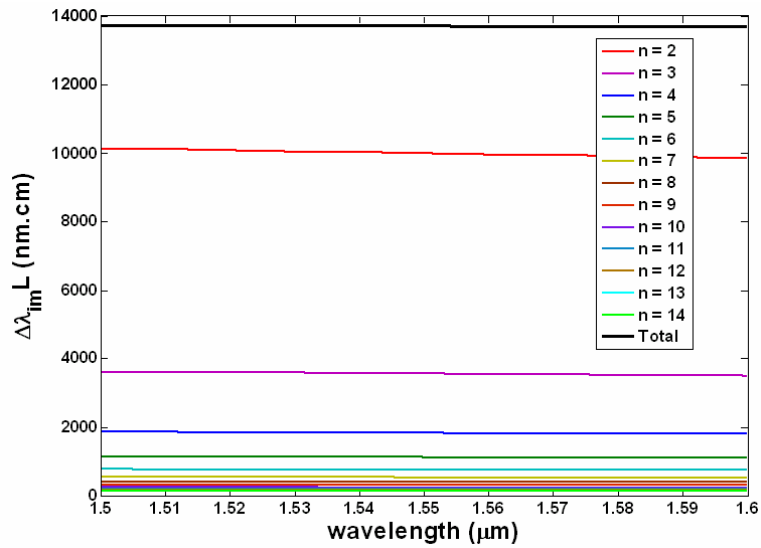


Fig. 2.19. Individual parameters $\Delta\lambda_{im,n}L$ and their collective behavior $\Delta\lambda_{im}L$ of the 105 μm fiber are plotted in a wavelength range of 1.5-1.6 μm .

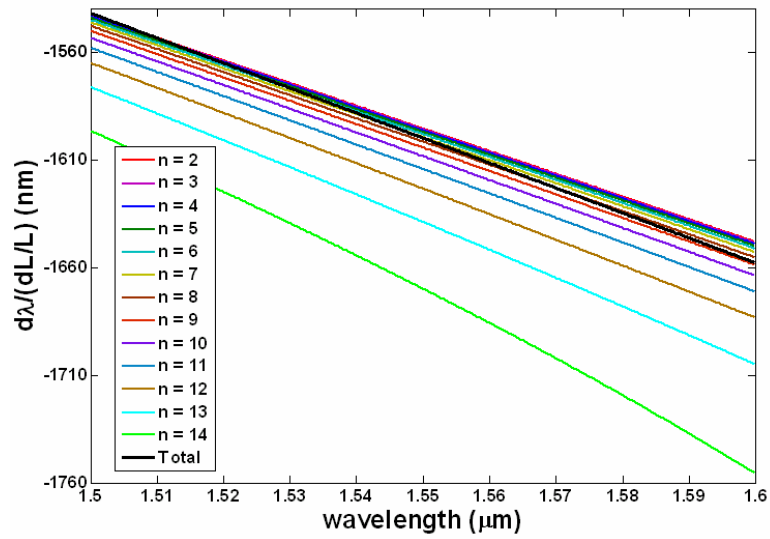


Fig. 2.20. Individual parameters $d\lambda_n/(dL/L)$ and their collective behavior $d\lambda_n/(dL/L)$ of the 105 μm fiber are plotted in a wavelength range of 1.5-1.6 μm .

2.3 Experimental Investigation of Self-imaging in Multimode Optical Fibers

In Section 2.2, the self-imaging properties of MM fibers have been analyzed theoretically.

In this section, the self-imaging properties are experimentally investigated. The key parameters to describe the self-imaging properties defined in Section 2.2 have also been evaluated quantitatively for the 50 μm and 105 μm fiber.

2.3.1 Direct observation of self-imaging inside an MM fiber

Since the light is guided inside the fiber core, it is hard to observe the self-imaging effect with a side view. In order to give a direct view of the intensity profile changing with positions inside the MM fibers, dozens of the 50 μm fiber segments with different lengths are prepared. The intensity profile is recorded by an infrared CCD camera by a setup shown in Fig. 2.21.

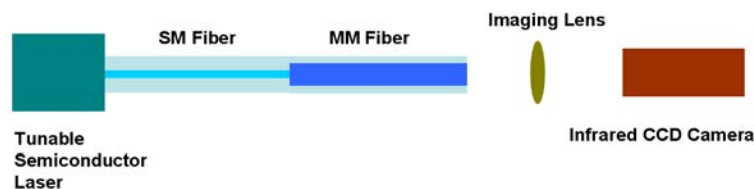


Fig. 2.21. Experiment setup for directly observing self-imaging in MM fibers.

The MM fiber segments are cleaved with different lengths around 49.1 mm, a self-imaging peak predicted by the calculation shown in Fig. 2.22. The intensity profiles at the fiber facet of the MM fiber segments are shown in Fig. 2.23. Clearly, when the MM fiber length is much far from the self-imaging position, the self-imaging quality is bad and the energy is distributed in a large region of the cross-section of the MM fiber. As the MM fiber segment length approaches the self-imaging position, the energy is almost accumulated at the central spot and the intensity profile resembles closely an input field from the SMF-28 fiber.

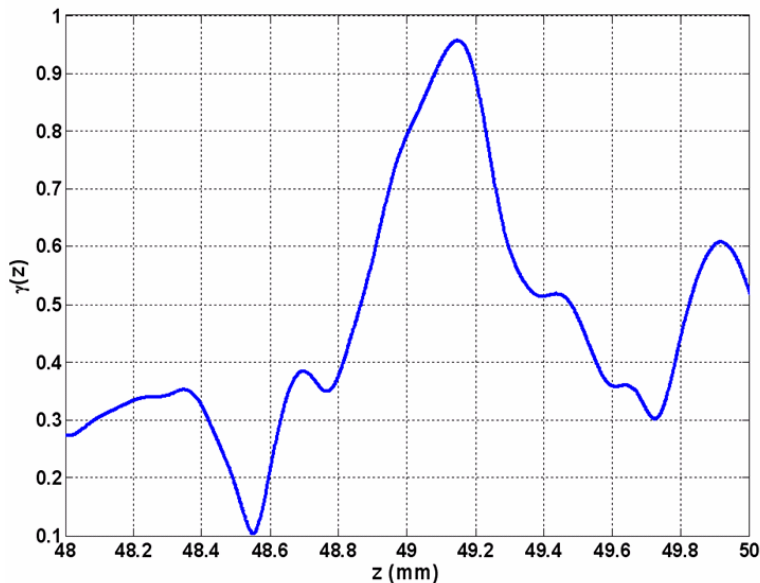


Fig. 2.22. Calculated self-imaging quality with respect to the position around 49.1 mm for the 50 μm fiber.

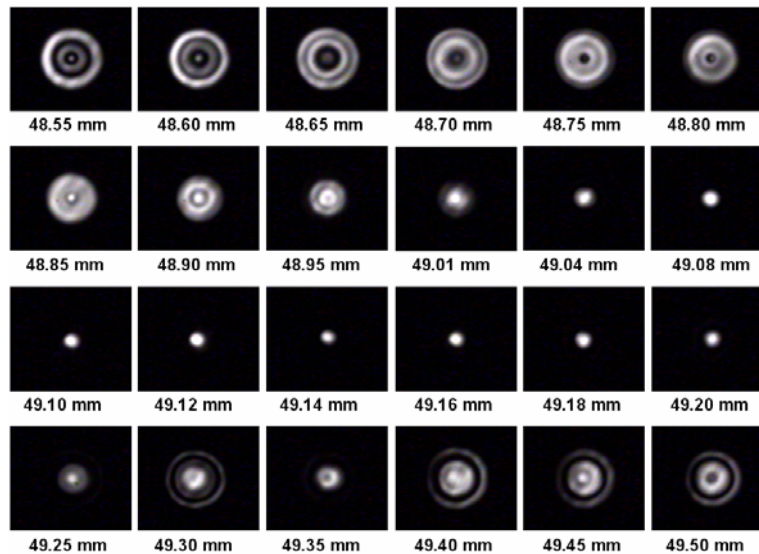


Fig. 2.23. Intensity profiles at positions around 49.1 mm inside the 50 μm fiber.

Based on the analyses in Section 2.2, the essence of MMI fiber lasers and amplifiers is to accurately control the length of the MM fiber segment, i.e., the length should correspond exactly to the self-imaging positions shown in Figs. 2.8-2.10. Based on the self-imaging peak shown in Fig. 2.22 and the intensity profile shown in Fig. 2.23, we can conclude that, a tolerance of $< 100 \mu\text{m}$ on length is required for a self-imaging quality $\gamma > 0.9$. It should be noted that, cleaving a fiber of tens of centimeters long with an accuracy of $10 \mu\text{m}$ can be achievable with commercial laboratory equipments.

2.3.2 Spectral filtering effect of MMI and its properties

Spectral filtering effect of MMI indicates that self-imaging occurs only for certain wavelengths which satisfy the condition expressed by Eq. (2.7). To experimentally investigate the behavior of self-imaging in the wavelength domain, the transmission spectrum of an MMI structure, as illustrated in Fig. 2.24, is measured with the length of the MM fiber segment varied. A fiber-coupled white light source is employed as the input source and SMF-28 is used for the SM fiber segments.

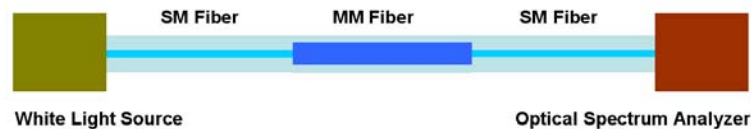


Fig. 2.24. Experimental setup for the transmission spectrum measurement of an MMI structure.

The transmission spectra of the MMI structure incorporating 50 μm and 105 μm MM fibers were measured for two different lengths of 20 cm and 100 cm of the MM fiber segment and are shown in Figs. 2.25 and 2.26. It is obvious that high transmission happens only at certain wavelengths. And the experimental results agree well with the

predictions based on Eqs. (2.8) and (2.9) that are discussed above, i.e., the wavelength interval of self-imaging $\Delta\lambda_{im}$ in the $L = 100$ cm long MM fiber is smaller than that in the $L = 20$ cm long MM fiber and the wavelength interval of self-imaging in the $105 \mu\text{m}$ fiber is larger than that in the $50 \mu\text{m}$ fiber because, as mentioned above, $\Delta\lambda_{im}L$ of the $105 \mu\text{m}$ fiber is larger than that of the $50 \mu\text{m}$ fiber.

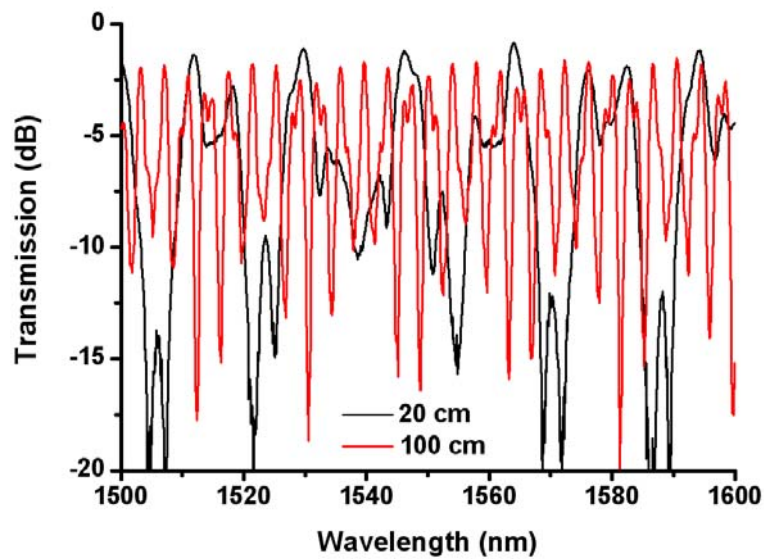


Fig. 2.25. Transmission spectra of MMI structures with fiber lengths of 20 cm and 100 cm and with a fiber core diameter of $50 \mu\text{m}$.

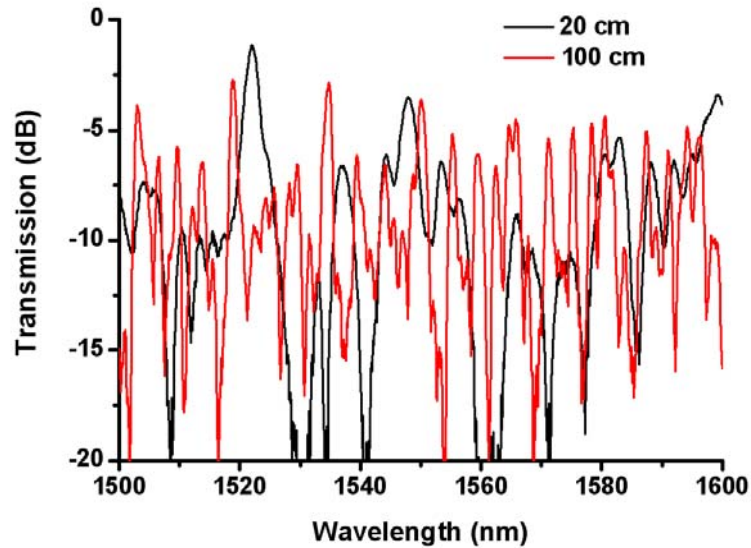


Fig. 2.26. Transmission spectra of MMI structures with fiber lengths of 20 cm and 100 cm and with a fiber core diameter of 105 μm .

To obtain the values of $\Delta\lambda_{\text{im}}L$ and $d\lambda/(dL/L)$ of self-imaging in the 50 and 105 μm MM fiber, MM fiber segments with different lengths were cut down with length intervals of 0.5 - 1 cm and the transmission spectra of the corresponding MMI structures were measured. The wavelength interval $\Delta\lambda_{\text{im}}$ and the wavelength shift $d\lambda/dL$ for 1 cm change of the MM fiber length can be obtained from the measured transmission spectra. The experimental results of $\Delta\lambda_{\text{im}}$ and $d\lambda/dL$ for the 50 and 105 μm fiber are plotted in Figs. 2.27 and 2.28, respectively. Here, self-imaging wavelengths are defined as periodical

transmission peaks with values larger than those of its neighboring peaks. The parameters $\Delta\lambda_{\text{im}}L$ and $d\lambda/(dL/L)$ can be obtained through fitting the experimental data with a reciprocal function. As shown in Figs. 2.27 and 2.28, $\Delta\lambda_{\text{im}}L$ of the 50 and 105 μm fiber are 1735.8 and 13583 nm·cm, respectively and $d\lambda/(dL/L)$ of the 50 and 105 μm fiber are -1745 and -1672.4 nm, respectively. It should be noted that, since $d\lambda/(dL/L)$ slightly depends on the wavelength, as shown in Figs. 2.18 and 2.20, the values we obtained are the average of $d\lambda/(dL/L)$ in the wavelength range of 1.5-1.6 μm .

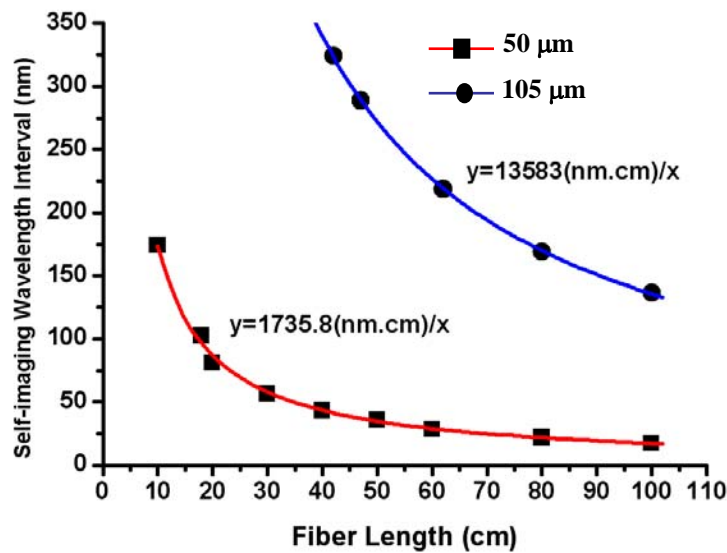


Fig. 2.27. The self-imaging wavelength interval of the MMI structure with different MM fiber lengths for the 50 μm and 105 μm fiber, respectively.

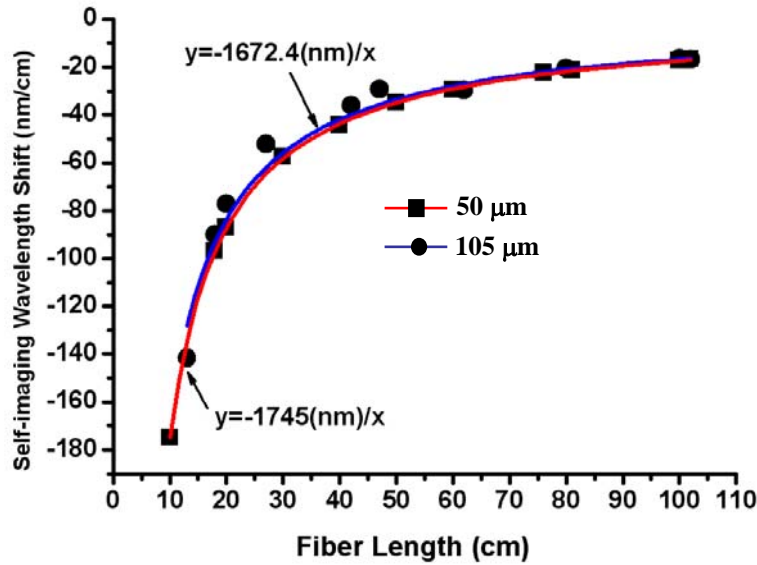


Fig. 2.28. The self-imaging wavelength shift for 1 cm change of the fiber length of the MMI structure with different MM fiber lengths for the 50 μm and 105 μm fiber, respectively.

2.3.3 Direct observation of self-imaging for different wavelengths

As have been demonstrated above, self-imaging quality changes with the signal wavelength for an MM fiber segment with a fixed length. In order to directly observe the self-imaging of the MM fiber, the field intensity distribution at the facet of the MM fiber segment of an experiment setup, as depicted in Fig. 2.21, was measured. A fiber-coupled

single-frequency semiconductor laser with a wavelength-tunable range of 1456-1584 nm was employed as the input source. The intensity distributions at the MM fiber output facet and of the corresponding far-field pattern were recorded by an infrared CCD camera. Self-imaging in the MM fiber was observed by tuning the wavelength of the input signal. After recording the intensity distribution, the transmission spectrum of the corresponding MMI structure was also measured by splicing the whole fiber segment to a SM fiber segment and using the experimental setup shown in Fig. 2.24.

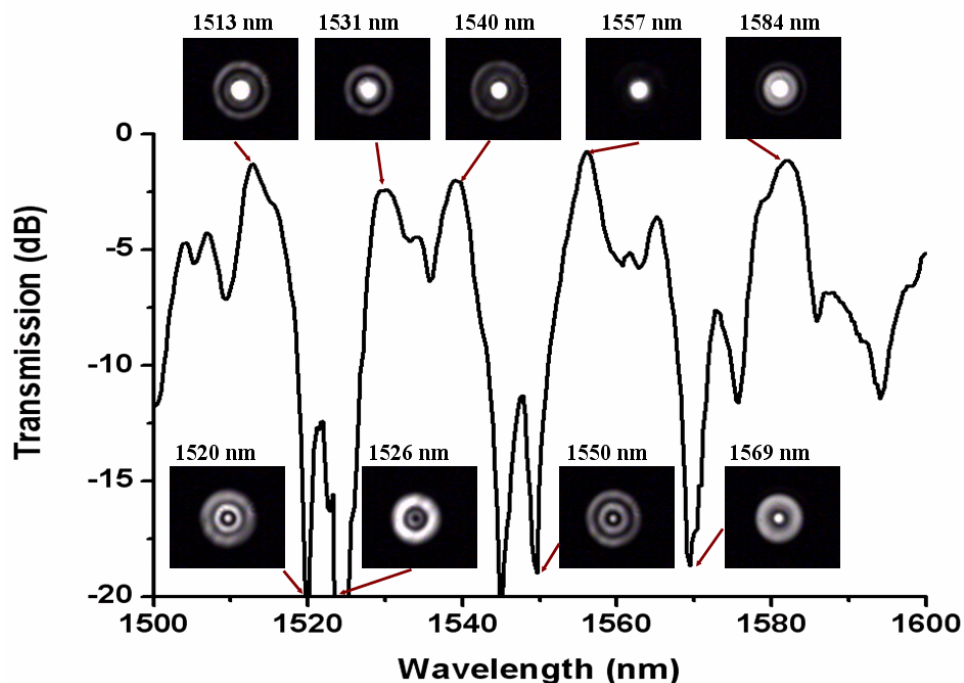


Fig. 2.29. The intensity distribution of the facet of the 50 μm MM fiber segment of a MMI structure when a tunable single-frequency signal is launched and the transmission spectrum of the corresponding MMI structure.

When a 15.0 cm long 50 μm MM fiber was used, the transmission spectrum and some typical intensity profiles at the MM fiber facet are shown in Fig. 2.29. Obviously, different intensity distributions were observed due to the complicated interference among the excited modes in the 50 μm MM fiber. When the signal wavelength λ equals 1513, 1531, 1540, 1557, or 1584 nm, the field has a very bright spot at the center of MM fiber and the corresponding transmission is large. Especially, at 1557 nm, the transmission is maximum (-0.75 dB) in the wavelength range and the intensity distribution at the MM fiber facet resembles the input field of the SM fiber. Therefore, 1557 nm is regarded as the self-imaging wavelength, and the low-intensity image of the MM fiber facet, the corresponding three-dimensional plot, and the far-field image are shown in Fig. 2.30. All results indicate that high-quality self-imaging can be obtained in the 50 μm MM fiber.

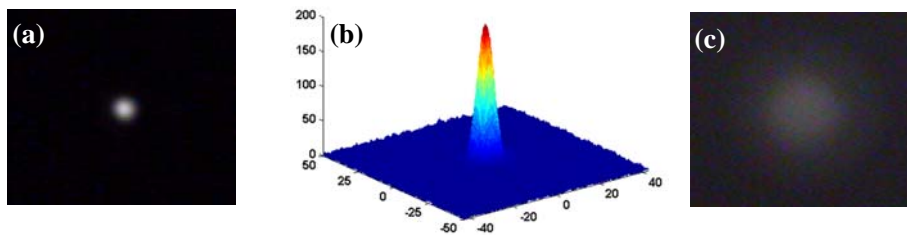


Fig. 2.30. The facet image, its three-dimensional plot, and the far-field image of the 50 μm MM fiber segment of a MMI structure when a signal of 1557 nm is input. (a) MM fiber facet image; (b) Three-dimensional plot of (a); (c) Far-field image.

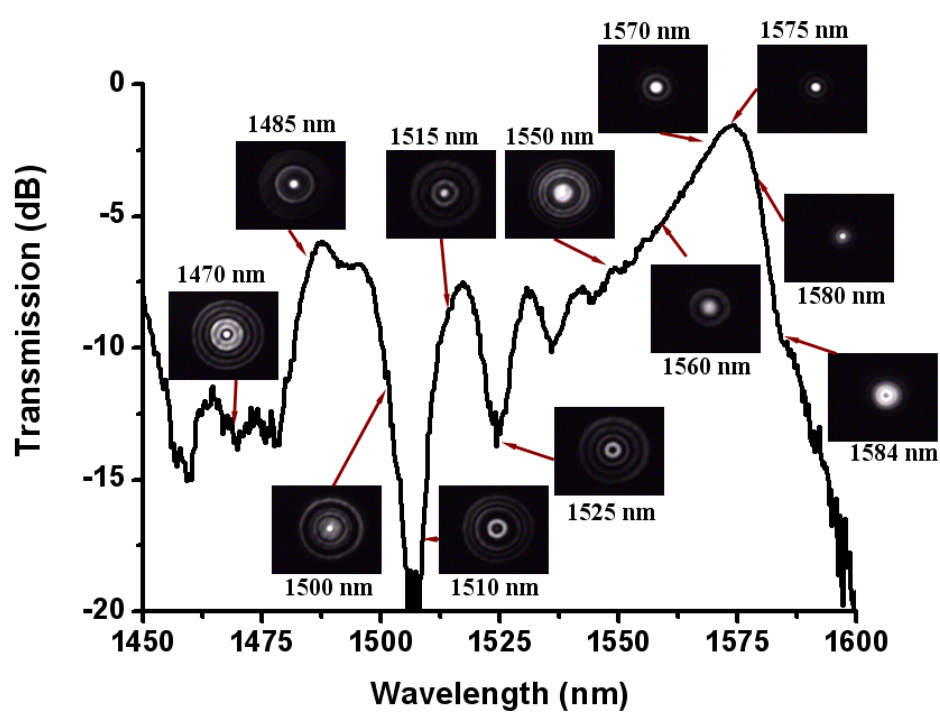


Fig. 2.31. The intensity distribution of the facet of the 105 μm MM fiber segment of a MMI structure when a tunable single-frequency signal is launched and the transmission spectrum of the corresponding MMI structure.

When a 4.3 cm long 105 μm fiber was used in the same experiment, the self-imaging wavelength was found to be 1575 nm. At other wavelengths, intensity distributions with a number of rings were observed and were more complicated than those in the 50 μm MM fiber. The transmission spectrum and some typical intensity profiles at the MM fiber facet are shown in Fig. 2.31. For the self-imaging wavelength of 1575 nm, the image of the

intensity distribution at the MM fiber facet, the corresponding three-dimensional plot, and the far-field image are shown in Fig. 2.32. Comparing the facet and the far-field intensity distributions in Figs. 2.30 and 2.32, it can be concluded that self-imaging in the 105 μm fiber is not as good as that in the 50 μm fiber.

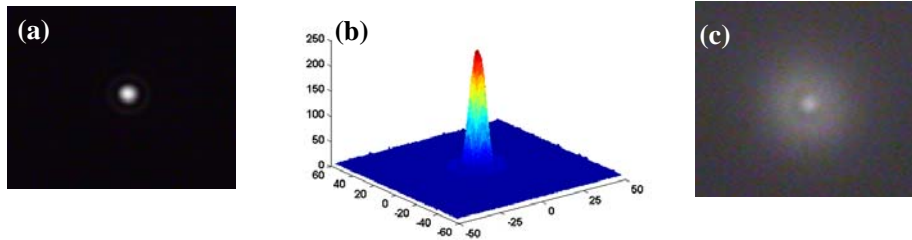


Fig. 2.32. The facet image, its three-dimensional plot, and the far-field image of the 105 μm MM fiber segment of a MMI structure when a signal of 1557 nm is input. (a) MM fiber facet image; (b) Three-dimensional plot of (a); (c) Far-field image.

2.4 Discussion and Conclusion

In this chapter, principle and properties of the self-imaging effect and the spectral filtering effect of MMI in the MM fibers have been described and investigated. Some key parameters to describe self-imaging in the MM fibers also have been evaluated.

Although Ulrich pointed out that self-imaging is an inherent property of MM waveguides, in comparison to the case of planar waveguides, MMI of optical fibers exhibit a different behavior. When the core diameter of the MM fiber segment is 25 μm , MMI in the fiber is relatively simple and an almost perfect reproduction of the input SM field from an SMF-28 fiber can be obtained because only four modes are strongly excited in the MM segment and most of energy is contained in the $LP_{0,1}$ and $LP_{0,2}$ modes. As the core diameter increases, more modes are excited and MMI becomes rather complicated. In general, perfect self-imaging of the input field from an SMF-28 SM fiber cannot be obtained in large-core MM fibers and the self-imaging quality decreases evidently as the core size larger than 250 μm . However, when the core diameter of the MM fiber is smaller than 250 μm , our calculations show that a reproduction of the input SM field with a self-imaging quality factor of 0.9 or larger is achievable.

Transmission spectrum of the MMI fiber structure and the direct observation of self-imaging at the MM fiber facet indicate that an MMI-based fiber laser or amplifier utilizing a rare-earth doped MM fiber can offer SM emission when its length has been

precisely controlled to make self-imaging occur at the splice point between an SM fiber and the rare-earth doped MM fiber.

CHAPTER 3

MMI-BASED FIBER LASERS AND AMPLIFIERS

The self-imaging effect in multimode (MM) waveguides implies that, for a single-mode (SM) field incident on the input facet of an active MM waveguide, in-phase multimode interference (MMI) results in an amplified SM field at the self-imaging plane in the MM waveguide. Applying self-imaging to obtain SM emission from an active MM planar waveguide has been proposed and demonstrated as a route to overcome the constraints of an active single-mode (SM) waveguide [29]-[34]. Although MMI in cylindrical optical fibers is more complicated than that in planar waveguides, the calculations and the experiments in Chapter 2 have shown that high quality reproduction of the input SM field can happen when a few modes are excited in the MM fiber segment. Therefore, in analogy to MMI planar waveguide lasers, an efficient MMI fiber laser or amplifier with single-mode output is feasible when the MM fiber length is precisely controlled.

In this chapter, the concept of utilizing the self-imaging effect to achieve single-transverse-mode output from a rare-earth doped MM fiber is introduced and demonstrated by use of a highly efficient diode-pumped MMI fiber laser consisting of a short Er/Yb codoped phosphate MM fiber with a core diameter of 25 μm and a conventional SM fiber (SMF-28). Subsequently, MMI-based fiber lasers and amplifiers

utilizing large-core rare-earth doped silica MM fibers are proposed and analyzed. Using an SM fiber with a large mode-field-area to improve the self-imaging quality and consequently the efficiency of an MMI large-core fiber laser is also suggested and demonstrated.

3.1 The First Demonstration of an MMI-based Fiber Laser

As have been demonstrated in Chapter 2, when an MM fiber is sandwiched by two SM fibers and the length of the MM fiber segment is precisely controlled to enable self-imaging of the input field, high transmission of the fundamental mode field of the SM fiber through the MM fiber can be obtained. A typical transmission spectrum of a 20 cm Er/Yb codoped phosphate MM fiber spliced with two SMF-28 fibers is shown in Fig. 3.1. For certain wavelengths, self-imaging of the input diffraction-limited field occurs and the propagation loss is only about 1 dB. Therefore, an MMI fiber laser cavity with low round-trip loss can be constructed by just splicing an SM fiber onto a rare-earth-doped MM fiber. Because the transmission spectrum of an MMI fiber laser cavity shifts as the length of the MM fiber changes, an efficient fiber laser with diffraction-limited emissions is achievable by just precisely controlling the length of the active MM fiber to overlap the transmission peak with the gain peak of the active ions, as illustrated in Fig. 3.1.

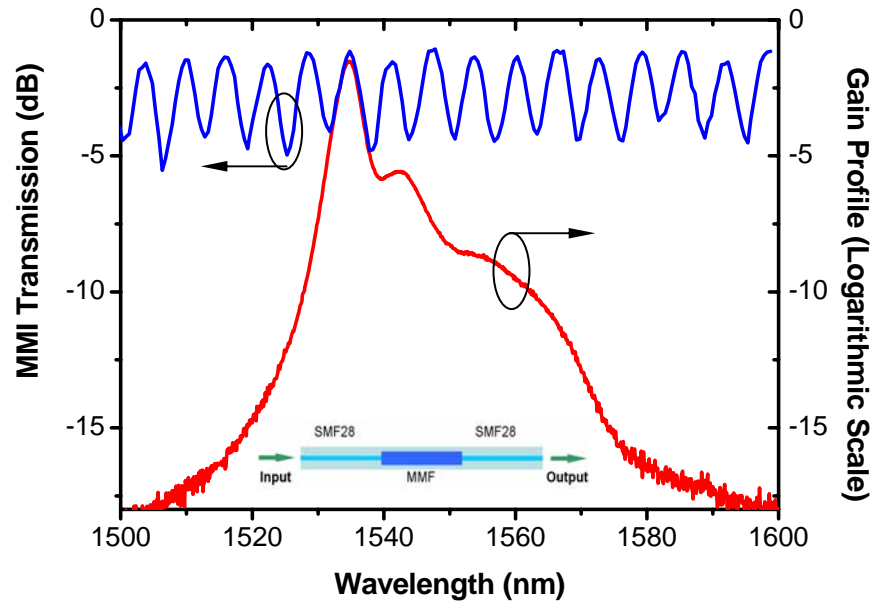


Fig. 3.1. Gain profile of a heavily Er/Yb codoped phosphate fiber and the transmission spectrum of an MMI cavity with 20-cm-long 50 μm MM fiber.

The design of our MMI fiber laser is schematically shown in Fig. 3.2. A 10.236-cm-long active MM phosphate fiber with a cladding of 125 μm is spliced to a 1-m-long section of SMF-28. The MM core is codoped with 1 wt% Er_2O_3 and 8 wt% Yb_2O_3 , respectively. The core diameter is 25 μm and the numerical aperture of the fiber is 0.17, which correspond to a normalized frequency $V \approx 8.7$. Propagation of approximately 30 modes (including two polarizations each) is supported in this MM

active fiber. The active fiber along with ~10 cm stripped SMF-28 is hold in a straight silicon U-groove which is cooled by a water chiller. The remaining 90 cm of SMF-28 are not stripped so that any cladding modes that might be excited by the modes of the MM fiber can be effectively suppressed through absorption by the outer coating and absolutely diffraction-limited output is ensured.

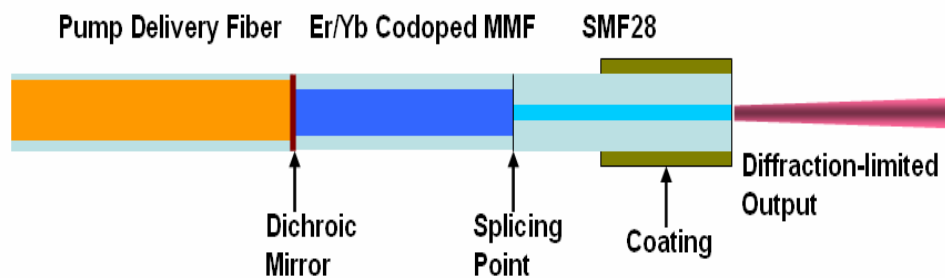


Fig. 3.2. Design of the MMI fiber laser (the figure is not to scale).

The pump source is a 976 nm beam-shaped laser diode arrays coupled by a multimode pump delivery fiber which has a 105 μm core diameter, a numerical aperture of 0.22, and a 125 μm outer diameter. A dichroic coating, which has high reflectivity at the laser wavelength and high transmission at pump wavelength, is deposited on the fiber

end-facet. The pump delivery fiber is butt-coupled to the MM active fiber. Note that the length of the MM phosphate fiber section is precisely controlled to an accuracy of better than $10\ \mu\text{m}$. For a 10-cm-long $25\ \mu\text{m}$ MM fiber, a length deviation of $10\ \mu\text{m}$ results in a transmission maximum shift of $\sim 0.1\ \text{nm}$. A transmission peak around $1535.5\ \text{nm}$ is obtained for the test hybrid cavity with a 10.236-cm-long active MM fiber that overlaps well with the maximum gain of the active fiber.

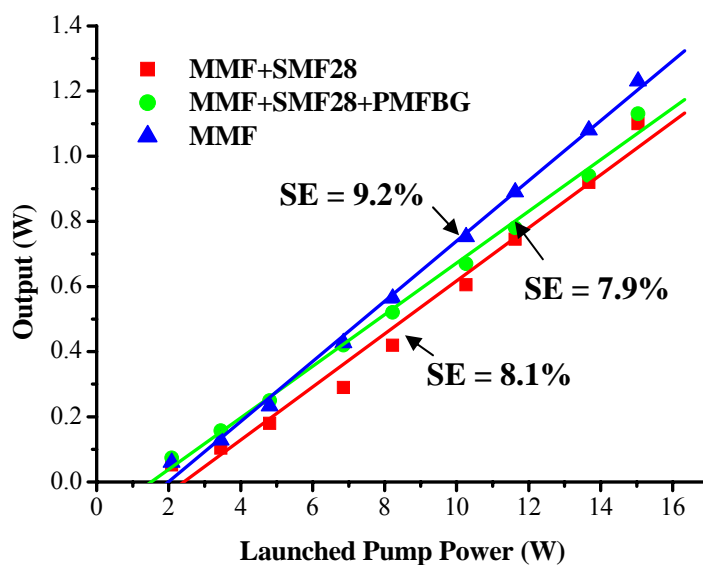


Fig. 3.3. Output power as a function of launched pump power for a MMI fiber laser as shown in Fig. 2 (red squares), a single-polarization MMI fiber laser (green circles), and a free-running MM fiber laser without SM section (blue triangles).

The output power of this MMI fiber laser as a function of launched pump power is shown in Fig. 3.3 as red squares and compared to the signal powers of a free running MM fiber laser without SMF-28 section (blue triangles) and another type of MMI fiber laser with an additional fiber Bragg grating (FBG) spliced to the SMF-28 fiber (green dots). All lasers have an active MM fiber section of ~ 10 cm. The MMI fiber laser reaches a maximum output power of more than 1 W that is limited by the available pump power. The slope efficiency is about 8.1% which is very close to 9.2%, the efficiency of its free-running counterpart MM fiber laser without a single mode section. A part of this difference might be attributed to imperfect splicing between the phosphate fiber and the silica fiber which results in some coupling losses.

The spectra of the output corresponding to different pump levels are plotted in Fig. 3.4. In contrast to the multi-wavelength operation due to MMI effects in passive MM fiber which has been reported in [35], we observe only a single emission peak with a 3-dB bandwidth clearly below 0.5 nm. Small bandwidth, single-peak emission of this MMI fiber laser indicates the spectral filtering effect of MMI during in-phase operation, and the implications of the particular gain profile of heavily Er/Yb codoped phosphate fiber as shown in Fig. 3.1. It is also observed that the emission peak moves towards shorter wavelengths and the bandwidth slightly broadens with increasing pump power.

The blue-shift of the laser peak should result from the increased MM fiber length due to thermal expansion at high pump levels. Some spectral broadening may be caused by a larger number of oscillating longitudinal laser modes.

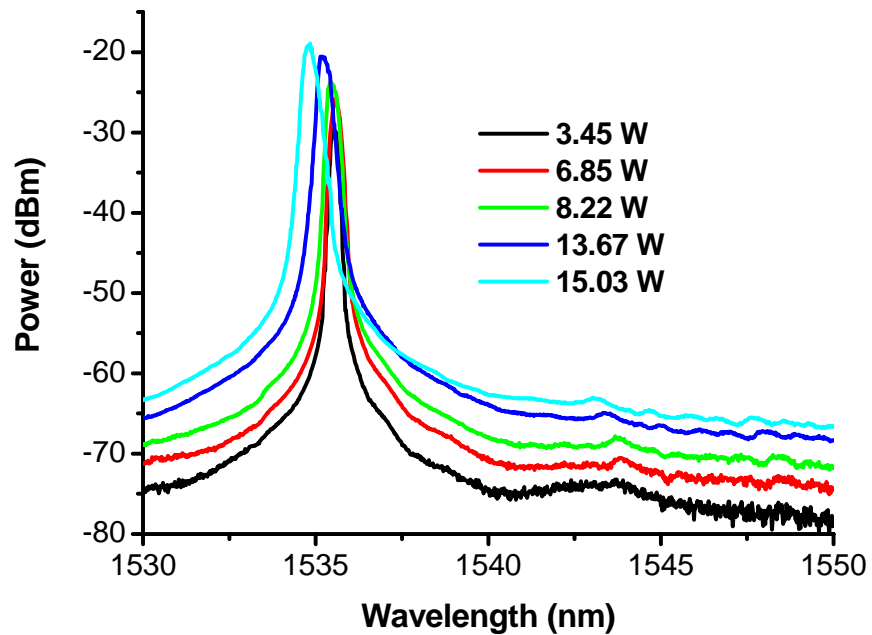


Fig. 3.4. Emission spectra of an MMI fiber laser at various pump power levels.

Furthermore, utilizing the spectral filtering effect of MMI, single-polarization SM emission can be obtained from an active MM fiber combined only with a polarization-maintaining fiber Bragg grating (PMFBG) without any other polarizing element. Note that, in general, to obtain single-polarization output from an all-fiber laser, a single-polarization SM fiber that only guides a single polarization state of the fundamental mode must be used.

A PMFBG is fabricated by writing the FBG onto a highly birefringent SM fiber. The transmission spectrum of a PMFBG, shown by a dotted green line in Fig. 3.5, always has two minima (two reflection peaks) which correspond to the two orthogonal linear polarization states. As a consequence, when the PMFBG is spliced with a conventional active SM fiber, a spectrum with two narrow-linewidth peaks is usually obtained and the output is randomly polarized. However, it is found that, when the PMFBG was spliced to the output SMF-28 fiber in the MMI laser scheme of Fig. 3.2, a linearly polarized output with a 3-dB linewidth less than 0.1 nm was obtained. The linearly polarized output was verified by measuring the signal power through a rotating a Glan-Taylor polarizer and a polarization extinction ratio of about 21 dB has been measured along the two orthogonal directions. The emission spectrum of the single-polarization-state operation is shown as a solid red line in Fig. 3.5. The emission peak is exactly correlated to one of the reflection peak of the PMFBG.

The observed single-polarization-state operation is a direct consequence of the MMI filtering effect. The transmission spectrum of the MMI structure corresponding to the MMI fiber laser is shown by a dashed black line in Fig. 3.5. The overlap of the transmission peak of the MMI structure with the longer wavelength reflection peak of the PMFBG prevents the oscillation at the other shorter wavelength reflection peak and leads to single-polarization-state operation. Interestingly, when the pump delivery fiber is displaced a few tens of microns away from the in-contact butt-coupling position, an output spectrum with two peaks separated by about 0.4 nm was observed and is shown by a short dashed line in Fig. 3.5. Consequently, the output became randomly polarized. This phenomenon is caused by a shift of the MMI transmission peak into the center between the two reflection peaks of the PMFBG due to the longer MMI cavity. In this situation both polarization states were able to reach the lasing threshold and oscillate in the MMI laser cavity. Single-polarization-state operation at the shorter reflection peak of the PMFBG can also be obtained by moving the pump delivery fiber even further away. However, the output power becomes much lower because of the poor coupling of the pump light.

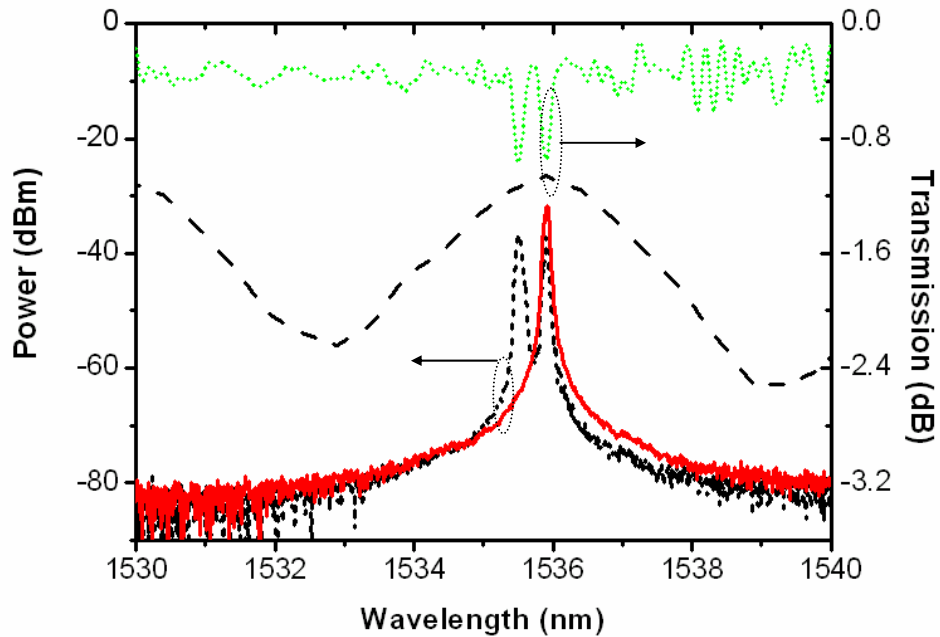


Fig. 3.5. Transmission spectra of a PMFBG (dotted green line) and a MMI structure consists of a 20 cm long 25 μm Er-Yb codoped MM phosphate fiber and two SMF-28 fibers (dashed line), respectively, and the output spectrum of a MMI fiber laser operating at single-polarization-state (solid red line) and random polarization-state (short dashed line), respectively.

When the MM fiber length was accurately controlled, single-polarization-state was maintained even at the maximum pump level. The linearly polarized signal power as a function of pump power is shown in Fig. 3.3. The 7.9% slope efficiency of the MMI fiber laser in single-polarization operation (circle) is only slightly less than that of its randomly-polarized MMI fiber laser counterpart (square) and the MM fiber laser counterpart (triangle). The single-polarization-state operation of this MMI fiber laser may

be more difficult to maintain as the pump power becomes much higher. However, when a larger-core or a longer active MM fiber laser is used, single-polarization-state operation with much higher output is still possible since the filtering bandwidth of the corresponding MMI structure becomes narrower and the filtering isolation becomes much larger.

It is worth noting here that, in all previous schemes of mode discrimination in fiber lasers with MM sections [11-20], only the fundamental mode of the MM section is oscillating in the fiber laser cavity. In our MMI fiber laser, however, several transverse modes are oscillating in the MM fiber section and they constructively interfere at the splice point between SM and MM fiber section where they are transformed into the fundamental mode of the SM fiber. Therefore, the active mode volume of our MMI fiber laser is increased significantly compared to any fundamental mode selection technique. Furthermore, MMI fiber lasers are easy to construct and do not need any specially-designed fibers. Especially, because of the intrinsic properties of MMI, narrow linewidth and linearly polarized output can be obtained from MMI fibers without using any spectral filter and polarizing component. Most importantly, the beam quality of the output of MMI fibers and amplifiers is only determined by the guiding property of the output SM fiber. The beam quality (M^2) of the first MMI fiber laser was measured to 1.01.

3.2 High Power MMI-based Fiber Lasers and Amplifiers

Although the first MMI fiber laser provided a perfect beam quality ($M^2 = 1.01$), an efficiency close to that of the MM fiber laser counterpart, and a narrow emission linewidth. However, the output of this MMI fiber laser was limited to watt-level by the large background loss of rare-earth doped phosphate fiber and the available pump power. Further power scaling may also be hampered by the small active core diameter (25 μm) and the low transition temperature ($\sim 600^\circ\text{C}$) of phosphate glass. Therefore, high power MMI fiber lasers and amplifiers can be built with active large-core ($> 50 \mu\text{m}$) MM silica fibers because their background loss is much lower than that of phosphate fibers and silica glass has a much higher transition temperature ($> 1600^\circ\text{C}$) than phosphate glass.

It is also noted that, in the first demonstration of the MMI-based fiber laser, a piece of 10 cm long active MM phosphate fiber with a core diameter of 25 μm was selected under a consideration of alleviating the mode conversion inside the MM fiber segment. When the length and the core diameter of the MM fiber segment are small, the effect of random mode conversion induced by internal perturbations, such as core inhomogeneities, geometrical imperfection, and microbending, is negligible. As the core diameter and the length of the MM fiber segment increase, the effect of random mode conversion becomes significant. Therefore, random mode conversion in large-core MM

fibers is investigated first in this section. Then the features of high power MMI-based fiber lasers and amplifiers, such as slope efficiency, output spectrum, and beam quality, are investigated through simulation and experiments. Finally, the method of improving the self-imaging quality and reducing the loss of random mode conversion for large-core MM fibers by use of an SM fiber with a large mode-area is demonstrated.

3.2.1 Loss of random mode conversion

Ideally, each of the excited $LP_{0,n}$ modes propagates independently along the MM fiber and the self-imaging quality mostly determines the round-trip loss of an MMI fiber cavity. However, due to internal perturbations, such as core inhomogeneities, geometrical imperfection, and microbending, the energy contained at the excited $LP_{0,n}$ modes inevitably converted to other modes as a consequence of mode coupling. To measure the loss due to the random mode conversion in large-core MM fibers, the transmission at a self-imaging wavelength for different MM fiber lengths is obtained from the cutback experiment described in section 2.3.2 and is plotted in Figs. 3.6 and 3.7 for the 50 μm and 105 μm fibers, respectively. Because the background loss of the passive MM fiber used in the experiments is very small ($< 0.01\text{dB/m}$ in the wavelength range of 1.5-1.6 μm), the loss caused by the random mode conversion in the MM fiber can be estimated from the

slope of a linear fitting of the data shown in Figs. 3.6 and 3.7. The loss due to the mode conversion in the 50 μm fiber is about 1.28 dB/m and about 1.67 dB/m in the 105 μm fiber.

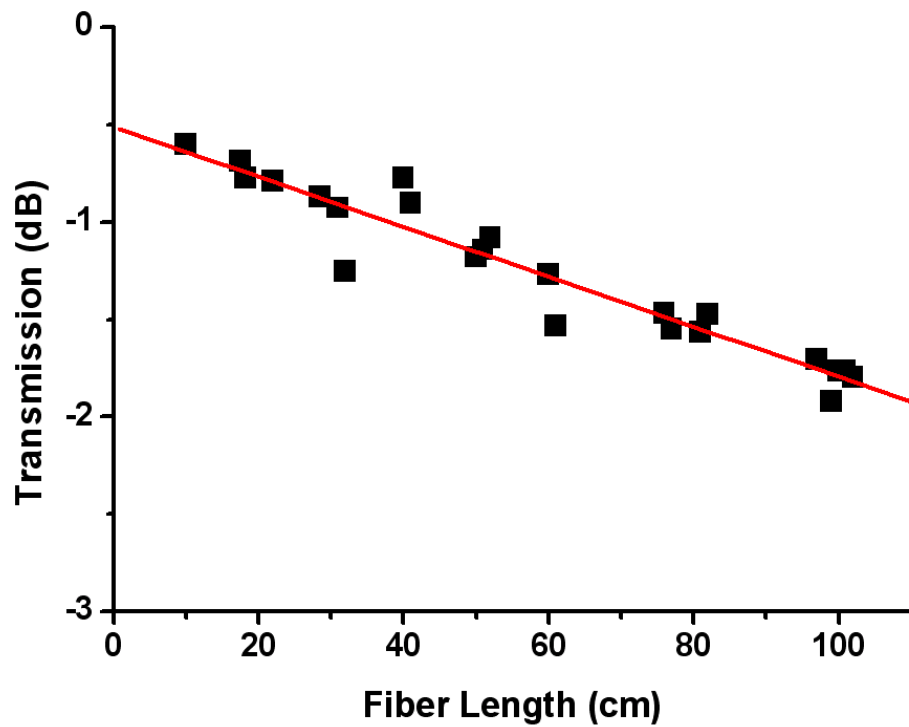


Fig. 3.6. Transmission at the self-imaging wavelength for MMI structures consisting of 50 μm MM fibers with different lengths and an SMF-28.

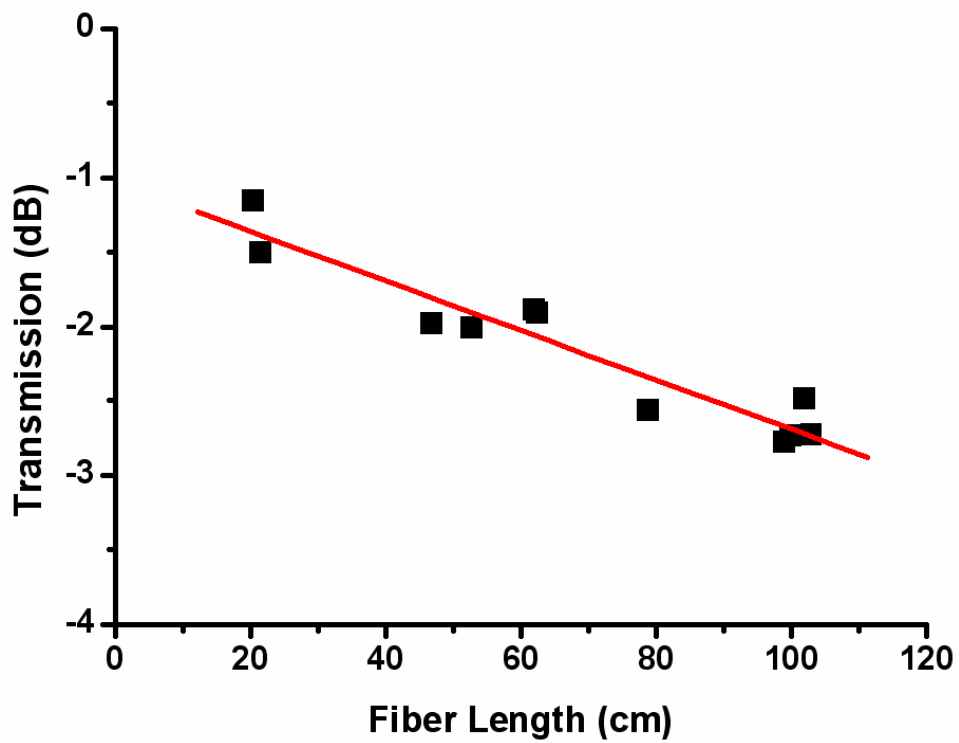


Fig. 3.7. Transmission at the self-imaging wavelength for MMI structures consisting of 105 μm MM fibers with different lengths and an SMF-28.

3.2.2 Efficiency of high power MMI fiber lasers

Since the MM fiber of the first MMI fiber laser has a small core and a short length, the fiber cavity loss due to imperfect self-imaging and random mode conversion is negligible.

Consequently, the efficiency of the MMI fiber laser is very close to that of the corresponding MM fiber laser because. As the core diameter or the length of the MM fiber increases, the cavity loss will increase evidently due to the worse self-imaging quality shown in Chapter 2 and the random mode conversion shown in section 3.2.1. To understand how these two factors affect the operation of an MMI fiber laser, the power distribution inside the fiber cavity and the slope efficiency of an MMI fiber laser and its MM fiber laser counterpart can be investigated through simulations by combining a Rigrod analysis and a Digonnet model [36]. Although the cavity configuration and the oscillating modes inside the MM fiber segment are not identical for the MMI fiber laser and the MM fiber laser, we assume that this does not change the lasing dynamics and our simulation based on effective absorption coefficients, cross sections, and excitation lifetimes is applicable to compare slope efficiencies between the MMI and MM fiber lasers.

In order to obtain high power from an MMI fiber laser, the parameters of a low-loss MM silica fiber codoped with Er and Yb ions are used in our calculations. According to the setup of an MMI fiber laser shown in Fig. 3.2, the reflectivities of the cavity mirrors are $R_1 = 99\%$ and $R_2 = 4\%$ for the dielectric mirror and the cleaved SM fiber end facet, respectively. Using a Rigrod analysis and a Digonnet model, the governing equations for forward power $P^+(z)$ and backward power $P^-(z)$ in the cavity can be expressed as follows:

$$\frac{dP^+(z)}{dz} = \frac{\sigma_s \tau_f}{h\nu_p} \alpha_a P_p(z) \frac{F_p}{A_f} \cdot \frac{P_0 + P^+(z)}{1 + (P^+(z) + P^-(z))/P_s} - (\alpha_L + \alpha_{mc})P^+(z) \quad (1)$$

$$\frac{dP^-(z)}{dz} = -\frac{\sigma_s \tau_f}{h\nu_p} \alpha_a P_p(z) \frac{F_p}{A_f} \cdot \frac{P_0 + P^-(z)}{1 + (P^+(z) + P^-(z))/P_s} + (\alpha_L + \alpha_{mc})P^-(z) \quad (2)$$

In the above equations, z represents the position in the fiber cavity. The pump power propagates according to $P_p(z) = P_p(0)\exp[-(\alpha_a + \alpha_p)z]$ after $P_p(0)$ is the launched into the MM fiber section. Here, α_a is the effective absorption coefficient and α_p is the background loss of the fiber at the pump wavelength of 975 nm. α_L is the background loss at the laser wavelength of 1535 nm and α_{mc} is the loss due to the random mode conversion. A_f is the cross-sectional area of the fiber core, σ_s the stimulated cross-section, τ_f the excitation lifetime of the upper laser level, $h\nu_p$ the pump photon energy, $h\nu_L$ the laser photon energy, F_p the spatial overlap integral between pump and signal modes, $P_s = (h\nu_L/\sigma_s\tau_f)A_f$ the saturation output power, and $P_0 = N h\nu_L(\pi\Delta\nu_L/2)$ the spontaneous emissions associated with N photons in the gain bandwidth $\Delta\nu_L$.

The 4th Runge-Kutta method was used to do iterative calculations to solve the coupled differential equations for forward and backward powers in a cavity of length L_f . By using the boundary conditions $P^+(0) = R_1P^-(0)$ and $P^-(L_f) = R_2P^+(L_f)$ the decision condition for the boundary values in our simulations are given by

$$P^+(L_f) = \frac{-P_0(1+R_2) + \sqrt{P_0^2(1+R_2)^2 + 4R_2P^-(0)(P_0 + R_1P^-(0) + P_0R_1)}}{2R_2} . \quad (3)$$

In addition, self-imaging quality at the splicing point z_{sp} is assumed leading to $P_{SM}^+(z_{sp}) = \eta P_{MM}^+(z_{sp})$ and $P_{MM}^-(z_{sp}) = P_{SM}^-(z_{sp})$. P_{SM} is the power inside the SM fiber, P_{MM} is the power inside the active MM fiber, and η is the power coupling efficiency from the MM fiber to the SM fiber.

The values of the parameters used in our simulations were set as $\alpha_p = 6.5 \times 10^{-2} \text{ m}^{-1}$; $\alpha_L = 3.2 \times 10^{-2} \text{ m}^{-1}$; $\sigma_s = 5.7 \times 10^{-25} \text{ m}^{-3}$; $\tau_f = 11 \text{ ms}$; and $F_p = 0.95$ for the MM fiber. The effective absorption coefficient α_a has been calculated from the core absorption divided by the ratio between the area of the pump cladding and the area of the core. Although a core absorption of 1000 dB/m can be achieved in an Er-Yb codoped silica fiber and such a fiber laser has resulted in a slope efficiency of 41% [38], in our calculation the core absorption coefficient is set to be 300 dB/m since it is large enough for a MMI fiber laser. This absorption can be adjusted and optimized varying the Yb doping level in the active fiber core.

It is assumed that a commercial 105- μm -core fiber-coupled laser diode with an output power of 75 W is employed as the pump source. When a 50 μm MM fiber is used in the MMI structure, the loss due to mode conversion was measured to be 1.28 dB/m and η was -0.5 dB. In Fig. 3.8, the forward power and the backward power inside the MMI fiber laser that consists of a 50 cm long active MM fiber and a 10 cm long SMF-28 fiber

are plotted. For comparison, the forward power and the backward power inside the 50 cm long MM fiber laser without the SMF-28 section are also plotted. Obviously, the powers inside the MM fiber segment of the MMI fiber laser are smaller than those of the MM fiber laser due to the loss of random mode conversion and the output power of the MMI fiber laser is further reduced due to the imperfect self-imaging.

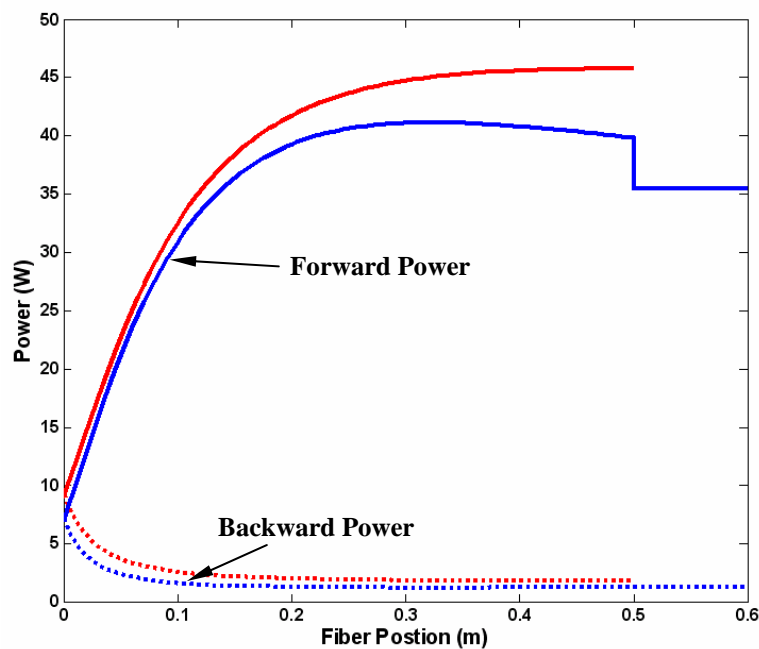


Fig. 3.8. Forward powers (solid lines) and backward powers (dotted lines) inside a MMI fiber laser that consists of a 50 cm long 50 μm active MM fiber and a 10 cm long SMF-28 fiber (blue) and inside its corresponding 50 cm long MM fiber laser (red).

When a 105 μm MM fiber is used in the MMI structure, the loss due to mode conversion was measured to be 1.67 dB/m and η was -1 dB. In Fig. 3.9, the forward power and the backward power inside the MMI fiber laser that consists of a 50 cm long MM active fiber and a 10 cm long SMF-28 fiber and inside the corresponding 50 cm long MM fiber laser are plotted, respectively. Due to mode conversion and imperfect self-imaging, the output power from the MMI fiber laser is only 65% of that of the corresponding MM fiber laser.

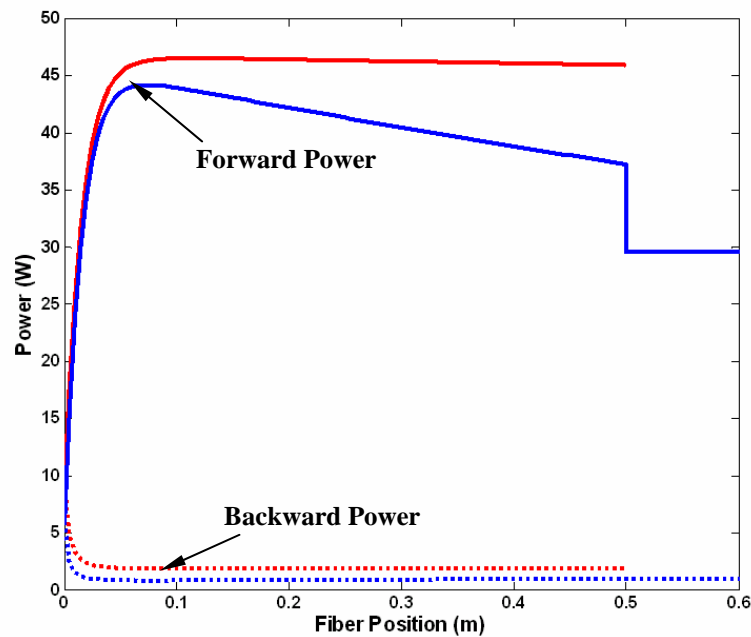


Fig. 3.9. Forward powers (solid lines) and backward powers (dotted lines) inside a MMI fiber laser that consists of a 50 cm long 105 μm active MM fiber and a 10 cm long SMF-28 fiber (blue) and inside its corresponding 50 cm long MM fiber laser (red).

In Fig. 3.9, it is clear that the pump is almost absorbed within the first 10 cm active fiber because of the effective core pumping scheme. Therefore, the length of the 105 μm active MM fiber segment can be as short as 10 cm. For this case, the forward powers and the backward powers inside the MMI fiber laser and the corresponding 10 cm long MM fiber laser are plotted in Fig. 3.10. Note that the output power of the 105 μm MMI fiber laser reaches 75% of that of the corresponding MM fiber laser.

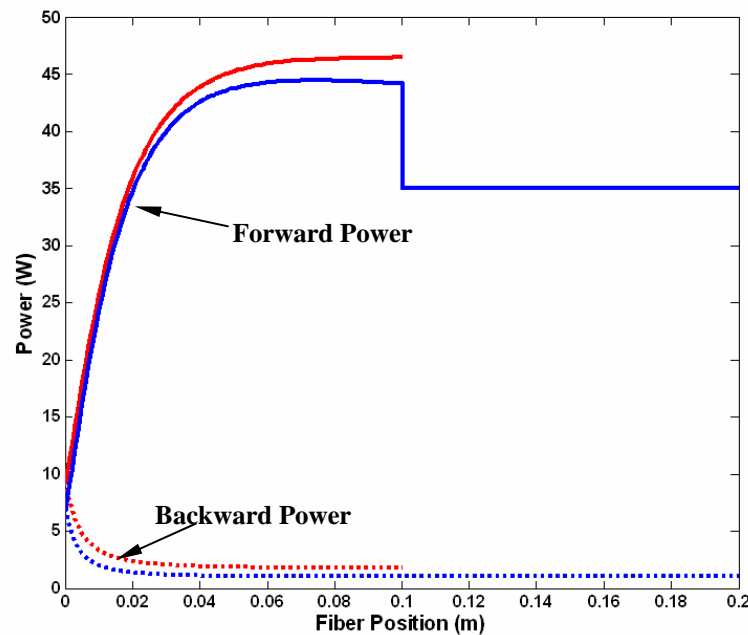


Fig. 3.10. Forward powers (solid lines) and backward powers (dotted lines) inside a MMI fiber laser that consists of a 10 cm long 105 μm active MM fiber and a 10 cm long SMF-28 fiber (blue) and inside its corresponding 10 cm long MM fiber laser (red).

When the active MM fiber segment is 50 cm long, the output power with respect to the pump power for the MMI fiber lasers and their corresponding MM fiber lasers are plotted in Fig. 3.11. Because of the loss due to mode conversion and imperfect self-imaging, the slope efficiencies of the 50 μm and the 105 μm MMI fiber laser are 77% and 65% of those of their corresponding MM fiber lasers, respectively. When the active 105 μm MM fiber segment is 10 cm long, the output power with respect to the pump power for the MMI fiber lasers and their corresponding MM fiber lasers are plotted in Fig. 3.12. The slope efficiencies of the 105 μm MMI fiber laser are 75% of that of the corresponding MM fiber lasers.

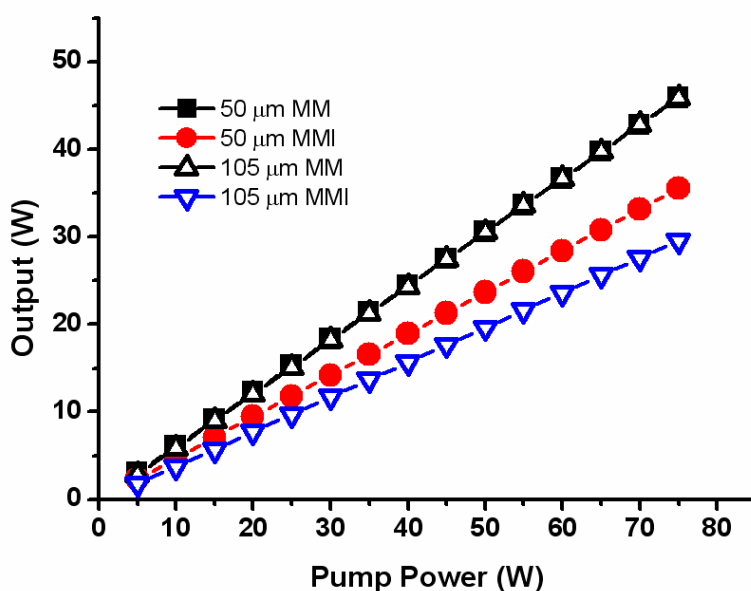


Fig. 3.11. Output power with respect to the pump power for a MMI fiber laser that consists of a 50 cm long 50 μm (circle) or 105 μm active MM fiber (downward triangle) and a 10 cm long SMF-28 fiber and their corresponding 50 cm long MM fiber lasers (square and upward triangle, respectively).

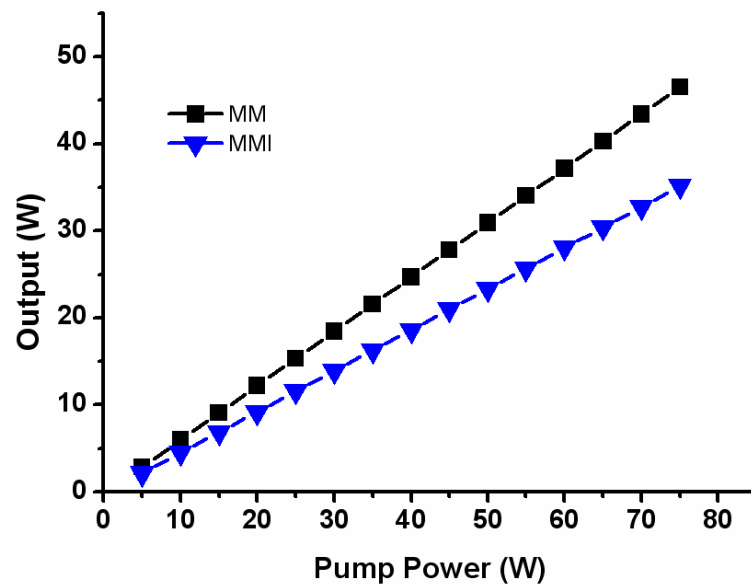


Fig. 3.12. Output power with respect to the pump power for a MMI fiber laser that consists of a 10 cm long 105 μm active MM fiber and a 10 cm long SMF-28 fiber (triangle) and the corresponding 10 cm long MM fiber laser (square).

3.2.3 Spectrum of MMI fiber lasers

Due to the filtering effect of MMI, the output spectrum of an MMI fiber laser always exhibits a unique feature – the MMI fiber laser only oscillates at wavelengths that satisfy the self-imaging condition. Therefore, the output spectrum of an MMI fiber can be tuned by changing the length of the MM fiber segment. In the first 10 cm MMI fiber laser, a

spectrum with only one peak was observed as shown in Fig. 3.4. When an active MM fiber section with a length of 15 cm was used in the same MMI laser setup, a spectrum with two peaks (blue line) was observed as shown in Fig. 3.13. In comparison, one spectrum (red line) from Fig. 3.4 and a typical spectrum of an MM fiber laser (black line) are also plotted in Fig. 3.13. Since there is no self-imaging around 1543 nm, there is no oscillation of the 10 cm MMI laser at this wavelength. Because the self-imaging wavelength shifts with the length of the MM fiber segment, the output spectrum from an MMI fiber laser can be tailored through the length of the MM fiber section.

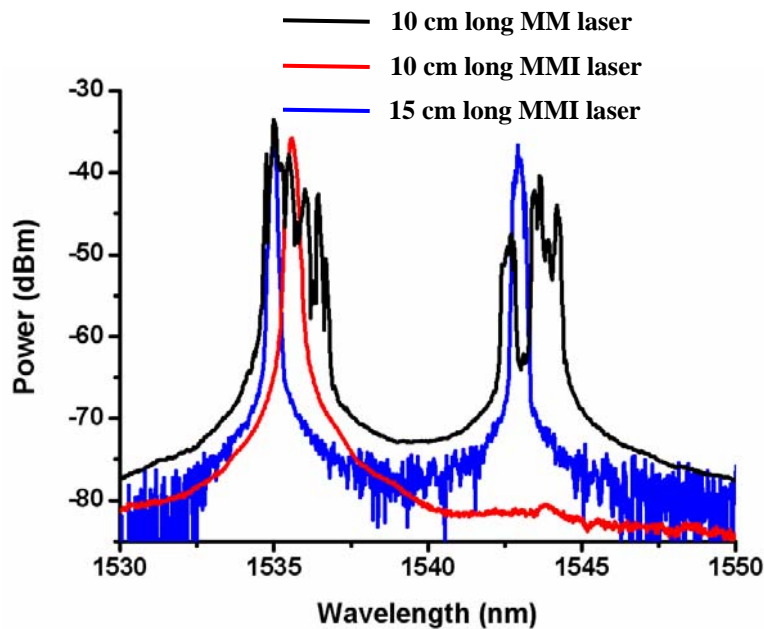


Fig. 3.13. Spectrum of an MMI fiber laser that utilizes a 10 cm long 25 μm Er-Yb codoped phosphate fiber (red line), that of an MMI fiber laser that utilizes a 15 cm long 25 μm Er-Yb codoped phosphate fiber (blue line), and that of the corresponding MM fiber laser (black line).

3.2.4 Beam quality of MMI fiber lasers and amplifiers

When a standard SM fiber is used as the output fiber as shown in Fig. 3.2, the output beam is strictly diffraction-limited and the beam quality (M^2) is equal to that of the SM fiber and can reach 1. In contrast to other methods of obtaining SM emission from MM active fiber, MMI fiber lasers not only offer a perfect beam quality, but also provide a flexible connectivity by using a standard SM fiber as the output delivery fiber.

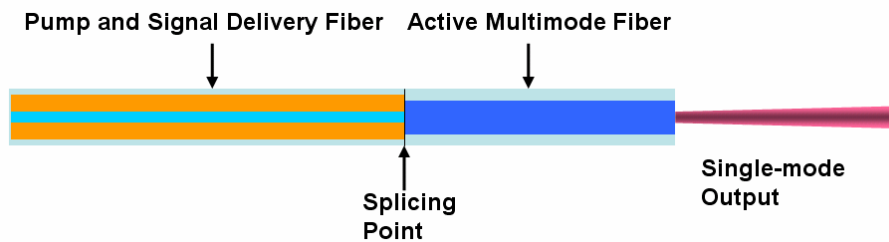


Fig. 3.14. Depiction of a proposed high-power MMI fiber amplifier in which the MM fiber is employed as the output fiber.

On the other hand, an MMI fiber amplifier can also operate in a configuration as shown in Fig. 3.14 in which the MM active fiber itself serves as the output fiber. In this case, the output power will be very close to that of the corresponding MM fiber laser. But

the beam quality may be ruined due to imperfect self-imaging and random mode conversion. In order to investigate the beam quality of the output in this situation, a tunable semiconductor was employed as the input signal and a passive MM fiber was used to replace the active MM fiber. As shown in Fig. 3.15 (a), the beam quality of the output at the self-imaging wavelength reached about 1.1 when a 50 μm MM fiber was used. When a 105 μm MM fiber was used, the beam quality of the output at the self-imaging wavelength was slightly worse, but still reaching about 1.3. It is noted that the M^2 measurement is truly meaningful only when the signal is at the self-imaging wavelength where a near-Gaussian beams are generated. At other wavelengths, the output beam from the MM fiber exhibits a complicated profile with special propagation properties that will be discussed in Chapter 4.

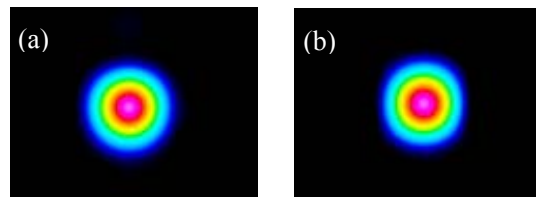


Fig. 3.15. Beam profiles of proposed high-power MMI fiber amplifiers depicted in Fig. 3.14. (a) M^2 was about 1.1 when a 50 μm MM fiber was used; (b) M^2 was about 1.3 when a 105 μm MM fiber was used.

3.2.5 Improve the efficiencies of large-core MMI fiber lasers and amplifiers

As analyzed above, the efficiencies of MMI fiber lasers and amplifiers are mainly restricted by the self-imaging quality and the loss of random mode conversion. The calculations in section 3.2.2 show that the slope efficiency of the 105 μm MMI fiber laser is about 75% of that of the corresponding MM fiber laser. As the core size becomes larger, the efficiency will be much lower due to the worse self-imaging and the stronger random mode conversion.

However, it is found that both the self-imaging quality and the loss of random mode conversion of large-core MM fibers can be improved by replacing the SMF-28 with a passive SM fiber with a large mode-field-area (MFD). Our calculations indicate that fewer guided modes are excited inside the MM fiber segment as the MFD of the input SM fiber increases and, as a consequence, the self-imaging quality is increased correspondingly. When the MFD of the input SM fiber is 23 μm and 40 μm , the number of the excited modes in the 105 μm MM fiber segment reduces to 7 and 5, respectively, as compared to 14 excited modes for a SMF-28. In the two cases, the self-imaging quality factor γ along the 105 μm MM fiber is plotted in Figs. 3.16 and 3.17, respectively. Comparing to the self-imaging quality in Fig. 2.10, not only is the self-imaging quality improved, but also the tolerance on the fiber length is relaxed. The relaxed tolerance

regarding the length of the MM segment can also be attributed to fewer excited modes in the MM fiber segment. When the MFD of the input SM fiber is $40\ \mu\text{m}$, a tolerance of 1 mm is enough to obtain a self-imaging quality higher than 0.9, as compared to a tolerance of $100\ \mu\text{m}$ when the SM fiber is an SMF-28..

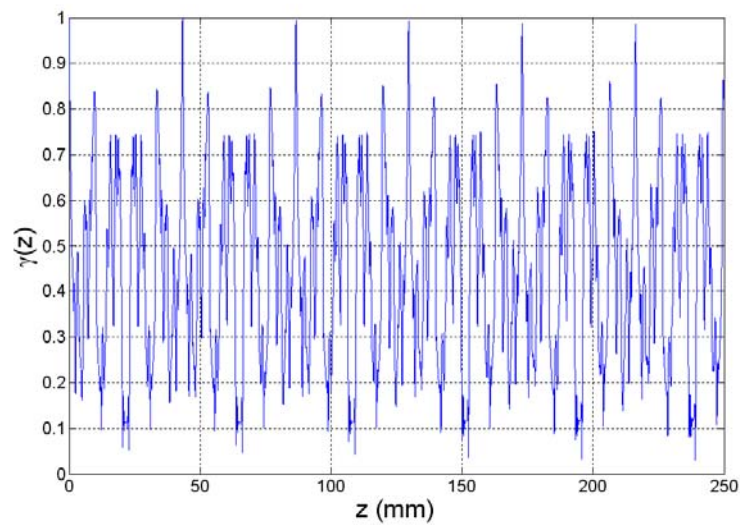


Fig. 3.16. Self-imaging quality factor γ along a MM fiber segment with a core diameter of $105\ \mu\text{m}$ when the input SM fiber has an MFD of $23\ \mu\text{m}$.

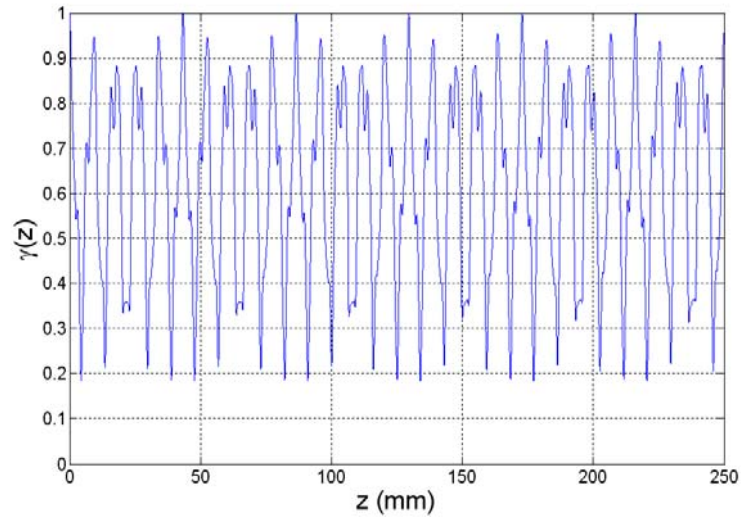


Fig. 3.17. Self-imaging quality factor γ along a MM fiber segment with a core diameter of $105\ \mu\text{m}$ when the input SM fiber has an MFD of $40\ \mu\text{m}$.

To evaluate the improvement of self-imaging via an SM fiber with a large MFD, a passive SM fiber (LMFD-10) with a core diameter of $10\ \mu\text{m}$ and a NA of 0.07 (i.e., about $23\ \mu\text{m}$ of the MFD) was used to replace the SMF-28 in Fig. 2.24. The result of a cutback experiment for an MMI fiber structure consisting of the LMFD-10 SM fiber and the $105\ \mu\text{m}$ MM fiber is shown in Fig. 3.18. In comparison, the result of the MMI fiber structure consisting of the SMF-28 fiber and the $105\ \mu\text{m}$ MM fiber is also shown in Fig. 3.18. Obviously, the use of LMFD-10 not only improves the transmission at the self-imaging

wavelength significantly (i.e., improvement of the self-imaging quality), but reduces the loss of the mode conversion as well. Comparing to 1.67 dB/m with the SMF-28 fiber, the loss due to the random mode conversion with the LMFD-10 fiber was only 0.5 dB/m.

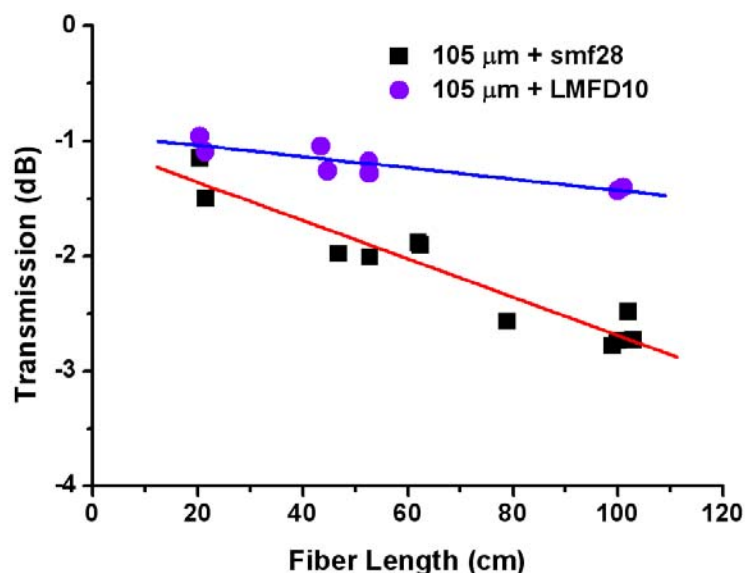


Fig. 3.18. Transmission at the self-imaging wavelength for MMI structures consisting of 105 μm MM fibers with different lengths and a LMFD-10 fiber (circle) or an SMF-28 fiber (square).

In order to see the improvement of the efficiency of an MMI fiber laser utilizing the LMFD-10 fiber, the output power with respect to the pump power for a 10 cm long 105 μm MM fiber laser, an MMI fiber laser consisting of the 10 cm long 105 μm MM fiber and a 10 cm long SMF-28 fiber, and an MMI fiber laser consisting of a 10 cm long 105

μm MM fiber and a 10 cm long LMFD-10 fiber are plotted in Fig. 3.19, respectively. When the SMF-28 fiber is used, the slope efficiency is 76% of the corresponding MM fiber laser. When the LMFD-10 fiber is used, the slope efficiency is increased to 87% of the corresponding MM fiber laser. The efficiency of the MMI fiber laser is expected to be much closer to that of its corresponding MM fiber laser if the random mode conversion and the self-imaging quality are further improved.

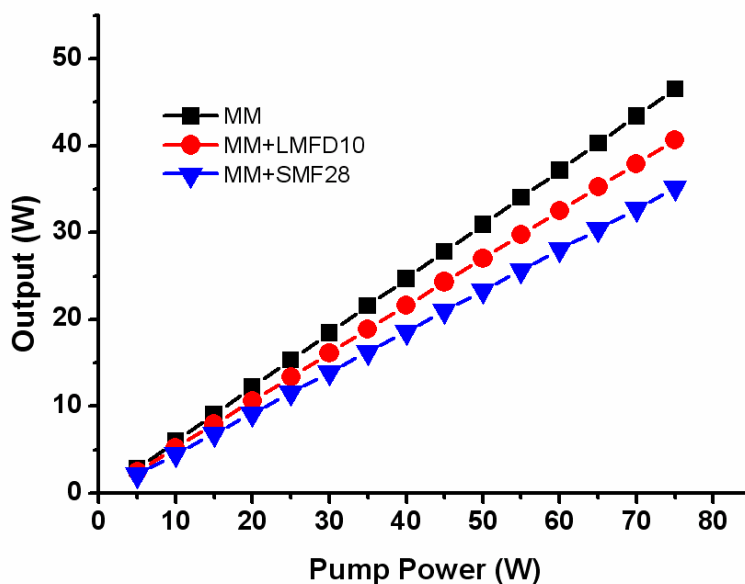


Fig. 3.19. Output power with respect to the pump power for a MMI fiber laser that consists of a 10 cm long $105\ \mu\text{m}$ active MM fiber and a 10 cm long SMF-28 fiber (triangle), or a 10 cm long LMFD-10 fiber (circle), and the corresponding 10 cm long MM fiber laser (square).

3.3 Discussion and Conclusion

Although MMI in MM fibers is more complicated than that in planar waveguides, quasi-reproduction of the input SM field with a high self-imaging quality can still be achieved. In analog to the MMI-based planar waveguide lasers, the approach to achieve single-transverse-mode output from an active MM fiber by utilizing the self-imaging principle of MMI effects has been demonstrated. Efficient and stable emission of the fundamental mode with narrow bandwidth from the MMI fiber laser has been achieved.

In general, perfect self-imaging of the input field from an SMF-28 fiber cannot be obtained in large-core MM fibers. Our calculations show that a reproduction of the input SM field with a self-imaging quality factor of 0.9 or larger is achievable when the core diameter of the MM fiber is smaller than 250 μm . It implies that a MMI-based large-core fiber laser or amplifier with trip-loss smaller than 1 dB can be constructed. Although additional loss caused by random mode conversion becomes significant as the large-core MM fiber length is long, our experiments in section 3.2.1 indicate that, a trip-loss < 2 dB/m can be obtained in the 50 μm fiber and < 3 dB/m can be obtained in the 105 μm fiber, respectively. Both values are much smaller than the background loss of rare-earth doped phosphate fibers. Therefore, rare-earth doped silica MMI fiber lasers and

amplifiers will be more efficient than the first MMI fiber laser utilizing highly Er/Yb codoped phosphate fiber.

Our calculations and experiments also show that the self-imaging quality and the mode conversion in very-large-core MM fibers ($> 100 \mu\text{m}$) can be improved via SM fibers with large MFD. Technically, it is easier to fabricate a passive SM fiber with large MFD than the active counterpart. Moreover, the SM fiber segment in an MMI fiber laser or amplifier can be very short, therefore it might not be necessary to consider the bending loss that typically sets a limit for the core size of an active SM fiber. Therefore, using SM fibers with large MFD is a feasible route to improve the performance of very-large-core MMI fiber lasers and amplifiers.

It should be pointed out that the MM fiber segment of an MMI fiber laser or amplifier must be kept straight to avoid the additional loss of mode conversion caused by macro-bending, so the fiber cavity should be always shorter than 1 meter in practice. We notice that, in recent years, rod-type fiber lasers [10, 38] can generate hundreds watts output from short-length active fibers (tens of centimeters). Therefore, high power MMI fiber lasers or amplifiers are of much practicability.

In conclusion, MMI fiber lasers and amplifiers possess unique features that make them excellent candidates for compact and miniature solid-state lasers. Tens or even hundreds of watts true single-mode emission can be generated from only a few tens of

centimeters long MMI fiber lasers and amplifiers. Due to the short fiber cavity, MMI fiber lasers and amplifiers are well-suitable for Q-switched or narrow-linewidth signal generation or amplification, because in these cases stimulate Raman scattering and stimulated Brillouin scattering limit the performance of fiber devices with a long fiber cavity.

CHAPTER 4

NONDIFFRACTING BEAM GENERATION

Diffraction is a well-known optical phenomenon associated with changes of the amplitude and/or phase of the light as it encounters an obstacle. Diffraction pattern is created as a consequence of the interference of parts of the wavefront that propagate beyond the obstacle. Diffraction affects the propagation of Gaussian light beam in free-space and causes its intensity profile to spread out. The diffractive spreading becomes increasingly noticeable at distances beyond the Rayleigh range defined by

$$Z_R = \frac{\pi w_0^2}{\lambda}, \quad (4.1)$$

where w_0 is the beam waist size and λ is the light wavelength. Diffraction sets a limit that makes it impossible to simultaneously obtain a beam with very narrow waist and a long nondiffracting propagation distance (longer than the Rayleigh range). Durnin showed the possibility of diffraction-free beams with special field distributions, so-called Bessel beams [39], whose central spot can be extremely narrow, on the order of one wavelength, without being subject to diffractive spreading. It is found that the beams coming from MMI fiber structures exhibit nondiffracting propagation like Bessel beams. The exciting finding can be used to produce high power nondiffracting beams and a variety of optical traps from compact and flexible fiber devices.

In this chapter, the concept of Bessel beam is introduced first. Then the principle of generating nondiffracting beams from an MMI fiber device is presented. Last, high power nondiffracting beams generating from an active MMI fiber device is proposed.

4.1 Bessel Beams

Bessel beam was first noted by Durnin [39, 40] when he examined the exact solution to the homogeneous Helmholtz equation in the cylindrical coordinates

$$\frac{d^2 R(r)}{dr^2} + \frac{1}{r} \frac{dR(r)}{dr} + R(r) \left(k_r^2 - \frac{m^2}{r^2} \right) = 0, \quad (4.2)$$

where $k_r = (k^2 - \beta^2)^{1/2}$, $k = 2\pi/\lambda$, and β is the propagation constant. Eq. (4.2) is obtained by substituting a separable complex amplitude $a(r, \phi, z) = R(r)\Phi(\phi)\exp(i\beta z)$ into the source-free Helmholtz equation

$$(\nabla^2 + k^2)a(x, y, z) = 0. \quad (4.3)$$

The function $\Phi(\phi)$ describing azimuthal dependence of the transverse amplitude profile of the beam must be periodical and is assumed to be

$$\Phi(\phi) = \exp(\pm im\phi), \quad m = 0, 1, 2, \dots \quad (4.4)$$

The physical solutions to Eq. (4.2) are the m -th order Bessel functions of the first kind $J_m(k_r r)$. Therefore, the beam described by the electric field $E(r, \phi, z, t) = J_m(k_r r)\exp(\pm im\phi)\exp(i\beta z)$ is called Bessel beam and is propagation invariant in free space because its intensity profile does not change as the beam propagates

$$I(r, \phi, z \geq 0) = |E(r, \phi, z)|^2 = J_m^2(r) = I(r, \phi, z = 0). \quad (4.5)$$

The intensity profile of a zeroth-order Bessel beam ($m = 0$) is shown in Fig. 4.1 and has a very bright central spot. The amount of energy contains in each ring of the Bessel

distribution is almost equal to the amount of energy contains in the central spot. Therefore, the power density in the central spot is much higher than that in the concentric rings. The high-order Bessel beams have a phase singularity on the beam axis and hence have a nondiffracting dark core. The intensity profile for a first-order Bessel beam is shown in Fig. 4.2. It is worthy noting that a high-order Bessel beam carries an orbital angular momentum that equals to $m\hbar$. In the past two decades, zeroth-order Bessel beams have been most intensively investigated.

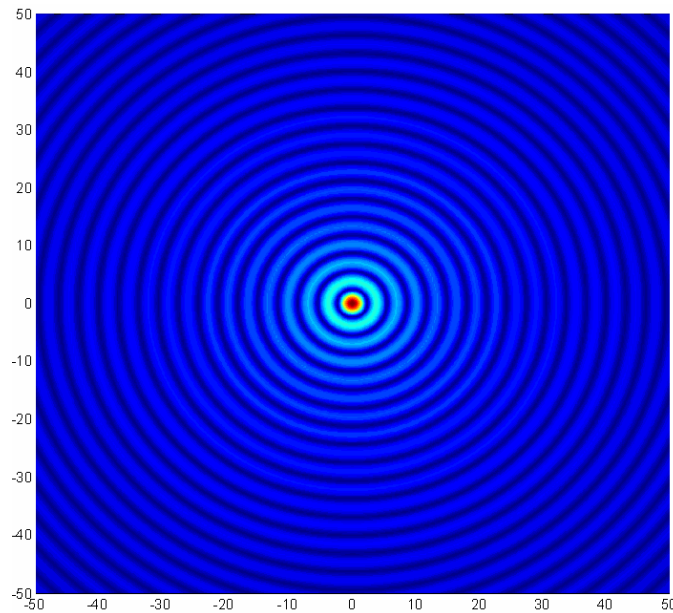


Fig. 4.1. Intensity profile of a zeroth-order Bessel beam.

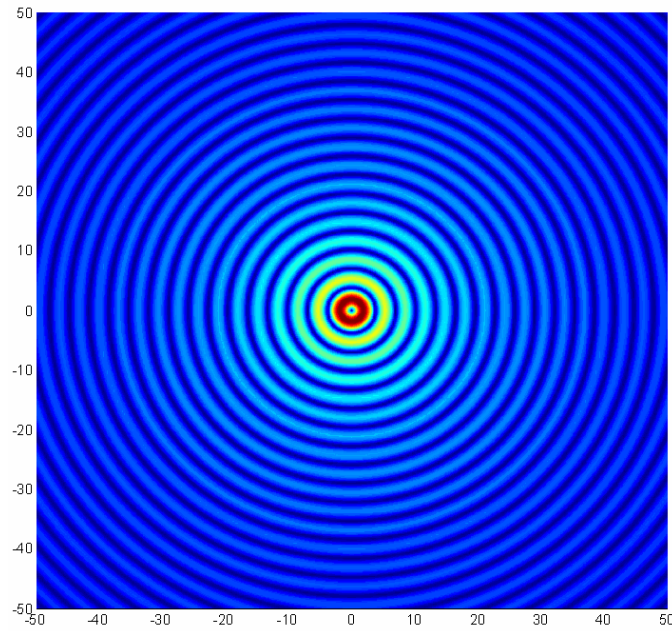


Fig. 4.2. Intensity profile of a first-order Bessel beam.

Because the field $E(r,\phi,z,t)$ of an Bessel beam extends to infinite and is not square integrable, therefore an ideal Bessel beam is not physically realizable. However, it is possible to generate an approximated or apertured Bessel beam whose central pattern shows a remarkable small diffraction spreading on propagation. The propagation of an apertured field of the Bessel beam shown in Figs. 4.1 with a diameter of $100\ \mu\text{m}$ is plotted in Fig. 4.3. Clearly, the central spot is significantly resistant to the diffractive spreading in contrast to the propagation of a Gaussian beam that is confined in a same

area as the central region of the Bessel field (the Rayleigh range of the corresponding Gaussian beam is about $13 \mu\text{m}$).

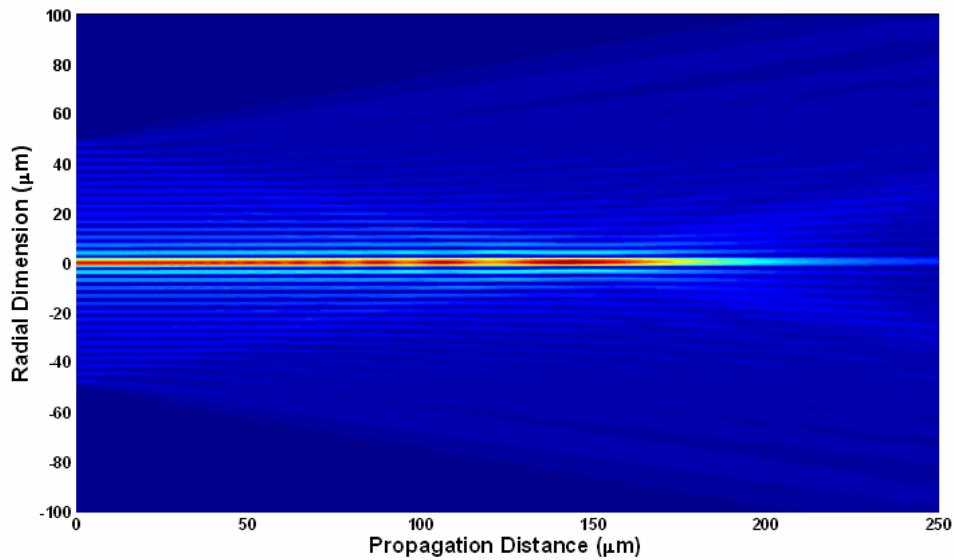


Fig. 4.3. Radial intensity profile of the Bessel beam shown in Fig. 4.1 in the propagation direction.

Propagation invariance of the intensity profile of Bessel beams can be explained as a result of a set of plane waves propagating on a conic surface (illustrated in Fig. 4.4). Mathematically, the angular spectrum of a Bessel beam is a ring in k -space described by the Dirac delta function $\delta(k-k_r)$. Thus the optical Fourier transform of a ring will result in

a Bessel beam, and this is the basis of most methods of generating an approximated Bessel beam in literature.

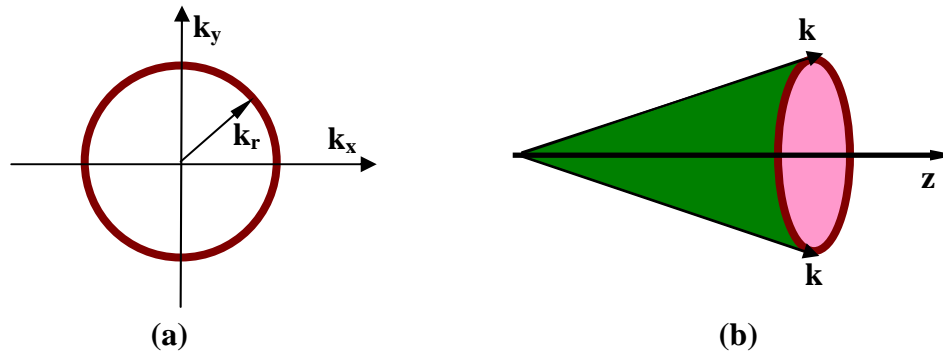


Fig. 4.4. (a) Angular spectrum of a Bessel beam; (b) the k -vectors of the Bessel beam propagate on a conic surface

The radius of the central bright spot r_0 is given by the first zero-point of the Bessel function and can be written as

$$r_0 = \frac{2.405}{k_r}. \quad (4.6)$$

Therefore, the larger the opening angle of the cone defined by the waves traversing its surface, the smaller the central spot. Evanescent Bessel beams [41] can have a tiny central spot because its radial vector k_r can be larger than the k vector. Note that, intensity of evanescent Bessel beams decays rapidly although their transverse shape can be maintained at a long distance.

Another interesting property of the Bessel beam is self-healing, i.e., the beam can resist against amplitude and phase distortions. When an opaque obstacle is placed in the center of the beam, the intensity profile of the incident beam can be reformed after a distance given by

$$z_{\min} \approx \frac{ak}{2k_z} \quad (4.7)$$

where a is the radius of the obstruction. When an opaque obstacle is placed $25 \mu\text{m}$ behind the source shown in Fig. 4.1, the reconstruction of the original field can be accomplished at about $25 \mu\text{m}$ behind the obstacle, as shown in Fig. 4.5.

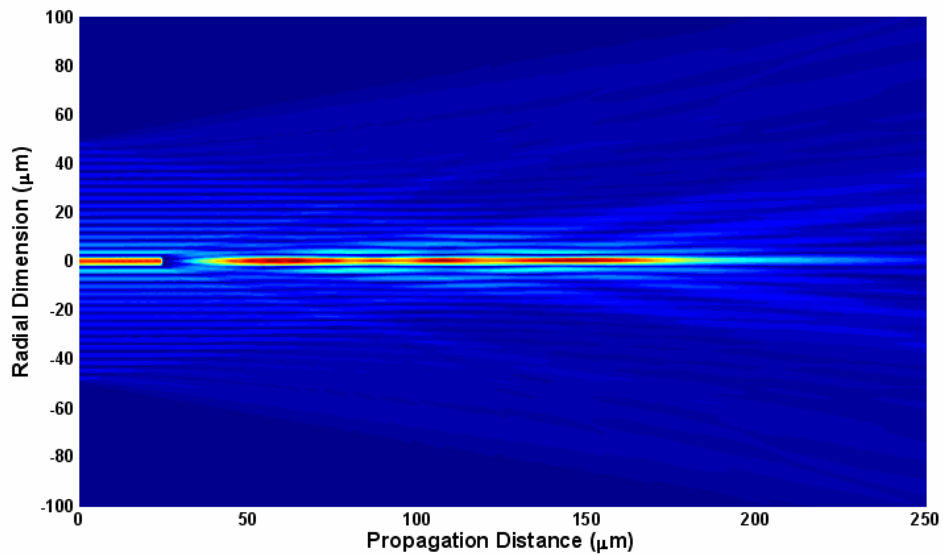


Fig. 4.5. Reconstruction of a Bessel beam when its central spot is blocked by an obstruction.

Bessel beams have been intensively investigated in the past two decades because of their many practical and potential applications, such as optical driving [42-44], particle guiding and manipulation [45-47], nonlinear optics [48, 49], waveguide generation [50], optical interconnection [51], interferometry [52], microfabrication [53], and lithography [54]. Although an ideal Bessel beam is impossible to be realized experimentally, a variety of methods of generating an approximated Bessel beam with finite field area have been demonstrated in literature [40, 55-67].

Most common techniques are based on the physics explanation that a Bessel beam results from the interference of plane waves propagating on a conic surface. In the first observation of the Bessel beam, an annular aperture was placed at the focal plane of a lens [40, 68] as shown in Fig. 4.6. However, this method is rather inefficient because most of the incident power is obstructed by the annular slit. And the on-axis intensity of the beam oscillates rather widely before falling off rapidly at the end of the propagation distance. A Bessel beam can be created using an axicon [55, 68], or conical lens element, as shown in Fig. 4.7. The use of an axicon is an efficient and the best known method of generating Bessel beams. Especially, the rapid on-axis intensity oscillation associated with the annular slit method is removed. By imprinting the appropriate phase of a Bessel beam onto an incoming Gaussian beam, efficient Bessel beam can be generated using static, etched hologram or computer-generated hologram [56-58]. Some special

techniques, such as utilizing localized modes [59] and parametric frequency doubling [60], can generate Bessel beams from cavities.

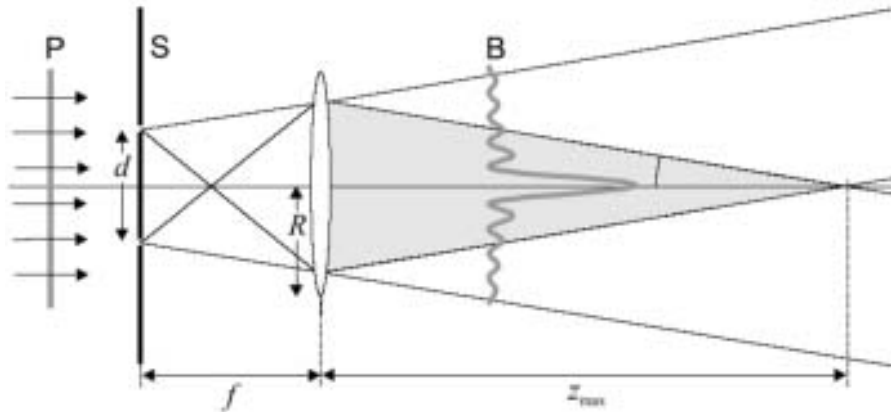


Fig. 4.6. Durnin's first demonstration of Bessel beam [68]

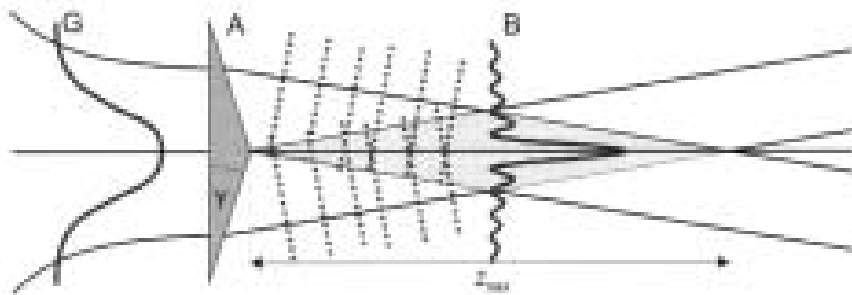


Fig. 4.7. Bessel beam generated by use of an axicon lens [68].

Recently, several techniques different from the common concept have been proposed, such as using an opaque disk [61] and a tunable acoustic gradient index of refraction lens [62]. However, all these methods mentioned above are bulk optics, free-space elements and require careful alignment.

In order to overcome the disadvantage of bulk elements and offer the possibility of producing Bessel-like beams with a compact fiber device, microaxicons [63-65] and whispering gallery mode resonators [66] fabricated on the fiber end have been proposed. But their manufacturing process is costly, complicated, and difficult to control. Very recently, Ramachandran [67] demonstrated a novel method to generate Bessel-like beam from an optical fiber with a long-period fiber Bragg grating inscribed into its core. This method, however, needs special equipments to fabricate the grating.

In next section, we present an extremely simple and low-cost method to generate non-diffractive beams from optical fibers. In contrast to any previously demonstrated device, the beam generated from our fiber device can be easily manipulated. Moreover, as a consequence of multimode interference, the output beam can form a variety of arrays that can only be obtained from interfering Bessel beams using complicated optical systems [69-73].

4.2 Generation of Nondiffracting Beams from Multimode Fibers

4.2.1 The principle

The method of generating nondiffracting beams from multimode (MM) fibers were found while the intensity profile evolution of the beam from the MM fiber of the MMI fiber structure shown in Fig. 2.21 was investigated. Therefore, the design of the fiber device to generating nondiffracting beams is the same as that shown in Fig. 2.21 and is schematically shown in Fig. 4.8. A conventional single-mode fiber is directly spliced onto a short-piece of large-core multimode (MM) fiber. Since the performance of this fiber device depends on the wavelength of the launched light [34], a single-frequency semiconductor laser with a wavelength-tunable range from 1456 to 1584 nm was used as the signal source.

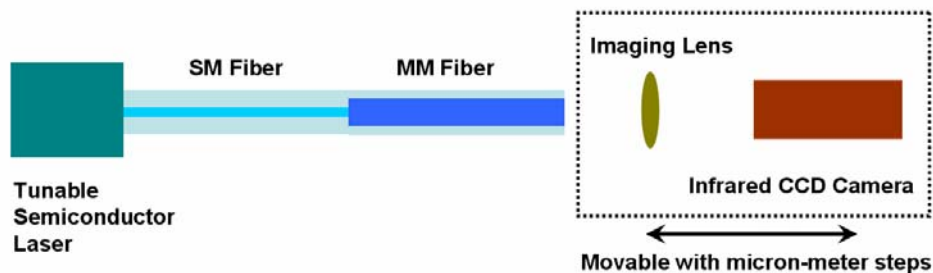


Fig. 4.8. Design of a fiber device generating nondiffracting beams (the figure is not to scale).

Based on the fiber device shown in Fig. 4.8, when the $LP_{0,1}$ mode (the fundamental mode) of the SM fiber is coupled to the MM fiber, only $LP_{0,n}$ modes (n is the radial index) are excited due to mode orthogonality and on-axis excitation. Mathematically and physically, the fields of the $LP_{0,n}$ modes in the MM fiber core are represented by apertured Bessel functions $J_0(\kappa_{fn}r)$ with different transverse wave vectors, $\kappa_{fn} = (n_f^2 k^2 - \beta_{fn}^2)^{1/2}$. Here, $k = 2\pi/\lambda$, n_f is the refractive index of the fiber core, and β_{fn} is the propagation constant of the $LP_{0,n}$ mode, respectively; r is the radial coordinate and smaller than the core radius of the MM fiber R . Because each $LP_{0,n}$ mode propagates along the waveguide independently with its own propagation constant, the field at the output facet of the MM fiber is the superposition of the Bessel-like fields

$$E_{Out}(r, L) = \sum_{n=1}^N C_n J_0(\kappa_{fn}r) e^{-i\beta_{fn}L}, \quad r \leq R \quad (4.8)$$

where, L is the MM fiber length, N is the number of the strongly excited modes in the MM fiber segment, and C_n is the decomposition coefficient defined by Eq. (2.2) and can be rewritten by

$$C_n = \frac{\iint E(r, \phi, 0) J_0(\kappa_{fn}r) r dr d\phi}{\iint J_0^2(\kappa_{fn}r) r dr d\phi}. \quad (4.9)$$

Because the Bessel fields are the solutions of the Helmholtz equation in circular cylindrical coordinates [39], ignoring the Fresnel reflection, the field in the free space can be approximately expressed as

$$E_{fs}(r, z) = \sum_{n=1}^N C_n J_0(\kappa_n r) e^{-i(\beta_n z + \beta_m L)} \quad (4.10)$$

Where, $\kappa_n = \kappa_{fn}$ and $\beta_n = (k^2 - \kappa_n^2)^{1/2}$. Therefore, as a consequence of superposition of multiple Bessel fields, the propagation of the beam in the free-space can be diffraction-free and optical arrays can be generated at certain axial regions [69-73]. It should be pointed out that Eq. (4.10) only applies for the propagation-invariant field close to the optical axis and the entire field should be obtained from the field $E_{out}(r, L)$ by use of diffraction theory.

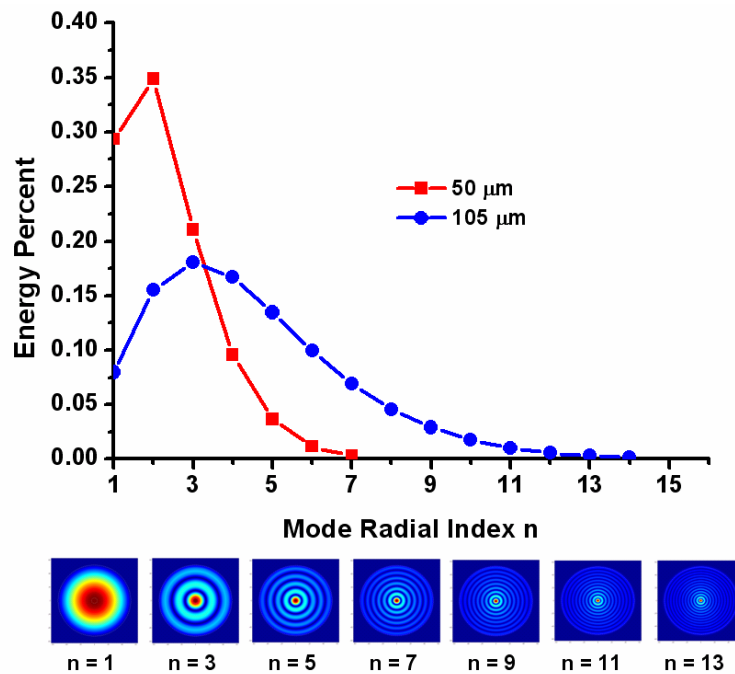


Fig. 4.9. Energy percentage of the strongly excited modes inside the MM fiber segment with core diameters of 50 μm and 105 μm , respective, when the input SM fiber is SMF-28, and the intensity profiles of the odd-th excited modes inside the 105 μm MM fiber.

It should be noted that, the phenomenon of nondiffracting propagation, i.e., the intensity profile close to the optical axis maintains its shape in a propagation distance much longer than the rayleigh distance defined by Eq. (4.1), is noticeable only when higher order $LP_{0,n}$ modes are excited because their mode fields resemble closely a real Bessel field. As an illustration, the intensity profiles of the odd-th $LP_{0,n}$ modes inside the 105 μm MM fiber are plotted in Fig. 4.9. In Fig. 4.9, the energy percentage of the excited modes is plotted for the 50 μm and 105 μm MM fibers, respectively, when the input fiber is an SMF-28. It is straightforward that the larger the core diameter of the MM fiber, the more $LP_{0,n}$ modes are excited and the more energy is coupled to higher $LP_{0,n}$ mode. Therefore, a large ratio of the core diameter between the MM fiber and the SM fiber is beneficial for confining most energy in a small area for a long propagation distance. Although lower order $LP_{0,n}$ mode field do not resemble a nondiffracting Bessel field, their field depths are still very long due to their small transverse vectors k_r . Therefore they can still contribute to the nondiffracting profile through the interference with other $LP_{0,n}$ modes. In comparison with other devices to generate a single Bessel field, this fiber device can accumulate more energy in the desired nondiffracting patterns or arrays (usually the central spot or the first ring). The radial intensity profile evolution of the first five $LP_{0,n}$ modes, $LP_{0,7}$ mode, and $LP_{0,9}$ mode is plotted in Fig. 4. 10. Clearly, for a high order mode, its entire beam has a large diverging angle due to the large transverse vector.

Nevertheless, the higher order $LP_{0,n}$ mode exhibits a property of nondiffracting to a larger extent than the lower order $LP_{0,n}$ mode. On-axis intensity of the intensity profiles shown in Fig. 10 is plotted in Fig. 11. The oscillation of the intensity evolution results from the edge effect of the aperture.

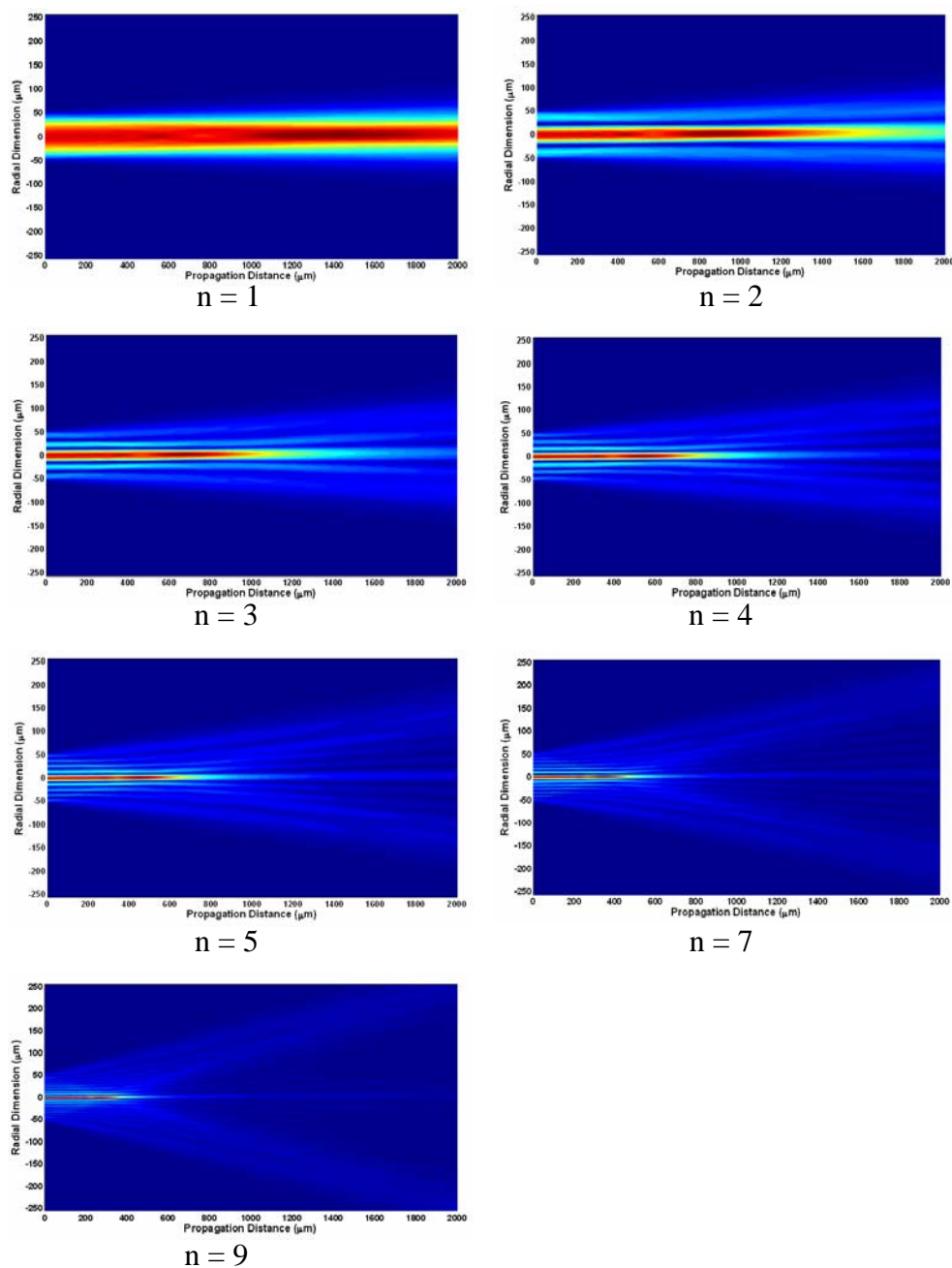


Fig. 4.10. Radial intensity profile evolution in the propagation direction of the first five $LP_{0,n}$ mode, $LP_{0,7}$ mode and $LP_{0,9}$ mode.

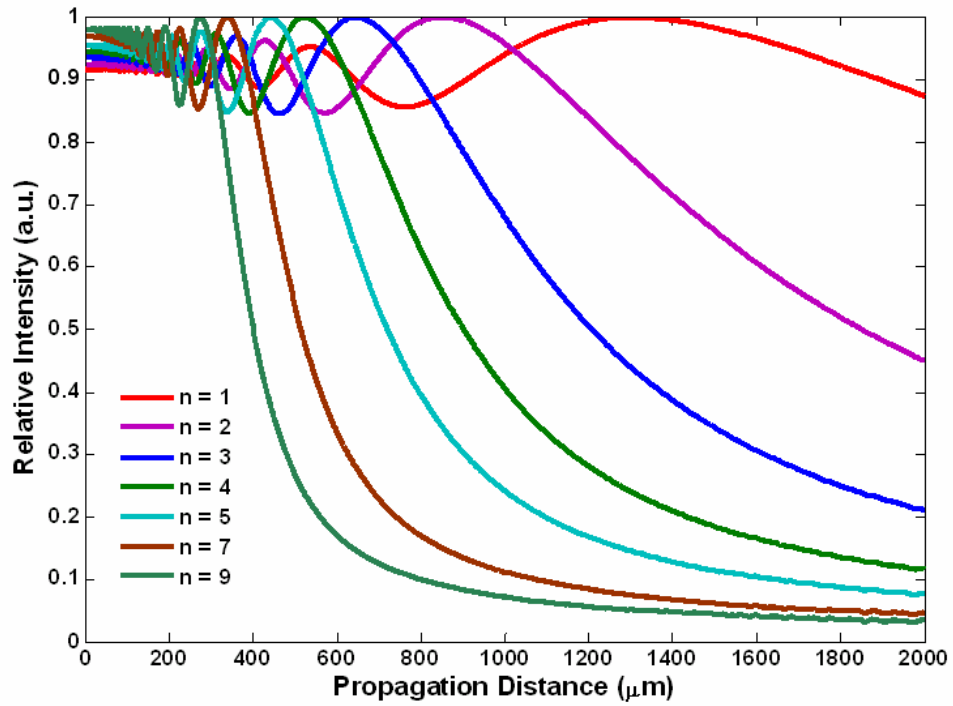


Fig. 4.11. On-axis intensity evolution of the first five $\text{LP}_{0,n}$ mode, $\text{LP}_{0,7}$ mode and $\text{LP}_{0,9}$ mode in the propagation direction.

4.2.2 Simulations

In order to understand the behavior of the beam generated from the MMI fiber device, theoretical calculations based on Eq. 4.8 and the diffraction theory are carried out in this section. The field in free space is obtained by the approach of optical transfer function (OTF) as follows,

$$E(r, z) = FT^{-1}[FT[E_{out}(r, L)]\exp(i\kappa(\xi)z)], \quad (4.11)$$

where FT represents the Fourier transform, FT^{-1} represents the inverse Fourier transform, and ξ is the coordinate in the k-space.

Because the propagation constants β_n and β_{nf} in Eq. (4.10) are wavelength dependent, the beam from the MMI fiber device can exhibit varying propagation behaviors for the different signal wavelengths. Consequently, the nondiffracting pattern or array generated by this fiber device can be easily controlled by changing the wavelength of the single-frequency signal. Therefore, wavelength dependence of the beam propagation is focused in the simulation.

When a 10 cm long 50 μm MM fiber is used, the intensity profile at the fiber facet and the radial intensity evolution in the propagation direction for several typical wavelengths are plotted in Figs. 4.12-4.14. Clearly, a variety of optical arrays are formed

for different wavelength signals. On-axis intensity of the beam shown in Figs. 4.12-4.14 is plotted in Figs. 4.15-4.17 accordingly.

When the wavelength is 1510 or 1550 nm, the beam propagates in free space for a long propagation distance with high on-axis intensity. When the wavelength is 1520, 1585, or 1595 nm, dark optical traps are formed. When the wavelength is 1540, 1555, or 1590 nm, bright optical traps can be obtained. When the interesting wavelength is 1575 nm, two dark optical traps and one bright optical trap can be generated.

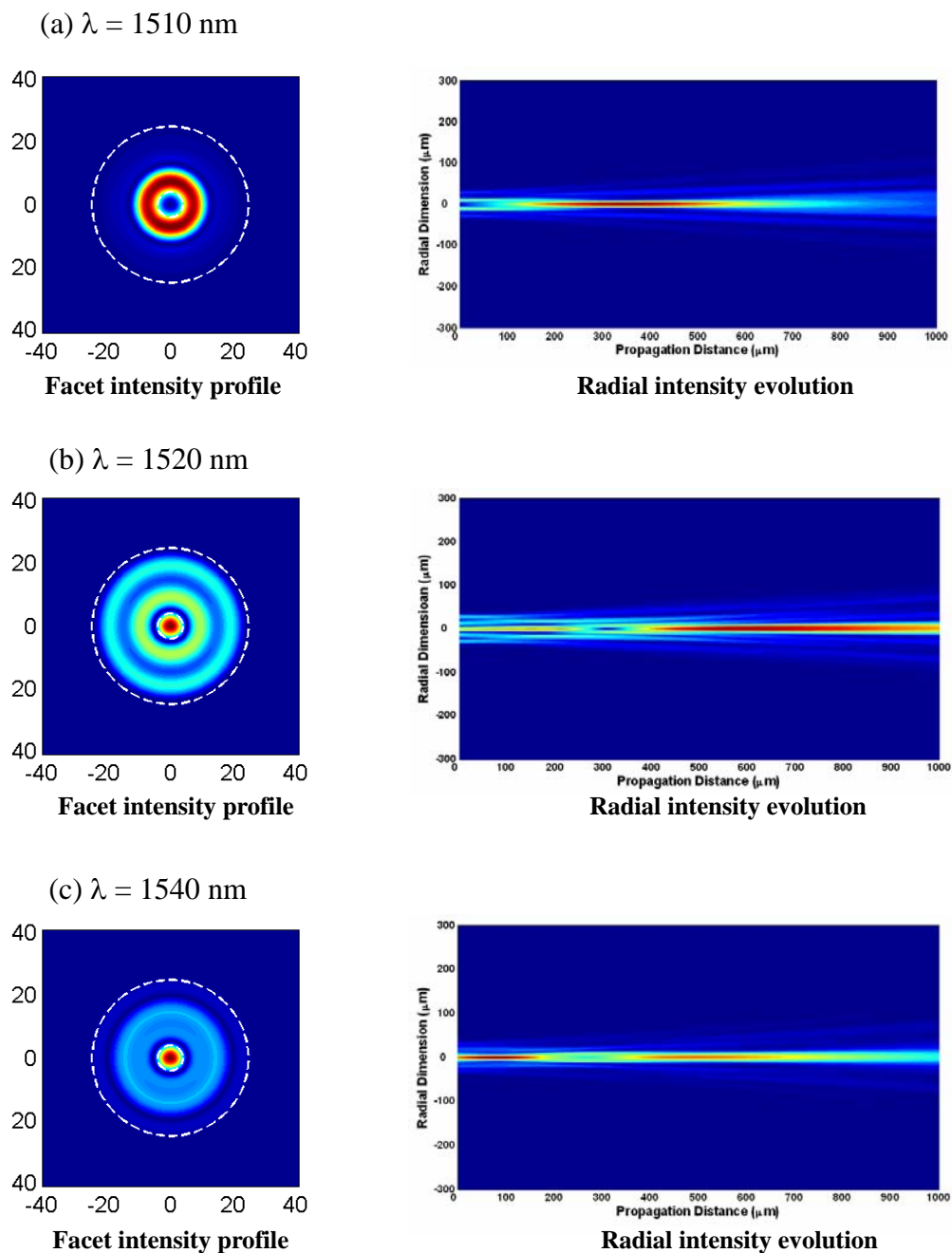


Fig. 4.12. Facet intensity profile and radial intensity evolution of the beam coming from the 50 μm MMI fiber device when the signal wavelength is 1510, 1520, and 1540 nm, respectively.

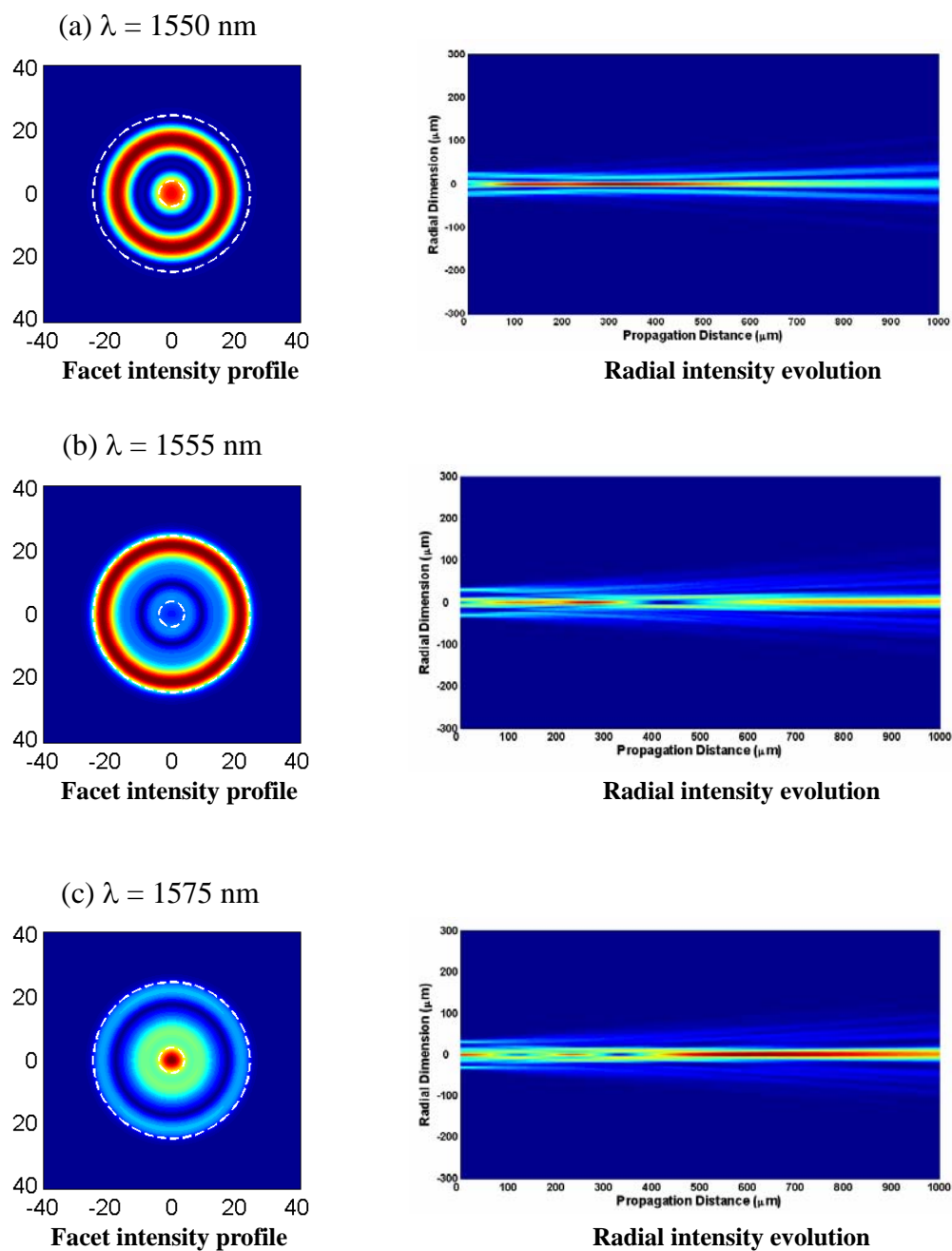


Fig. 4.13. Facet intensity profile and radial intensity evolution of the beam coming from the $50\ \mu\text{m}$ MMI fiber device when the signal wavelength is 1550, 1555, and 1575 nm, respectively.

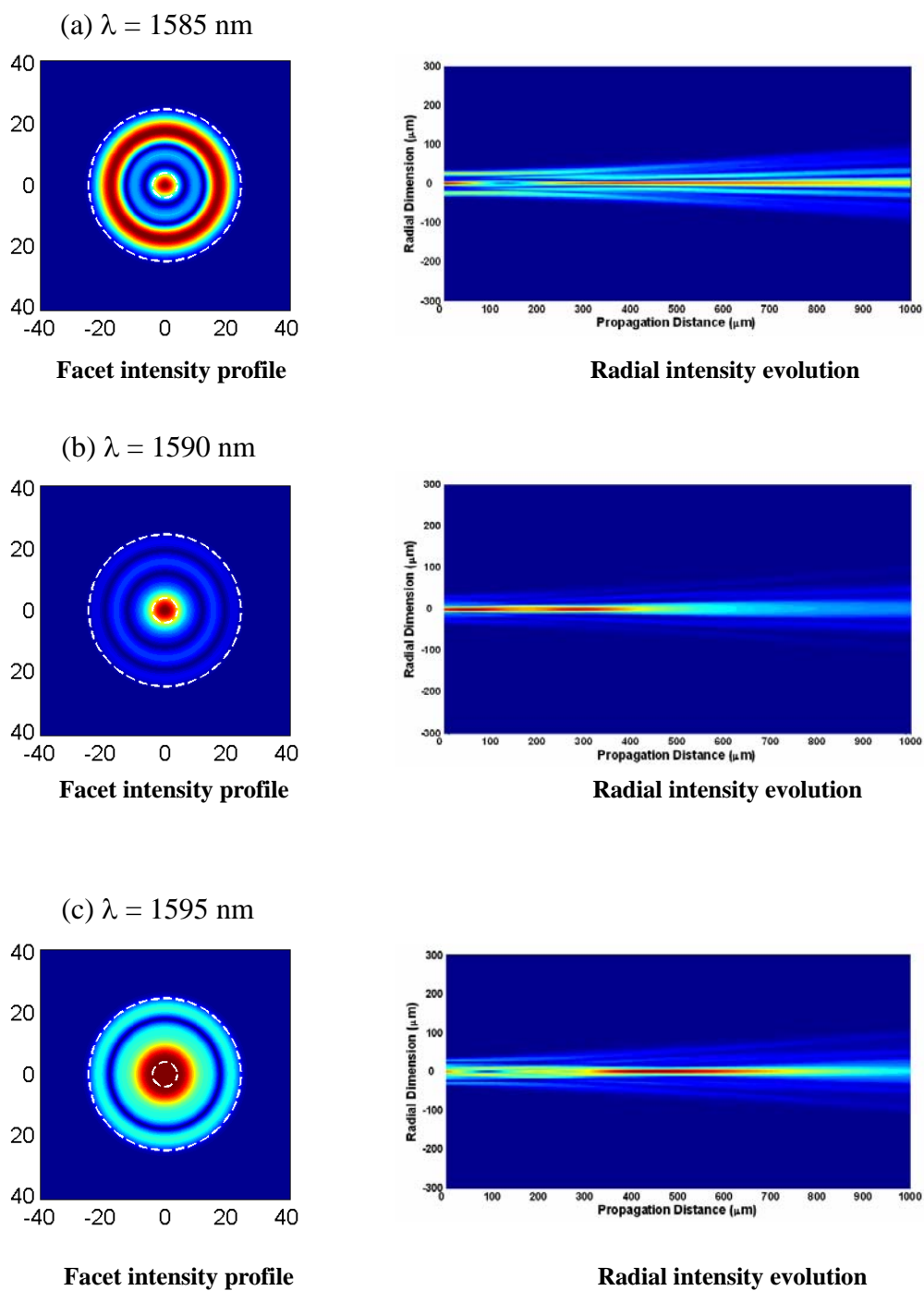


Fig. 4.14. Facet intensity profile and radial intensity evolution of the beam coming from the 50 μm MMI fiber device when the signal wavelength is 1585, 1590, and 1595 nm, respectively.

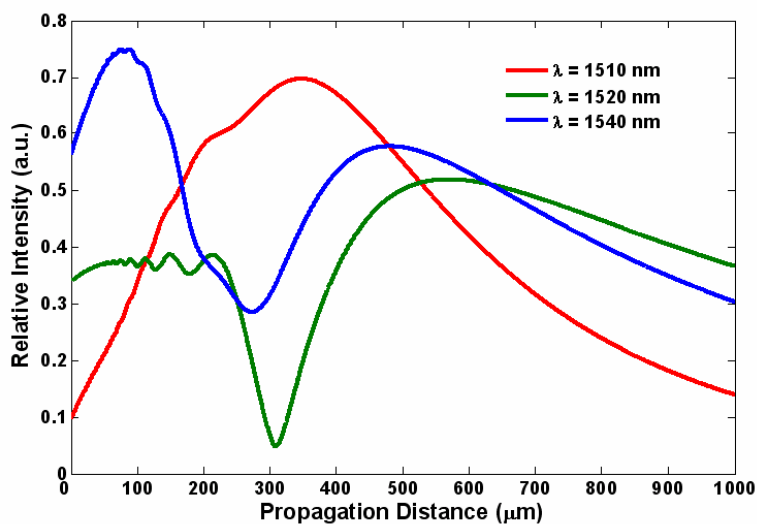


Fig. 4.15. On-axis intensity of the beam coming from the 50 μm MMI fiber device when the signal wavelength is 1510, 1520, and 1540 nm, respectively.

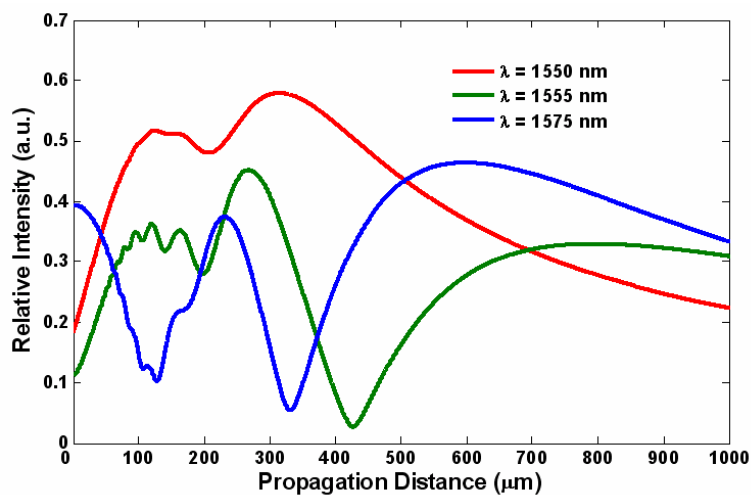


Fig. 4.16. On-axis intensity of the beam coming from the 50 μm MMI fiber device when the signal wavelength is 1550, 1555, and 1575 nm, respectively.

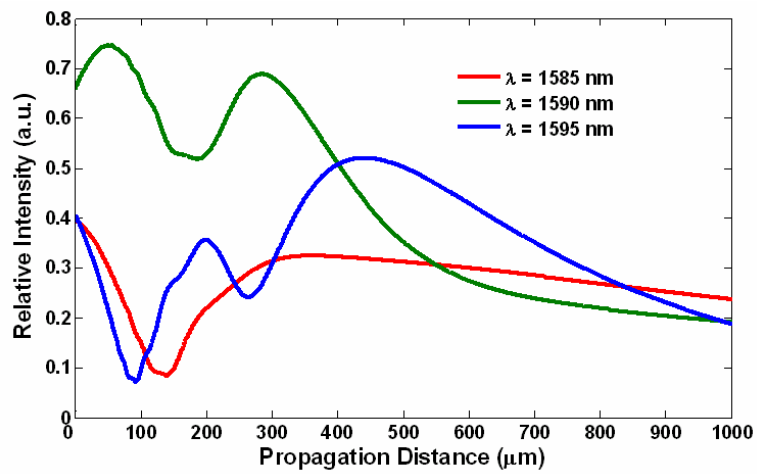
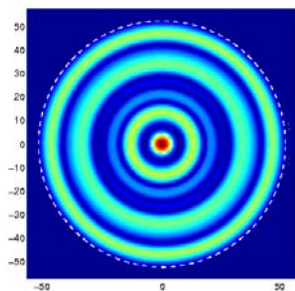


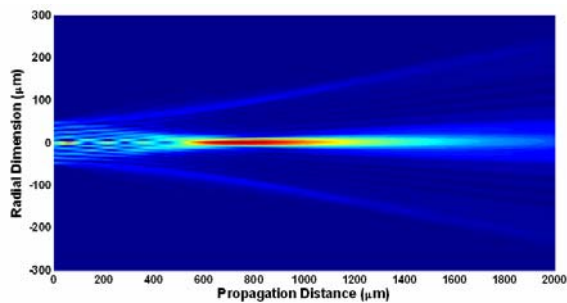
Fig. 4.17. On-axis intensity of the beam coming from the 50 μm MMI fiber device when the signal wavelength is 1585, 1590, and 1595 nm, respectively.

Since the length of the 50 μm MM fiber is not close to a self-imaging position, the self-imaging effect in free space cannot be observed. In the following simulation of 105 μm MM fiber, therefore, a fiber length very close to a self-imaging position of 43 mm is used. The intensity profile at the fiber facet and the radial intensity evolution in the propagation direction for several typical wavelengths are plotted in Figs. 4.18-4.20. Clearly, for wavelengths shorter than 1550 nm, one optical trap like that focused by a conventional lens can be obtained due to the self-imaging effect in free space. The optical trap goes closer to the fiber facet as the wavelength becomes longer and its trap length becomes shorter as well. On-axis intensity of the beam shown in Figs. 4.18-4.20 is plotted in Figs. 4.21-4.23 accordingly. When the wavelength is longer than 1550 nm, clustering optical traps with very small dimension can be obtained.

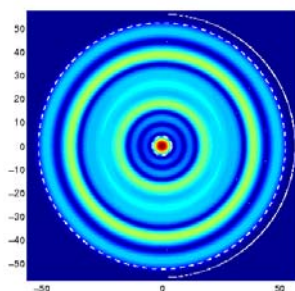
The simulation results of the 50 μm and the 105 μm fibers indicate the beams coming from the MMI fiber device can be controlled or selected by changing the signal wavelength or the MM fiber length. The wavelength dependence of the propagation behavior can be utilized to generate flexible optical traps that may have a promising application in particle trapping.

(a) $\lambda = 1500$ nm

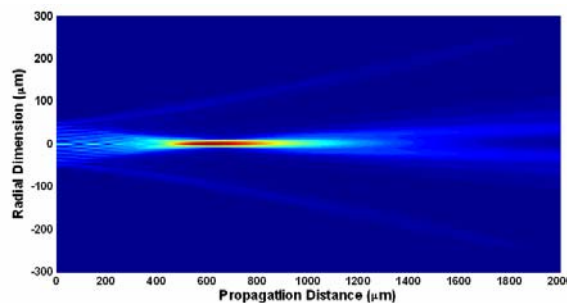
Facet intensity profile



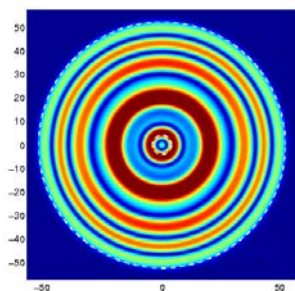
Radial intensity evolution

(b) $\lambda = 1510$ nm

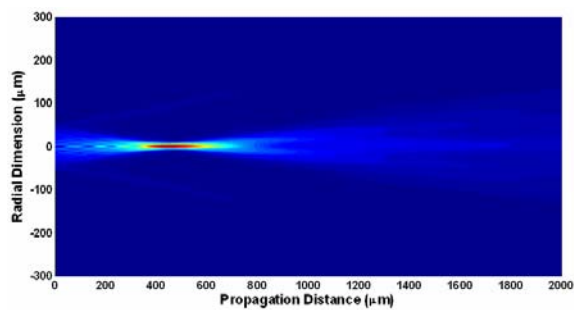
Facet intensity profile



Radial intensity evolution

(c) $\lambda = 1520$ nm

Facet intensity profile



Radial intensity evolution

Fig. 4.18. Facet intensity profile and radial intensity evolution of the beam coming from the $105 \mu\text{m}$ MMI fiber device when the signal wavelength is 1500, 1510, and 1520 nm, respectively.

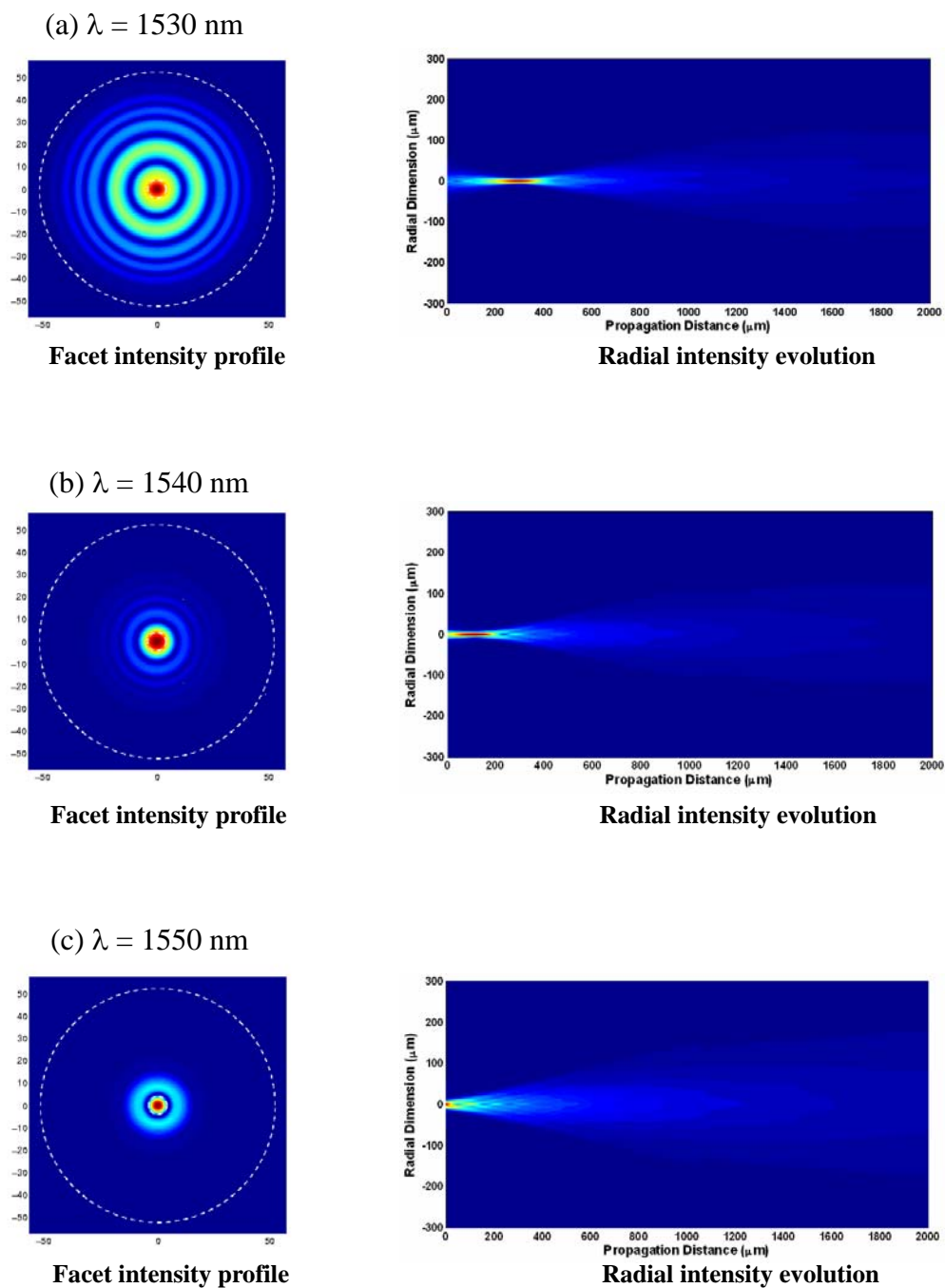
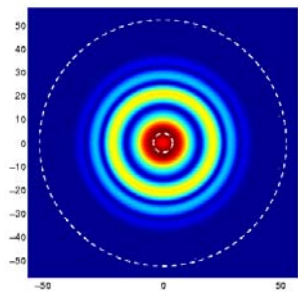
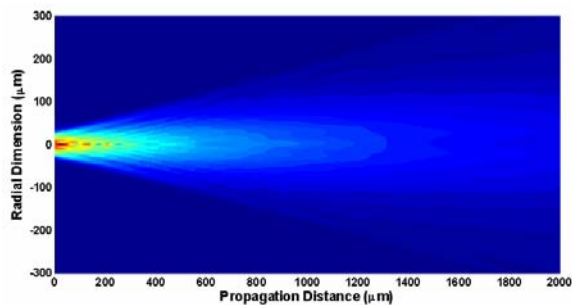


Fig. 4.19. Facet intensity profile and radial intensity evolution of the beam coming from the 105 μm MMI fiber device when the signal wavelength is 1530, 1540, and 1550 nm, respectively.

(c) $\lambda = 1560$ nm

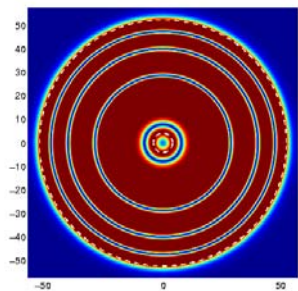


Facet intensity profile

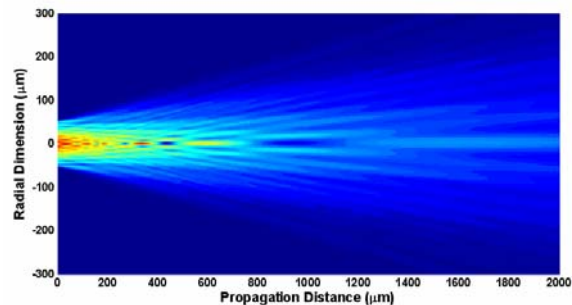


Radial intensity evolution

(c) $\lambda = 1570$ nm

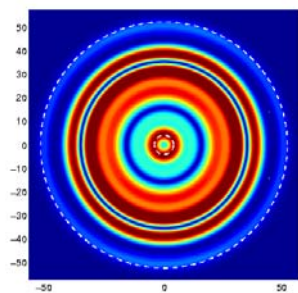


Facet intensity profile

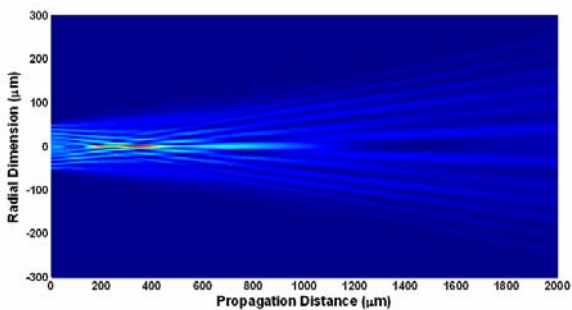


Radial intensity evolution

(c) $\lambda = 1580$ nm



Facet intensity profile



Radial intensity evolution

Fig. 4.20. Facet intensity profile and radial intensity evolution of the beam coming from the 105 μm MMI fiber device when the signal wavelength is 1560, 1570, and 1580 nm, respectively.

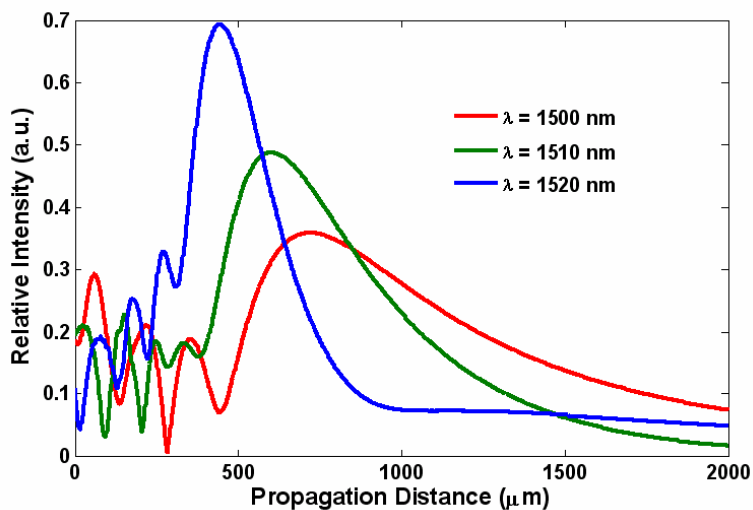


Fig. 4.21. On-axis intensity of the beam coming from the 105 μm MMI fiber device when the signal wavelength is 1500, 1510, and 1520 nm, respectively.

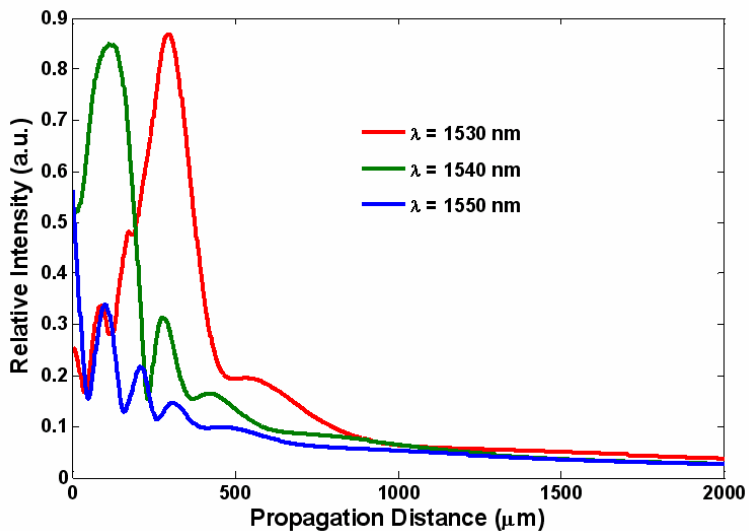


Fig. 4.22. On-axis intensity of the beam coming from the 105 μm MMI fiber device when the signal wavelength is 1530, 1540, and 1550 nm, respectively.

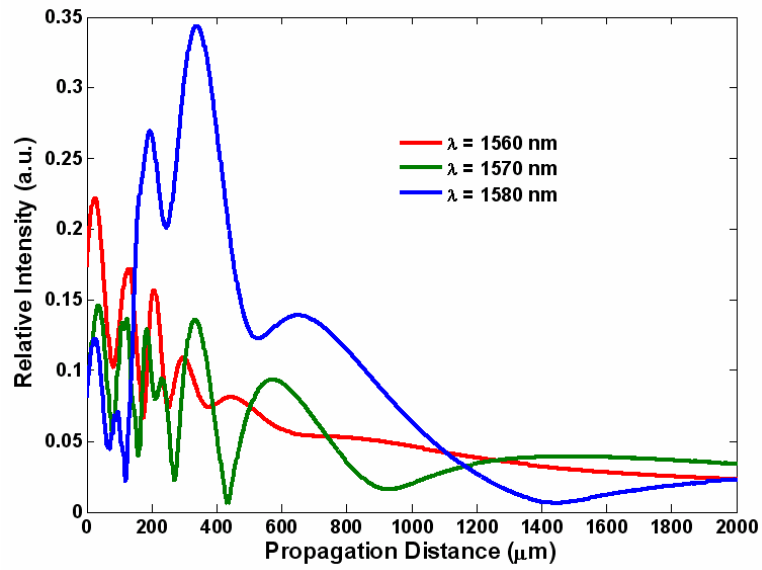


Fig. 4.23. On-axis intensity of the beam coming from the 105 μm MMI fiber device when the signal wavelength is 1560, 1570, and 1580 nm, respectively.

4.2.3 Experimental results

In order to measure the intensity profile evolution in the propagation distance, an objective lens with a large numerical aperture is used to magnify the optical field. The transverse intensity profile of the generated beam is recorded by an infrared camera. The objective lens and the CCD camera can be moved forward or backward together to record the intensity profile at selected positions.

In Fig. 4.24, for the signal of 1545 nm and 1570 nm, the intensity profiles at selected planes are shown for the beam from a 10 cm 50 μm MM fiber segment. Clearly, the propagation of the beam from the fiber device exhibits a very small diffraction. When the signal wavelength is 1545 nm, the nondiffracting pattern near the fiber facet is a very bright ring (a bottle beam [70]) and changes to a bright central spot after a propagation of 50 μm . At the position of 150 μm it goes back to a bright ring and then changes to a bright spot again at 250 μm . Clearly, three-dimensional optical traps are formed in this case. When the signal is 1570 nm, however, the nondiffracting pattern is always a bright on-axis spot as a result of constructive addition at the center. The on-axis intensity relative to its maximal value at selected distances from the MM fiber facet is plotted in Fig. 4.25 for the two nondiffraction beams. In comparison, the intensity evolution of the beam from the SMF-28 fiber is also plotted in Fig. 4.25 (black squares). For the beam

coming from the SMF-28 fiber, the peak intensity reduces to a half value after propagating $\sim 50 \mu\text{m}$ as a consequence of diffraction. However, for the 1570 nm beam coming from the MMI fiber device, the peak intensity of the central spot can be maintained above half of its maximal value for a propagation distance of more than 400 μm . It should be emphasized that, different from a single Bessel beam in which each ring contains energy nearly equal to that of the central spot, for the beam generated from this fiber device, most of the energy can be accumulated in the desired nondiffracting pattern.

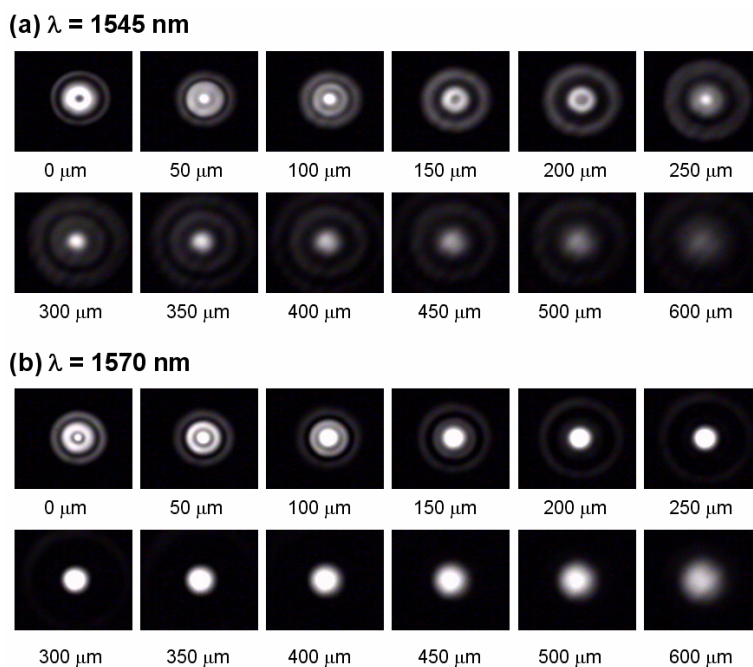


Fig. 4.24. Intensity profiles at selected distances from the MM fiber facet for signal wavelengths of (a) 1545 nm and (b) 1570 nm, respectively.

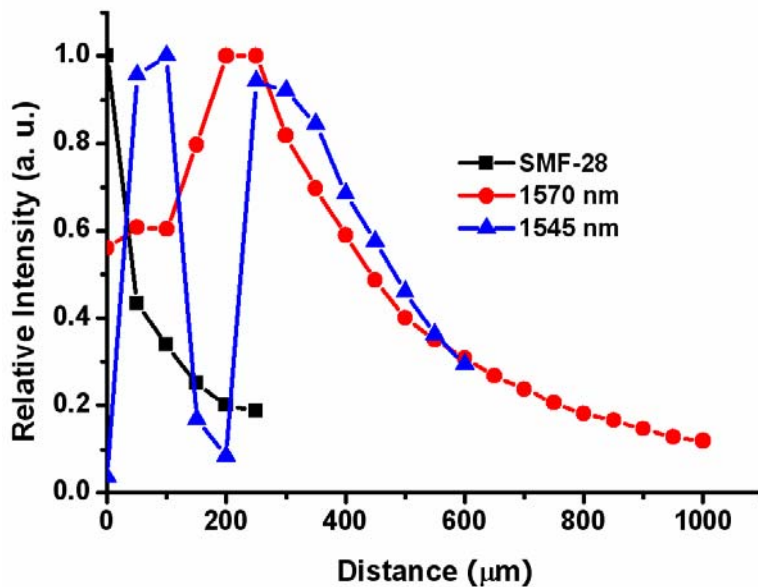


Fig. 4.25. On-axis intensity at the selected distances from the MM fiber facet for signal wavelengths of 1545 nm (blue triangles) and 1570 nm (red circles), respectively, and from a SMF-28 fiber (black squares).

In Fig. 4.26, the intensity profiles at selected planes are shown for the beam from a 43.2 cm long 105 μm MM fiber segment for four typical cases. When the signal wavelength is 1510 nm, a bottle beam can be obtained at positions around 250 and 500 μm , respectively, and an on-axis bright spot at other regions. When the signal wavelength changes from 1560 nm to 1580 nm, it is found that the on-axis bright spot starts closer to the MM fiber facet and its nondiffracting pattern maintains longer accordingly. The

relative on-axis intensity for the four cases is plotted in Fig. 4.27. Comparing the results in Fig. 4.25 and Fig. 4.27, it is obvious that the nondiffracting propagation distance of the beam from 105 μm fiber is much longer than that from 50 μm . For the 1580 nm beam, the on-axis intensity can be maintained above half of its maximal value for propagation distance of more than 800 μm . Because the larger ratio between the core diameters of the SM fiber and the MM fiber, higher $\text{LP}_{0,n}$ modes are excited, we can predict that much longer diffraction-free distance can be obtained when a smaller core SM fiber or a larger core MM fiber is used.

Although both the length of the 50 μm and the 105 μm MM fiber segments are chosen the same as those used in the calculations, the beam propagation behavior of the experiment is not exactly the same as that of the simulations. It should attribute to the slight difference between the MM fiber length in the experiment and the desired length.

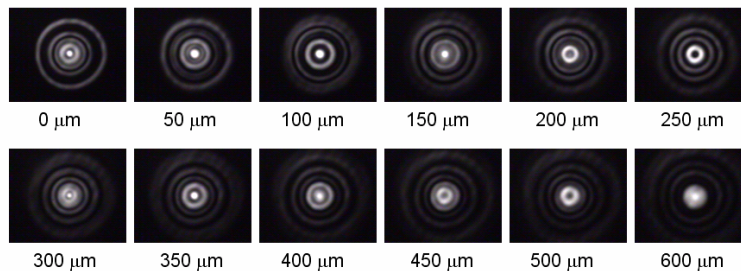
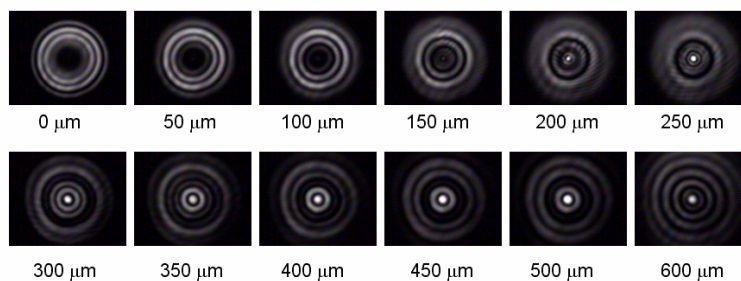
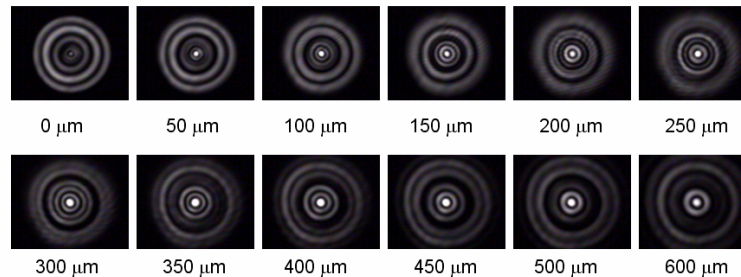
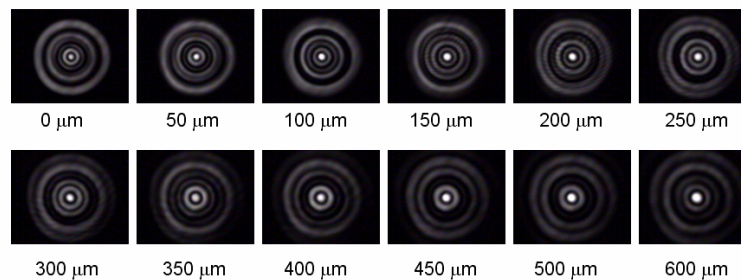
(a) $\lambda = 1510$ nm**(b) $\lambda = 1560$ nm****(c) $\lambda = 1570$ nm****(d) $\lambda = 1580$ nm**

Fig. 4.26. Intensity profiles at selected distances from the MM fiber facet for signal wavelengths of (a) 1510 nm, (b) 1560 nm, (c) 1570 nm, and (d) 1580 nm, respectively.

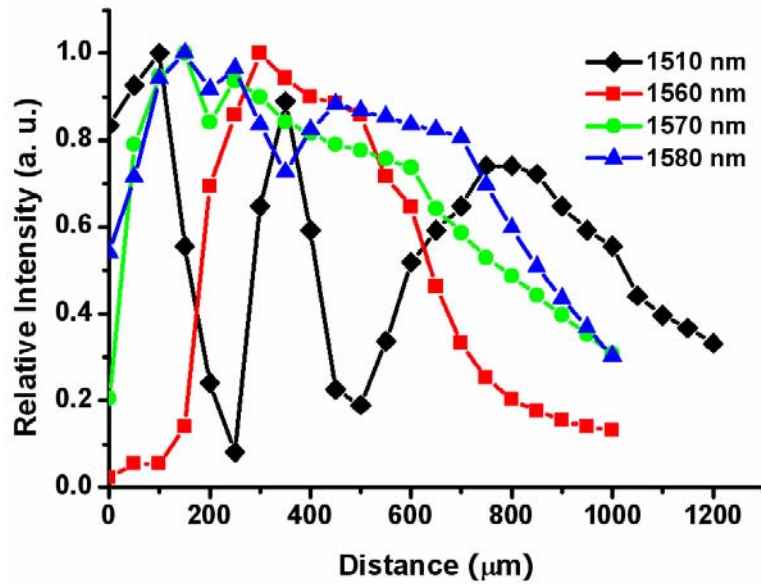


Fig. 4.27. On-axis intensity at the selected distances from the MM fiber facet for signal wavelengths of 1510 nm (black diamonds), 1560 nm (red squares), 1570 nm (green circles), and 1580 nm (blue triangles), respectively.

Since the phase difference between the excited $LP_{0,n}$ modes depends on the total length of the MM fiber segment, the dependence of the beam profile on wavelength also shows critical relation with the MM fiber length. When the MM fiber length is long, the beam profile varies fast with a change of signal wavelength. And the beam profile varies

slowly with a change of signal wavelength when the MM fiber length is short. Therefore, the beam profile from the fiber device can be easily and flexibly controlled through a proper MM fiber length and a signal wavelength.

The self-healing property of the beam from the MMI fiber device is also investigated by placing a needle with a diameter of about $100\ \mu\text{m}$ to block the center of the magnified beam after an objective lens, as shown in Fig. 4.28. The intensity profile at selected planes behind the needle is shown in Fig. 4.29. Clearly, the central spot is totally reconstructed when the beam propagates about 10 cm beyond the needle. The reconstruction of the nondiffracting beam can be applied for trapping particles at different planes [45].

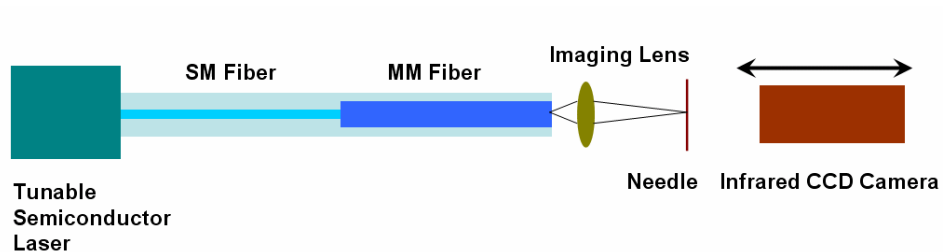


Fig. 4.28. Experimental setup to investigate the self-healing property of the nondiffracting beam generated from the fiber device.

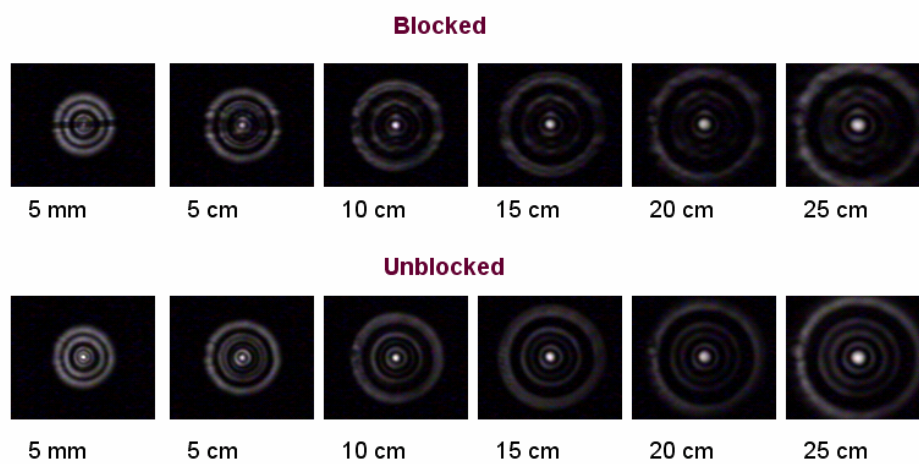


Fig. 4.29. Beam profiles at selected positions behind the plane of the needle for the case of blocking (upper row) and unblocking (lower row), respectively.

4.3 High Power Nondiffracting Beams Generation

The method of generating nondiffracting beams from MM fibers has been demonstrated experimentally and theoretically. Considering recent progress of high power fiber lasers and amplifiers, this technique can be applied to generate high power micron-size nondiffracting beams, which may have considerable applications in nonlinear optics, high-energy physics, atomic optics, and micro-fabrication. In general, a small-core input fiber is required to generate a small-size central spot. When the input fiber has a small core size, the launching power will be limited accordingly. In addition to extreme simplicity and controllability, big benefit of MMI fiber device is that the fiber segment can be active and the signal can be amplified. Therefore, high power nondiffracting beams can be obtained from the MM fiber in the designs shown in Figs. 4.30-4.31. In Fig. 30, a short-piece of passive MM fiber can be splice to an active SM fiber. The signal is amplified through SM launching fiber and converted into a diffractionless beam via MMI inside the passive MM fiber. In Fig. 31, the MM fiber is active and provides the gain. The advantage of this design is that the constraints of SM active fiber can be overcome.

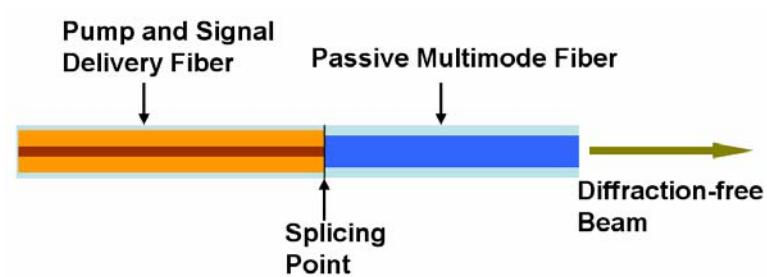


Fig. 4.30. A proposed active fiber device generating high power diffraction-free beams (SM fiber provides the gain).

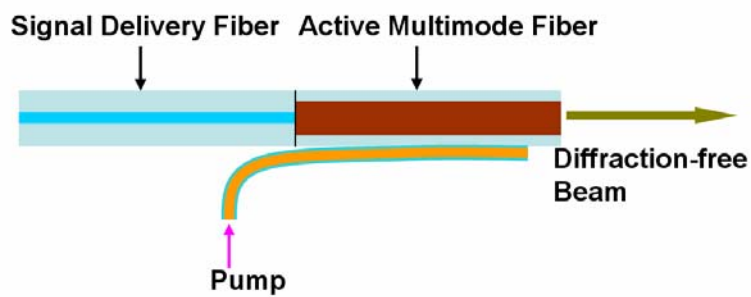


Fig. 4.31. A proposed active fiber device generating high power diffraction-free beams (MM fiber provides the gain).

4.4 Discussion and Conclusion

Because the exclusively excited $LP_{0,n}$ modes are apertured Bessel fields with different transverse wave vectors, the beam coming from an MMI fiber device possesses the property of nondiffracting propagation like a Bessel beam. As a consequence of multiple interference between the excited $LP_{0,n}$ modes, a variety of optical arrays are produced. And the construction of the optical array can be easily and flexibly manipulated through the parameters of the MMI fiber device, such as the core diameters of the SM fiber and the MM fiber and the length of the MM fiber segment. Most importantly, the behavior of the nondiffracting beam can easily controlled through changing the signal wavelength even after the fiber device has been fabricated.

Furthermore, the concept of generating nondiffracting beam from MMI fiber devices can be combined with other fiber technologies, such as high power fiber lasers and amplifiers, fiber sensors, fiber optical communications. And a lot of novel applications using the nondiffracting beams will bloom.

CHAPTER 5

SUMMARY AND PROSPECT

5.1 Summary

The research of this thesis is mainly based on MMI fiber devices that generally consist of a multimode (MM) fiber and one or two single-mode (SM) fibers. The physics of the MMI fiber devices has been studied thoroughly and their properties have been investigated in detail. Achievement of single-transverse-mode emission while utilizing rare-earth doped MM fibers and generation of nondiffracting beams using large-core MM fibers have been accomplished with MMI fiber devices

Theoretically, self-imaging, i.e., exact reproduction of the input field, can occur periodically in the MM waveguide as a consequence of in-phase MMI. However, it is impossible to realize perfect reproduction of the input field within a practically long MM fiber when many modes are excited because the propagation constants of the excited modes in the MM fibers do not have multiple relationships between each other like the case of planar waveguides. Nevertheless, close resemblance of the input field with a large self-imaging quality can be obtained periodically along the MM fiber when the phase differences between the strongly excited modes are very small. Utilizing the self-imaging

effect, an MMI fiber laser has been demonstrated as a route to obtain true SM emission with a beam quality equal to that of a strict SM fiber. Moreover, due to the spectral filtering effect, the spectrum of the MMI fiber laser is much narrower than that of the corresponding MM fiber laser and can be tailored through control of the MM fiber length. The spectral filtering effect was also used to achieve linearly polarized SM output from an MMI fiber laser using a polarization-maintaining fiber Bragg grating.

Although the first MMI fiber had an efficiency very close to that of the MM fiber laser counterpart, the slope efficiency was smaller than 10% due to the large background loss of the phosphate fiber. The 25 μm fiber core would also be a potential limit of the power scaling of an MMI fiber laser or amplifier. Therefore, large-core silica fibers should be candidates for future high power MMI fiber lasers or amplifiers. Calculations predicted that high-efficiency high power MMI fiber lasers using rare-earth doped silica fibers could be realized when the self-imaging quality is improved and the random mode conversion is suppressed by use of an SM fiber with a large mode-field diameter.

Due to mode orthogonality and on-axis excitation, only $\text{LP}_{0,n}$ modes are excited in the MM fiber segment. Because $\text{LP}_{0,n}$ modes are actually described by apertured Bessel functions, the beam coming from the MM fiber segment exhibit resistance to diffraction spreading like a Bessel beam. It is found that the larger ratio of the core size between the SM fiber and the MM fiber, the longer the nondiffracting propagation distance. As a

result of MMI, a variety of optical traps are formed at different positions in the propagation direction. Most importantly, the propagation behavior of the nondiffracting beam is wavelength dependent. Therefore, the beam coming from an MMI fiber device can be flexibly controlled by changing the signal wavelength. The propagation properties of the nondiffracting beams have been investigated experimentally and theoretically in this thesis. Considering high power MMI fiber lasers and amplifiers, simple MMI fiber devices to generate high power nondiffracting beams are proposed.

5.2 Prospect

Because macro-bending will enhance the mode conversion effect and increase the fiber cavity loss rapidly, the MMI fiber lasers and amplifiers must be kept straight. The loss of random mode conversion also restricts the length of a MMI fiber laser or amplifier to tens of centimeters. Both geometrical aspects make an MMI fiber laser or amplifier like a rod-type fiber laser or amplifier [10, 38, 74] from which hundreds of watts output has been achieved. Therefore, hundreds of watts MMI fiber lasers and amplifiers are feasible by use of recent or next generation technologies.

With recent doping level in silica optical fibers, core absorption of 1000 dB/m can be achieved and a slope efficiency of 41% has been demonstrated. Based on my calculations in Chapter 3, it is very possible to build a single-longitudinal-mode fiber oscillator with output power beyond ten watts or more by use of the MMI fiber laser scheme. In order to check the feasibility of the single-longitudinal-mode oscillator based on MMI fiber structure, an experiment using a 3 cm long 25 μm Er/Yb codoped phosphate fiber and a narrow-band silica FBG was carried out. The experimental setup is shown in Fig. 5.1. The output fiber is a SM fiber inscribed with a FBG with a bandwidth of 0.05 nm. The other devices are the same as the first MMI fiber laser shown in Chapter 3. The optical spectrum and the radio frequency spectrum obtained by a heterodyne measurement are

shown in Fig. 5.2 and 5.3, respectively. Clearly, single-longitudinal-mode operation can be achieved in this short-length MMI fiber laser. However, the slope efficiency of this MMI fiber laser was only 5% because the MM fiber length was not controlled to enable high-quality self-imaging. Nevertheless, this experiment indicates that ten-watt level single-longitudinal-mode fiber oscillators can be realized via the MMI fiber scheme.

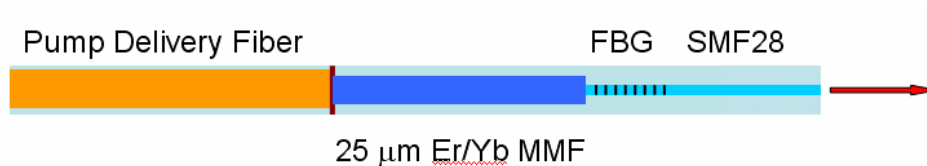


Fig. 5.1. Design of a single-frequency MMI fiber laser.

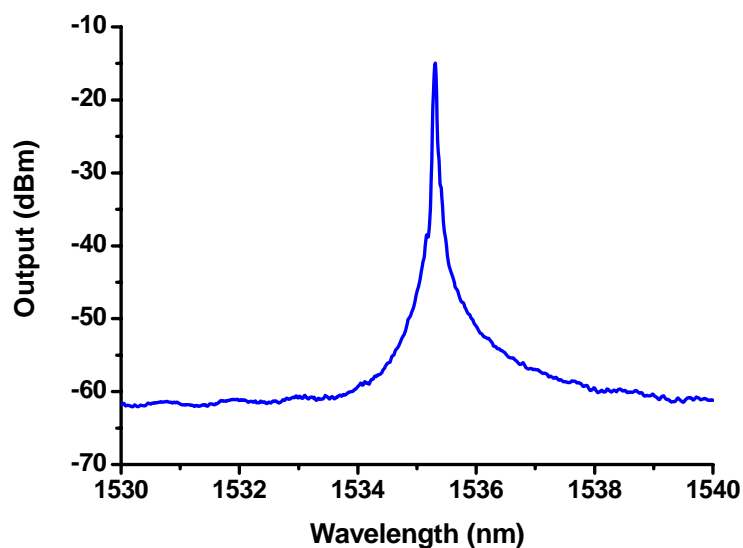


Fig. 5.2. Optical spectrum of the single-frequency MMI fiber laser.

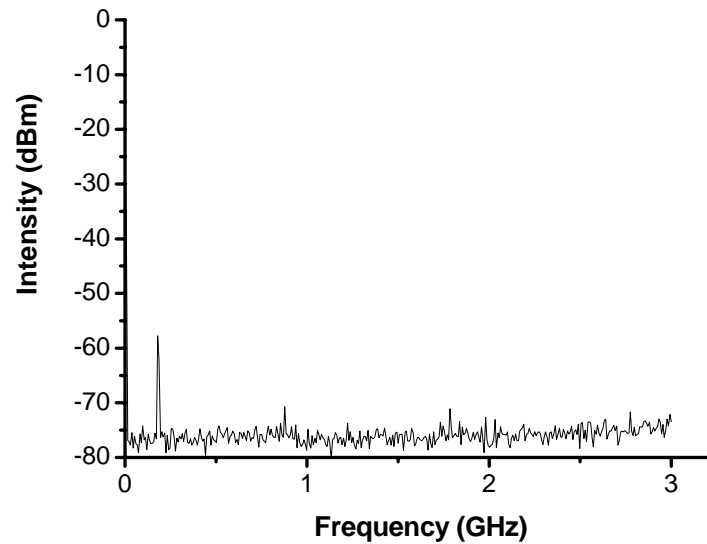


Fig. 5.3. RF beat signal between the emission of the single-frequency MMI fiber laser and a narrow linewidth single-frequency diode laser measured by an electrical spectrum analyzer.

As the nonlinear phenomena of SBS and SRS become the main hindrance of the power scaling of fiber lasers and amplifiers, short-length fiber cavity is a well-known solution to these problems. Therefore, MMI fiber amplifiers are well-suitable for Q-switched and narrow-linewidth signal amplification. Calculation results in Figs. 5.4 and 5.5 show the significant improvement of the thresholds for SBS and SRS when a

large-core MM fiber is used. Note that, 3 mJ and 100 W Q-switched signal has been achieved from a 30 μm rod-type fiber amplifier [74]. It can be predicted that MMI fiber amplifiers can not only provide high-beam-quality SM emission but also boost the energy and the power of Q-switch signal to an unbeatable level due to their ultra large core comparing to large-mode-area core of an SM fiber.

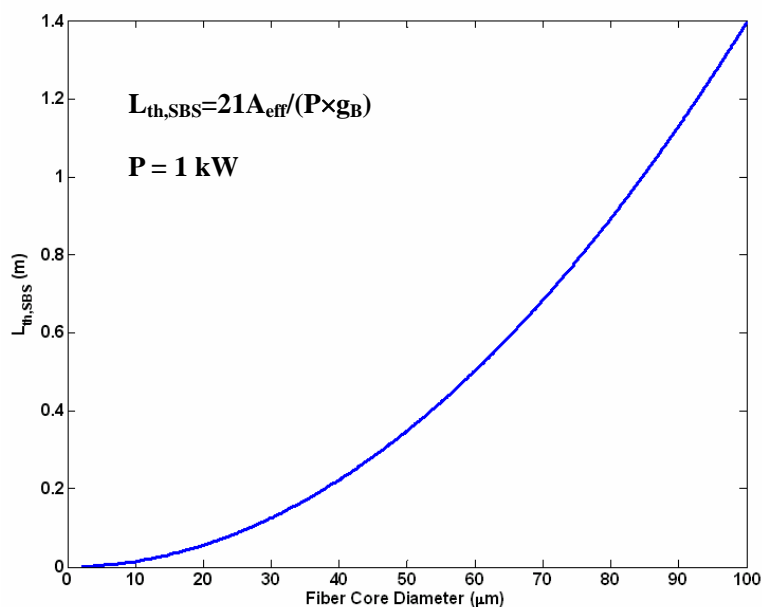


Fig. 5.4. The fiber length associated with the SBS threshold as a function of the fiber core diameter when the power is 1 kW.

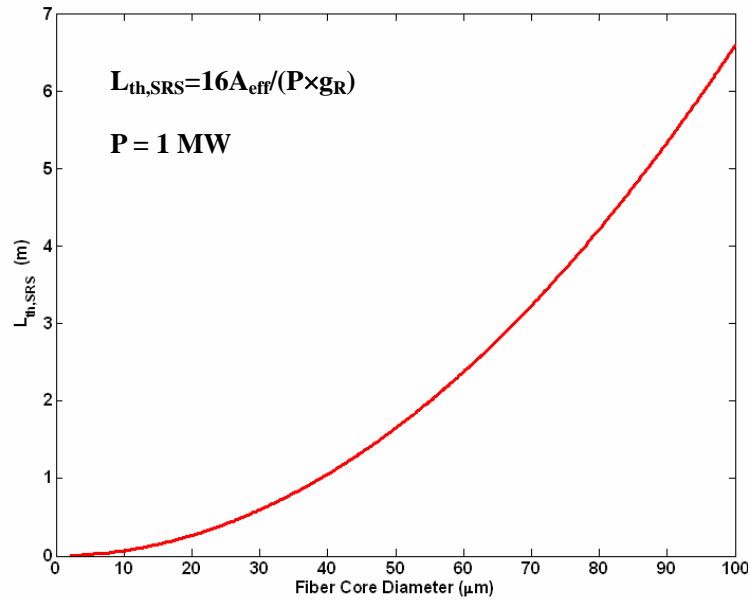


Fig. 5.5. The fiber length associated with the SRS threshold as a function of the fiber core diameter when the power is 1 MW.

Although only the method of generating nondiffraction beams from MMI passive fiber devices has been demonstrated in this thesis, proposed MMI active fiber devices to generate high power nondiffracting beams are very feasible. Besides simplicity, compactness, and flexibility of the fiber devices, high power output and scalability will make proposed MMI active fiber devices much promising for generating high power nondiffracting beams that can be extensively used for particle micro-manipulation, nonlinear optics, atom optics, and micro-fabrication.

REFERENCE

1. T. H. Mainman, "Stimulated optical radiation in ruby," *Nature* **187**, 493-494 (1960).
2. E. Snitzer, "Proposed fiber cavities for optical masers," *J. Appl. Phys.* **32**, 36 (1961).
3. E. Snitzer, "Optical maser action in Nd³⁺ in a Barium crown glass," *Phys. Rev. Lett.* **7**, 444-446 (1961).
4. R. J. Mears, L. Reekie, I. M. Juancey, and D. N. Payne, "Low-noise Erbium-doped fiber amplifier operating at 1.54 μm ," *Electron. Lett.* **23**, 1026-1028 (1987).
5. E. Snitzer, H. Po, F. Hakimi, R. Tumminelli, L. Zenteno, and B. C. McCollum, "Double-clad, offset core Nd fiber laser," in *Proceeding of Conference on Optical Fiber Sensors*, New Orleans, 1988, post-deadline paper **PD5**.
6. V. P. Gapontsev, "High Power Fiber Laser and It's Application", presented at *Laser Optics 2008, 4th International Symposium on High-Power Fiber Lasers and Their Applications*, St. Petersburg, Russia, June 2008.
7. X. Zhu and R. Jain, "10-W-level diode-pumped compact 2.78 μm ZBLAN fiber laser," *Opt. Lett.* **32**, 26-28 (2007).
8. A. Schülzgen, L. Li, V. L. Temyanko, S. Suzuki, J. V. Moloney, and N. Peyhambarian, "Single-frequency fiber oscillator with watt-level output power using photonic crystal phosphate glass fiber," *Opt. Express* **14**, 7087-7092 (2006).
9. J. Wu, Z. Yao, J. Zong, and S. Jiang, "Highly efficient high-power thulium-doped germinate glass fiber laser," *Opt. Lett.* **32**, 638-640 (2007).
10. J. Limpert, O. Schmidt, J. Rothhardt, F. Roser, T. Schreiber, and A. Tunnermann, "Extended single-mode photonic crystal fiber lasers," *Opt. Express* **14**, 2715-2720 (2006).
11. H. L. Offerhaus, N. G. Broderick, D. J. Richardson, R. Sammut, J. Caplen, and L. Dong, "High-energy single-transverse-mode Q-switched fiber laser based on a multimode large-mode-area erbium-doped fiber," *Opt. Lett.* **23**, 1683-1685, (1998).

12. J. M. Sousa and O. G. Okhotnikov, "Multimode Er-doped fiber for single-transverse-mode amplification," *Appl. Phys. Lett.* **74**, 1528-1530, (1999).
13. U. Griebner, R. Koch, H. Schonagel, and R. Grunwald, "Efficient laser operation with nearly diffraction-limited output from a diode-pumped heavily Nd-doped multimode fiber," *Opt. Lett.* **21**, 266-268, (1996).
14. A. Polynkin, P. Polynkin, A. Schülzgen, M. Mansuripur, and N. Peyghambarian, "Watts-level, short all fiber laser at 1.5 μm with a large core and diffraction-limited output via intracavity spatial-mode filtering," *Opt. Lett.* **30**, 403-405, (2005).
15. J. P. Koplow, D. A. V. Kliner, and L. Goldberg, "Single-mode operation of a coiled multimode fiber amplifier," *Opt. Lett.* **25**, 442-444, (2000).
16. P. Wang, L. J. Cooper, J. K. Sahu, and W. A. Clarkson, "Efficient single-mode operation of a cladding-pumped ytterbium-doped helical-core fiber laser," *Opt. Lett.* **31**, 226-228, (2006).
17. L. Dong, J. Li, and X. Peng, "Bend-resistant fundamental mode operation in ytterbium-doped leakage channel fibers with effective areas up to 3160 μm^2 ," *Opt. Express* **14**, 11512-11519, (2006).
18. L. Dong, J. Li, H. McKay, A. Marcinkevicius, B. Thomas, M. Moore, L. Fu, and M. E. Fermann, "Robust and practical optical fibers for single mode operation with core diameters up to 170 μm ," in *Conference on Lasers and Electro-Optics*, (Optical Society of America, San Jose, 2008), Postdeadline Papers **CPDB6**.
19. S. H. Baek and W. B. Roh, "Single-mode Raman fiber laser based on a multimode fiber," *Opt. Lett.* **29**, 153-155, (2004).
20. A. Mocofanescu, X. Zhu, L. Wang, and R. Jain, "Recent studies of CW stimulated Brillouin scattering in single-mode and multimode optical fibers", in *conference on Lasers and Electro-Optics* (Optical Society of America, 2005), paper **CMCC6**.
21. R. Ulrich and G. Ankele, "Self-imaging in homogeneous planar optical waveguides," *Appl. Phys. Lett.* **27**, 337-339 (1975).
22. L. B. Soldano and E. C. M. Penning, "Optical multi-mode interference devices based on self-imaging: principles and applications," *J. Lightwave Technol.* **13**, 615-627,

- (1995).
23. S. W. Allison and G. T. Gillies, "Observations of and applications for self-imaging in optical fibers," *Appl. Opt.* **33**, 1802-1805 (1994).
 24. R. Selvas, I. Torres-Gomez, A. Martinez-Rios, J. A. Alvarez-Chavez, D. A. May-Arrijoja, P. Likamwa, A. Mehta, and E. G. Johnson, "Wavelength tuning of fiber lasers using multimode interference effects," *Opt. Express* **13**, 9439-9445 (2005).
 25. W. S. Mohammed, P. W. E. Smith, and X. Gu, "All-fiber multimode interference bandpass filter," *Opt. Lett.* **31**, 2547-2549 (2006).
 26. W. S. Mohammed, A. Mehta, and E. G. Johnson, "Wavelength tunable fiber lens based on multimode interference," *J. Lightwave Technol.* **22**, 469-477 (2004).
 27. A. Mehta, W. S. Mohammed, and E. G. Johnson, "Multimode interference-based fiber-optic displacement sensor," *IEEE Photon. Technol. Lett.* **15**, 1129-1131 (2003).
 28. H. Li, M. Brio, L. Li, A. Schülzgen, N. Peyghambarian, and J. V. Moloney, "Multimode interference in circular step-index fibers studies with the mode expansion approach," *J. Opt. Soc. Am. B* **24**, 2707-2720 (2007).
 29. K. Hamamoto, E. Gini, C. Holtmann, and H. Melchior, "Single-transverse-mode active multi-mode-interferometer 1.45 μm high power laser diode," *Appl. Phys. B* **73**, 571-574 (2001).
 30. H. J. Baker, J. R. Lee, and D. R. Hall, "Self-imaging and high-beam-quality operation in multi-mode planar waveguide optical amplifiers," *Opt. Express* **10**, 297-302 (2002).
 31. W. S. Pelouch, D. D. Smith, J. E. Koroshetz, I. T. Mckinnie, J. R. Unternahrer, S. W. Henderson, W. R. Scharpf, "Self-imaging in waveguide lasers and amplifiers", in *OSA Topical Meeting on Advanced Solid State Lasers*, Optical Society of America, Washington, D. C., 2002, pp. 6-9.
 32. I. T. Mckinnie, J. E. Koroshetz, W. S. Pelouch, D. D. Smith, J. R. Unternahrer, S. W. Henderson, M. Wright, "Self-imaging waveguide Nd:YAG laser with 58% slope efficiency," in *OSA Topical Meeting on Advanced Solid State Lasers*, Optical Society of America, Washington, D. C., 2002, pp. 262-263.

33. I. T. Mckinnie, B. E. Callicoatt, C. Wood, J. E. Koroshetz, J. R. Unternahrer, M. L. Tartaglia, S. E. Christensen, O. J. Koski, M. Hinckley, M. J. Bellanca, E. Schneider, and D. D. Smith, "Self-imaging waveguide lasers," in *Conference on Lasers and Electro-optics*, CMS1, 2005, pp. 319-321.
34. V. Raghunathan, H. Renner, R. R. Rice, and B. Jalali, "Self-imaging silicon Raman amplifier," *Opt. Express* **15**, 3396-3408 (2007).
35. A. J. Poustie, N. Finlayson, and P. Harper, "Multiwavelength fiber laser using a spatial mode beating filter," *Opt. Lett.* **19**, 716-718 (1994).
36. X. Zhu and R. Jain, "Numerical analysis and experimental result of high-power Er/Pr:ZBLAN 2.7 μm fiber lasers with different pumping designs," *Appl. Opt.* **45**, 7118-7125 (2006).
37. D. Y. Shen, J. K. Sahu, and W. A. Clarkson, "Highly efficient Er, Yb-doped fiber laser with 188 W free-running and > 100 W tunable output power," *Opt. Express* **13**, 4916-4921 (2005).
38. J. Limpert, N. D. Robin, I. M. Honninger, F. Salin, F. Roser, A. Liem, T. Schreiber, S. Nolte, H. Zellmer, A. Tunnermann, J. Broeng, A. Petersson, C. Jakobsen, "High-power rod-type photonic crystal fiber laser," *Opt. Express* **13**, 1055-1058 (2005).
39. J. Durnin, "Exactly solutions for nondiffracting beams, I. The scalar theory," *J. Opt. Am. A* **4**, 651-654 (1987).
40. J. Durnin, J. J. Miceli, and J. H. Eberly, "Diffraction-free beams," *Phys. Rev. Lett.* **58**, 1499-1501 (1987).
41. S. Ruschin and A. Leizer, "Evanescent Bessel beams," *J. Opt. Soc. Am. A* **15**, 1139-1143 (1998).
42. B. Hafizi, E. Esarey, and P. Sprangle, "Laser-driven acceleration with Bessel beams," *Phys. Rev. E* **55**, 3539-3545 (1997)

43. V. Garce-Chavez, K. Volke-Sepulveda, S. Chavez-Cerda, W. Sibbett, and K. Dholakia, "Transfer of orbital angular momentum to an optically trapped low-index particle," *Phys. Rev. A* **66**, 063402 (2002)
44. V. Garce-Chavez, D. McGloin, M. J. Padgett, W. Dultz, H. Schmitzer, and K. Dholakia, "Observation of the transfer of the local angular momentum density of a multiringed light beam to an optically trapped particle," *Phys. Rev. Lett.* **91**, 093602 (2003).
45. V. Garce-Chavez, D. McGloin, H. Melville, W. Sibbett, and K. Dholakia, "Simultaneous micromanipulation in multiple planes using a self-reconstructing light beam," *Nature* **419**, 145-147 (2002).
46. J. Arlt, K. Dholakia, J. Soneson, and E. M. Wright, "Optical dipole traps and atomic waveguides based on Bessel light beams," *Phys. Rev. A* **63**, 063602 (2001).
47. T. Cizmar, M. Siler, and P. Zemanek, "An optical nanotrap array movable over a millimeter range," *Appl. Phys. B* **84**, 197-203 (2006).
48. T. Wulle and S. Herminghaus, "Nonlinear optics of Bessel beams," *Phys. Rev. Lett.* **70**, 1401-1404 (1993).
49. V. E. Peet and R. V. Tsubin, "Third-harmonic generation and multiphoton ionization in Bessel beams," *Phys. Rev. A* **56**, 1613-1620 (1997).
50. H. Sheng, K. Y. Kim, V. Kumarappan, B. D. Layer, and H. M. Milchberg, "Plasma waveguides efficiently generated by Bessel beams in elongated cluster gas jets," *Phys. Rev. E* **72**, 036411 (2005).
51. C. Yu, M. R. Wang, A. J. Varela, and B. Chen, "High-density non-diffracting beam array for optical interconnection," *Opt. Commun.* **177**, 369-376 (2000).
52. M. Fortin, M. Piche, and E. F. Borra, "Optical tests with Bessel beam interferometry," *Opt. Express* **12**, 5887-5895 (2004).
53. Y. Matsuoka, Y. Kizuka, and T. Inoue, "The characteristics of laser micro drilling using a Bessel beam," *Appl. Phys. A* **84**, 423-430 (2006).

54. M. Erdelyi, Z. L. Horvath, G. Szabo, Zs. Bor, F. K. Tittel, J. R. Cavallaro, and M. C. Smauling, "Generation of diffraction-free beams for application in optical microlithography," *J. Vac. Sci. Technol. B* **15**, 287-292 (1997).
55. G. Indebetouw, "Nondiffracting optical fields: some remarks on their analysis and synthesis," *J. Opt. Soc. Am. A* **6**, 150-152 (1989).
56. J. A. Davis, E. Carcole, and D. M. Cottrell, "Nondiffracting interference patterns generated with programmable spatial light modulators," *Appl. Opt.* **35**, 599-602 (1996).
57. N. Chattrapiban, E. A. Rogers, D. Cofield, W. T. Hill, and R. Roy, "Generation of nondiffracting Bessel beams by use of a spatial light modulator," *Opt. Lett.* **28**, 2183-2185 (2003).
58. A. Vasara, J. Turunen, and A. Friberg, "Realization of general nondiffracting beams with computer-generated holograms," *J. Opt. Soc. Am. A* **6**, 1748-1754 (1989).
59. W. B. Williams, and J. B. Pendry, "Generating Bessel beams by use of localized modes," *J. Opt. Soc. Am. A* **22**, 992-997 (2005).
60. S. Saltiel, W. Krolikowski, D. Neshev, and Y. S. Kivshar, "Generation of Bessel beams by parametric frequency doubling in annular nonlinear periodic structures," *Opt. Express* **15**, 4132-4138 (2007).
61. M. Brunel and S. Coetmellec, "Generation of nondiffracting beams through an opaque disk," *J. Opt. Soc. Am. A* **24**, 3753-3764 (2007).
62. E. Mcleod, A. B. Hopkins, and C. B. Arnold, "Multiscale Bessel beams generated by a tunable acoustic gradient index of refraction lens," *Opt. Lett.* **31**, 3155-3157 (2006).
63. S. K. Eah and W. Jhe, "Nearly diffraction-limited focusing of a fiber axicon microlens," *Rev. Sci. Instrum.* **74**, 4969-4971 (2003).
64. S. Cabrini, C. Liberale, D. Cojoc, A. Carpentiero, M. Prasciolou, S. Mora, V. Degiorgio, F. De Angelis, and E. Di Fabrizio, "Axicon lens on optical fiber forming optical tweezers, made by focused ion beam milling," *Microelectron. Eng.* **83**, 804-807 (2006).

65. T. Grosjean, S. S. Saleh, M. A. Suarez, I. A. Ibrahim, V. Piquerey, D. Charraut., and P. Sandoz, "Fiber microaxicons fabricated by a polishing technique for the generation of Bessel-like beams," *Appl. Opt.* **46**, 8061-8067 (2007).
66. V. S. Ilchenko, M. Mohageg, A. A. Savchenkov, A. B. Matsko, and L. Maleki, "Efficient generation of truncated Bessel beams using cylindrical waveguides," *Opt. Express* **15**, 5866-5871 (2007).
67. S. Ramachandran and S. Ghalmi, "Diffraction-free, self-healing Bessel beams from fibers," in *Conference on Lasers and Electro-Optics/Quantum Electronics and Laser Science conference*, San Jose, 2008, **CPDB5**.
68. D. McGloin and K. Dholakia, "Bessel beams: diffraction in a new light," *Contemp. Phys.* **46**. 15-28 (2005).
69. Z. Jaroszewicz, A. Kolodziejczyk, A. Kujawski, and C. Gomez-Reino, "Diffractive patterns of small cores generated by interference of Bessel beams," *Opt. Lett.* **21**, 839-841 (1996).
70. S. Chavez-Cerda, E. Tepichin, M. A. Meneses-Nava, G. Ramirez, and J. M. Hickmann, "Experimental observation of interfering Bessel beams," *Opt. Express* **3**, 524-529 (1998).
71. S. Chavez-Cerda, M. A. Meneses-Nava, and J. M. Hichmann, "Interference of traveling nondiffracting beams," *Opt. Lett.* **23**, 1871-1873 (1998).
72. D. McGloin, G. C. Spalding, H. Melville, W. Sibbet, and K. Dholakia, "Three-dimensional arrays of optical bottle beams," *Opt. Commun.* **225**, 215-222 (2003).
73. M. Zamboni-Rached, "Stationary optical wave fields with arbitrary longitudinal shape by superposition equal frequency Bessel beams: Frozen waves," *Opt. Express* **12**, 4001-4006 (2004).
74. J. Limpert, S. Hofer, A. Liem, H. Zellmer, A. Tunnermann, S. Knoke, and H. Voelckel, "100-W average-power, high-energy nanosecond fiber amplifier," *Appl. Phys. B* **75**, 477-479 (2002).